Vacuum and Optical Designs for an Open-access Trapped Ion Quantum Processor

by

Noah Greenberg

A thesis
presented to the University of Waterloo
in fulfillment of the
thesis requirement for the degree of
Master of Science
in
Physics (Quantum Information)

Waterloo, Ontario, Canada, 2020

Author's Declaration

I hereby declare that I am the sole author of this thesis. This is a true copy of the thesis, including any required final revisions, as accepted by my examiners.

I understand that my thesis may be made electronically available to the public.

Abstract

This thesis focuses on the design of a vacuum system for a trapped ion quantum computer that will house an advanced ion chip trap from Sandia National Laboratories [51], capable of performing high fidelity operations on up to tens of qubits [55]. The thesis will outline the different design considerations, criteria, and serve to document the final design choices, in addition to optical design work that will be used to drive resonant atomic transitions in the qubit of choice, $^{133}Ba^{+}$, as well as the qudit, $^{137}Ba^{+}$.

Acknowledgements

First off, I would like to thank my advisor, Prof. Crystal Senko, for initially giving me the opportunity to work in her lab.

I would also like to thank Prof. David Corey and Transformative Quantum Technologies (TQT) for providing the space and funds for this project, as this type of open-access experiment would certainly not have been possible otherwise. In particular, I would like to thank Sara Clark from TQT for her help with this project in these early stages.

The designs presented here would also not have been possible without the many conversations I have had with our vendors. I feel as if I have learned quite a bit about the practical challenges and implications of different vacuum and optical designs through these conversations. That being said, I would like to thank Ishwar Niraula and the group at SAES Getters for their expertise and recommendations regarding non-evaporable getters (NEG). I would also like to thank Dario Nicolosi from the SAES Getters group in Italy for our conversations related to NEG thin films and helping to evaluate their viability in ion trapping experiments. I would like to thank Hamid Saidi from Vacuum Products Canada for our meetings at IQC to discuss vacuum diagnostics and I would like to thank Todd TeVogt from Edwards Vacuum as well as Joey Keller from Kurt J. Lesker for meetings related to our titanium sublimation and ion pump solutions.

Besides these people that helped me to navigate different possible pumping schemes, there are a few individuals from industry, that through discussion, helped shaped the design of the vacuum chamber. Most relevantly, I would like to thank Takeshi Osako and the team at Vista Corp. for manufacturing the main portion of the vacuum chamber. I would also like to thank Jimmy Stewart at Atlas Technologies and Scott O'Connell from Anderson-Dahlen Inc. for discussing other viable ultra-high vacuum chambers and working with me to better understand their capabilities. I would also like to thank Kimball physics for their well designed off-the-shelf solutions and transparency in their manufacturing process.

The other manufacturers that also made the vacuum design presented in this thesis possible are MPF Inc., MDC Vacuum Products, and Tactic Electronics Inc. I would like to thank these suppliers for their unique, custom solutions that helped us to optimize our system.

Finally, I would also like to thank all the members from both Prof. Crystal Senko's ion trapping group as well as Prof. Rajibul Islam's group at IQC for the countless discussions these past two years.

Dedication

To all the ion trappers out there, happy trapping.

Table of Contents

List of Tables

List of Figures

Chapter 1

QuantumIon Project Overview

The birth of quantum information in the 1980's [2] and the advent of powerful theories like quantum error correction and fault-tolerant quantum computing [105] proving the viability of quantum computing sparked serious experimental investment in the 1990s that has now grown to unfathomable proportions. Of course this investment is only realized because of the promises that come with building machines capable of quantum information processing. The two most famous algorithms that can be run on quantum computers that provide a significant benefit over classical computers are Shor's factoring algorithm and Grover's search algorithm [57]. These provide exponential and quadratic speed ups, respectively. Besides these impressive algorithms, quantum computers can also be used to more efficiently send information with techniques like superdense coding [57]. These examples are end-all goals associated with experimental quantum information processing and would require a fault-tolerant quantum computer. Before this can be achieved reliable quantum error correction must be established, which necessitates gate and measurement fidelities to be above a certain fidelity threshold. Experimental quantum information processing is near the point where fidelities are high enough for near-term applications of quantum computers like quantum simulation or error correction with a single logical qubit could potentially be viable and act as a stepping stone towards more complicated machines [47][48].

The overarching purpose of the QuantumIon project is to provide an open-access trapped ion processor to the research community, meant for many different quantum information researchers. This will hopefully foster collaboration and allow ideas to be tested without building entirely new experiments. The truly sizable machines capable of quantum error correction on >10 logical qubits are likely decades away, but there is precedence for near term projects focused on enabling different quantum information researchers before larger-scale machines can be built or further conceived [58]. These near term projects are

aimed at giving researchers more control over underlying hardware to prove out concepts relating to general purpose quantum computing. For these Noisy Intermediate-Scale Quantum (NISQ) platforms, trapped ions are an ideal candidate because of their unmatched single and two qubit gates fidelities [56], state-preparation [59], and coherence times [54]. The QuantumIon project will implement trapped ions as both processing and memory qubits.

The majority of the work in this thesis is focused on designing and simulating the vacuum chamber and continuous wave (CW) optics that will drive resonant or near-resonant transitions in the trapped barium ions. The other prominent portions of the project not covered in this thesis is the individual addressing scheme, which will be used to drive single qubit rotations and entangling operations between ions as well as the control system, which will be used to calibrate the machine, shape pulses, and provide precision timing during an experiment.

The thesis starts first with more information regarding the major "pillars" of the project before switching focus to the CW optical designs. The CW optical designs are accompanied by basic information related to cooling and preparing ions. The optical sections also include optomechanical designs that will allow the machine to operate remotely and without the need of a person in-lab. After this, there is a discussion about the relationship between trapped ion chains used in quantum information processing and the vacuum system. Basic material related to designing and calculating base pressures for vacuum systems is presented followed by a survey of current vacuum technologies. The design and simulated pressures of the vacuum chamber are discussed, before ending with a proposed baking procedure.

1.1 Facility and Vacuum System

With a project that demands high performance and repeatability, the design of the room and operating environment is a crucial component, which must be addressed during the initial construction of the first major experiment. This could ultimately dictate the capabilities of the machine and it is important that needs of the first experiment as well as the needs of future experiments are considered. In general, temperature stability, humidity control, and vibration isolation at a fundamental level need to be addressed. As this experiment is meant to act as a resource for the research community, it is paramount that the machine is consistent, so there is an even greater need to isolate the experiment from the environment. These fluctuations are reflected in the experiment by deviations in laser frequency, power, phase, beam pointing, the trap potential, and the magnetic field at the ion, eventually accumulating in the failure of individual experiments or destruction of

experimental hardware. Figure 1.1 is a layout of a room that is meant to act as a guideline for the design for the QuantumIon experiment.

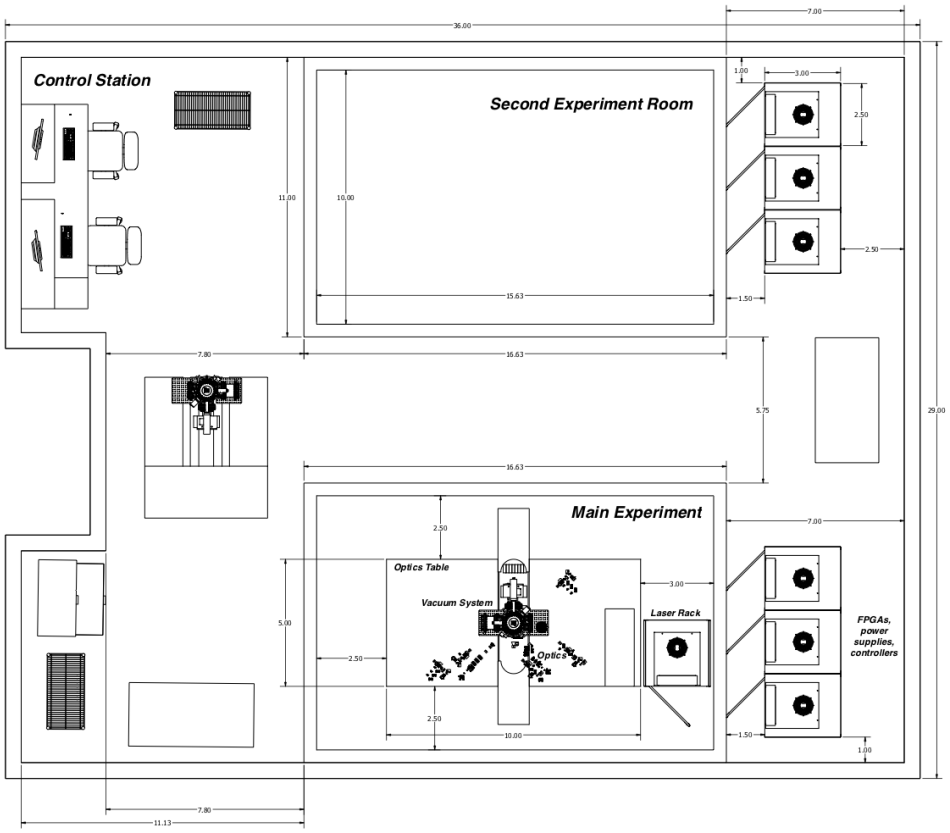

Figure 1.1: Facility layout for the QuantumIon experiment, with the units in feet. The vacuum system is centered on a custom optics table.

Besides the room itself, another important mechanical aspect for the experiment is the vacuum apparatus. The main goal of the vacuum apparatus is to provide ultra-high vacuum (UHV) at or below 10^{-11} mbar, enabling traps to capture large chains of ions for extended periods of time [10]. UHV systems are utilized in many areas of physics and have been well studied. UHV systems are studied so much so, that companies offer a wide variety of solutions that will guarantee these target pressure as long as the vacuum chamber is properly cleaned and baked.

Regardless of the readiness of vacuum technology, the integration of the vacuum system with the optical requirements necessary to achieve separate trapping zones and high fidelity

operations on many ions is no easy task. In addition to this complex integration, we can always try to push the base pressure lower with novel implementations of vacuum technologies, which is important for improving the total experimental lifetime of an ion chain.

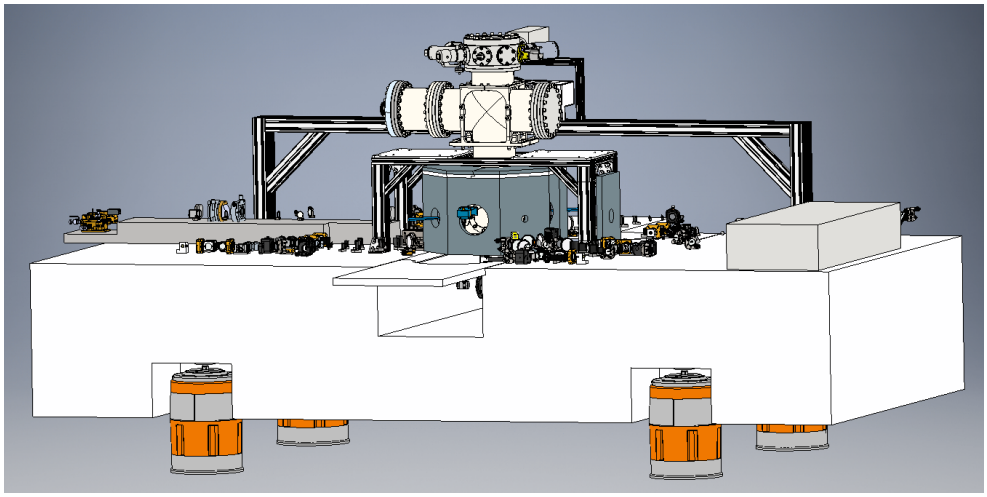

Figure 1.2: Vacuum chamber centered on the optics table, however not all mounting structures or optics are pictured. Cavity below the vacuum chamber to allow for ion imaging optics. Optics table height is 30 inches from the floor.

1.2 Individual Addressing

Few systems have been built in academia or industry that can individually address large chains of ions, a requirement to drive entangling operations between arbitrary pairs of ions in a chain. In fact, the state-of-art trapped ion quantum computer that utilizes individual addressing schemes with light, as of Spring 2020, is 17 fully connected ions [86]. This project plans to maintain > 10 fully connected qubits by using a laser written waveguide to split the light into 17 different channels, 16 of which will be sent to individual ions to drive transitions between hyperfine levels. Planar waveguides have been integrated into ion traps for final focusing of the collimated light at the ions [111], but this laser written waveguide is used as an intermediate step far before focusing at the ions. The designers of the individual addressing optics are Nikolay Videnov, a current Masters student, and Matt Day, a post doctoral research fellow on the QuantumIon project.

1.3 Control System

For a trapped ion experiment to be run successfully, the ion must be prepared in some motional ground and electronic state. While Doppler cooling, resolved sideband cooling, and optical pumping all typically happen on the order of milliseconds and do not require nanosecond timing resolution, other portions of the experiment are limited by this. Specifically, the pulse shape and timing of the Raman transitions are of the upmost importance for high fidelity entangling operations and could benefit from improved timing resolution [49]. The two most common control systems, that are not homebrew, among ion trappers are Ion Control developed at Sandia National Laboratories [50] and Sinara developed by M-Labs [60]. These systems offer timing resolution on the order of tens of nanoseconds or better, while QuantumIon aims to have sub-nanosecond resolution. This is just one example improvement of QuantumIon's control system over existing systems.

Besides the timing of the experimental laser pulses, the QuantumIon control system has domain over the optomechanical devices which will be used for gross power adjustments, polarization control, fiber coupling, phase modulation, and beam positioning at the ion. This aspect of system is important for providing consistent experimental results. As an open resource for the quantum information community it is necessary for the system to be reliable and we aim to achieve this by making these routines and calibrations automated, more precise, and without the need for a physical person in the experiment room. This work is being completed by a Ph.D. student, Richard Rademacher, and more information can be found in the Masters thesis [45].

1.4 $^{133}Ba^{+}$ Qubit and $^{137}Ba^{+}$ Qudit

There is common functionality that all quantum computing experiments must have, explained typically as DiVincenzo's criteria. As the main processing unit in this experiment is a trapped ion, the atomic structure of the ion plays in important role in realizing DiVincenzo's criteria. For example, in Figure 1.3 the $S_{1/2} \rightarrow P_{1/2}$ is used to measure the ions state and it also plays a role in state preparation. The metastable D states are necessary for measuring qudits, but they are also useful in achieving higher state preparation fidelities. $^{133}Ba^{+}$ is an attractive qubit candidate because the nuclear spin of 1/2 gives rise to a simplified hyperfine structure in the $S_{1/2}$ state that reduces leakage to other hyperfine levels during Raman transitions, improving gate fidelities [61]. The hyperfine structure also has a nearly magnetic field insensitive clock transition, which can be used to encode the computational basis states, $|0\rangle$ and $|1\rangle$. For comparison, in the $S_{1/2}$ state of $^{43}Ca^{+}$, which

has a nuclear spin of $I = 7/2$, there are $|F = 3, m_f = 0\rangle$ and $|F = 4, m_f = 0\rangle$ clock states, but they are accompanied by fourteen other hyperfine levels. $^{133}Ba^+$ only has two other hyperfine states in addition to the clock states, the simplest possible hyperfine structure.

$$|I - J| + |I - J + 1| \cdots \leq F \leq I + J \tag{1.1}$$

$$-F \leq m_f \leq F \tag{1.2}$$

Possible quantum F numbers depending on the nuclear spin I, and the total angular momentum J [53].

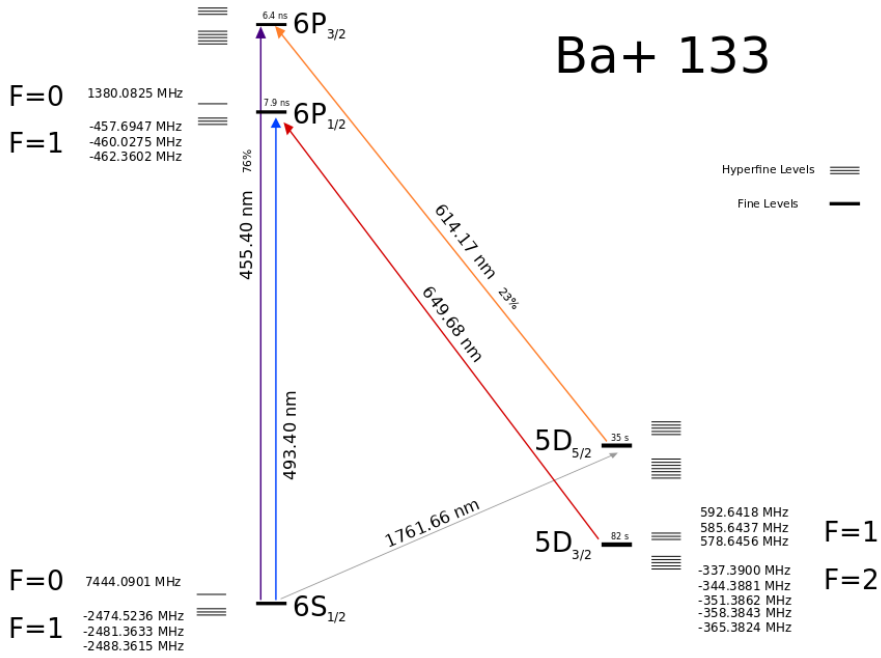

Figure 1.3: $^{133}Ba^+$ atomic structure, with transitions [62], branching ratios [59] and lifetimes [46]. Further calculations of Zeeman split hyperfine levels in Appendix B based on measured splittings [59]. Magnitude of the magnetic field is 5 Gauss.

Besides this tidy hyperfine structure, $^{133}Ba^+$ also has a long-lived $D_{5/2}$ state that can be used for storing states. This is a necessity in order to perform measurements in qudit

systems where entanglement is created between > 2 hyperfine levels [46], but it can also be used to improve the fidelity of certain processes in qubit systems like state preparation [59]. In the latter, state determination is typically done with state-dependant fluorescence, which is when, depending on whether or not fluorescence is collected in a time window, the state can be said to be in $|F = 0, m_f = 0\rangle$ or $|F = 1, m_f = 0\rangle$ with relative confidence. This measurement scheme works due to the selection rules forbidding $F = 0 \leftrightarrow 0$ electric dipole transitions, but due to imperfect state initialization or off resonantly driving the $F = 1 \leftrightarrow 1$ state when the $|1\rangle = |F = 1, m_f = 0\rangle$ is prepared this fidelity can become limited. Shelving the $|F = 1, m_f = 0\rangle$ state in certain measurement schemes can greatly improve this fidelity [59]. The shelving levels, $D_{3/2}$ and $D_{5/2}$, in $^{133}Ba^+$ are long lived in comparison with other trapped ion qubits, with lifetimes of 30 and 80 seconds, respectively.

Another attractive feature of $^{133}Ba^+$ are the wavelengths that can be used to manipulate the ion. Every wavelength, save one, falls in the visible spectrum. This includes wavelengths used for photoionization and Raman transitions, which makes the optical engineering easier (whether it is with bulk optics, planar or laser written waveguides, micro-Fresnel lenses, etc.). For comparison, the transitions in $^{171}Yb^+$ are overwhelmingly ultra-violet or near-infrared. Figure 1.1 presents wavelengths that will be used to manipulate the barium ions:

Term	Resonant Transition	Wavelength
Cooling	$6S_{1/2} \rightarrow 6P_{1/2}$	493 nm (VIS)
Second Cooling	$6S_{1/2} \rightarrow 6P_{3/2}$	455 nm (VIS)
Repumper	$5D_{3/2} \rightarrow 6P_{1/2}$	650 nm (VIS)
Shelving Repumper	$5D_{5/2} \rightarrow 6P_{3/2}$	614 nm (VIS)
Shelving	$6S_{1/2} \rightarrow 5D_{5/2}$	1762 nm (SWIR)
Raman	NA	532 nm (VIS)
First Photoionization	$6S_0 \rightarrow 6P_1$	553 nm (VIS)
Second Photoionization	NA	405 nm (VIS)

Table 1.1: Singly ionized barium wavelengths as well as photoionization wavelengths.

Finally, there is one obvious drawback to using $^{133}Ba^+$ which is that it is radioactive, sporting an exposure rate of $\Gamma = 28.564$ mSv cm^2 mCi^{-1} hr^{-1} [63]. This provides the technical challenge of integrating lead shielding into the experiment, typically about 1 inch thick walls are required to keep exposure low, but this depends on the amount of radioactive material used. As of now the lab works with 1/2 mCi sources. These samples come from Eckert and Ziegler, and can come with or without extra stable barium added to the source. In the interest of documentation it is worth pointing out that other isotopes

can be obtained in high purity like ^{138}Ba with 99.7% purity in salt form through Trace Sciences International Corp., should that so be desired.

As has been shown, there are many advantages to using $^{133}Ba^{+}$ as a qubit and the benefits seem to far our way the drawbacks which is why this has been referred to as the "goldilocks" qubit [64].

Besides using $^{133}Ba^{+}$ as a qubit, this project also plans to implement $^{137}Ba^{+}$ as a qudit. The main difference between these two isotopes is that the latter has $I = 3/2$, which gives rise to more hyperfine levels. These extra hyperfine levels can be used to encode information in more than two hyperfine levels and create entanglement between three and five levels reliably [102]. The Hilbert space in these higher dimensional quantum information bits scale like d^n, where d is the number of basis states ($d = 2$ for qubits), and n is the number of bits. Storing information this way increases the computational power of each ion, but more concretely, algorithms can potentially be sped up with qudits by applying gates in parallel [103].

Chapter 2

Loading and Ion Preparation

This section outlines key details in trapping and cooling ions, which are fundamental steps before ions can be used for processing information. Before any quantum operations can begin, ions need to be loaded into the trap and sufficiently cooled to the motional ground state. Cooling chains of ions is an active area of research and cooling all ions in the chain to the motional ground state is non-trivial [22][107]. This chapter briefly introduces loading ions, cooling ions, and preparing them in a chosen hyperfine state with a specific example. Once a hyperfine state has been prepared, then the ion can be used for quantum information processing.

2.1 Loading

The first step in most trapped ion experiments is to load ions into the trap. There are two main ways that this is done. Either a metallic piece of the element is heated to the point of sublimation, or a laser pulse is focused onto a substrate that contains the element, which also causes sublimation. Laser ablation has many benefits over traditional atomic ovens as it is faster and more efficient.

Traditional atomic ovens can be made up of a stainless steel tube containing the element, with a wire wrapped around the tube so that when a large current (a few amps) is ran through the wire it resistively heats the tube and metal to sublimation. This process takes minutes to reach the sublimation point even in UHV and causes large clouds of atoms to enclose the trapping zone. This exposes the trap to significantly more atomic flux than laser ablation and the process can not immediately be terminated when an ion has been

loaded because of residual heat. The denser clouds created by ovens increases broadening from collisions, which makes isotope selective loading more difficult. While ablation pulses produces clouds that contain ions as well as neutrals, the parameters of ablation can be tuned such that it primarily produces neutral atoms [74]. This is particularly important in sources that contain multiple isotopes, so that a two-step photoionization process can be implemented and isotope selective loading can be accomplished. Producing more neutrals also reduces trap charging.

(a) Oven installed in a vacuum chamber. (b) $BaCl_2$ deposited on aluminum substrate.

Figure 2.1: Two common methods for loading ions are with resistively heated metals and laser ablated salts or metals.

Current ablation loading practice in the lab is to "condition" the target by scanning a large area and ablating in fine steps. This changes the surface of the $BaCl_2$ to make the loading more consistent. As seen in Figure 2.1b, the surface of the salt is rough and the peak to valley difference is substantial. Typical laser ablation pulses contain about 50-170 μJ and the efficiency of loading decreases slowly over time.

This project plans to implement three ablation targets and no ovens. The ovens were not considered for the aforementioned reasons as well as restrictive space constraints. Average oven designs are large, however, there are examples of compact ion traps implementing

ablation and ovens in their designs, but this would take significant engineering [75][76][36]. Two of the planned ablation targets will be orientated in the chamber for isotope selective loading.

2.1.1 Isotope Selective Photoionization

The first step in a trapped ion experiment is to load a specific barium isotope, assuming that an ion reservoir is not being maintained in other parts of the trap. While this cannot be done perfectly, steps can be taken to minimize the amount of accidental loading of an ion of the wrong isotope. Loading a chain of 16 ions of one specific isotope is challenging, but efficient isotope selective loading of this length has been demonstrated with barium [77]. In general, the probably of success depends on the relative neutral isotope shifts relating to the first step in the photionization process, the purity of the target, and the experimental details that cause broadening of the first transition [77].

Using a two-step photoionization process on a neutral atom can be compared to a loading process with a laser ablation pulse of higher power that often strips one of the electrons in the valance shell, regardless of isotope and thus allowing any isotope to be trapped.

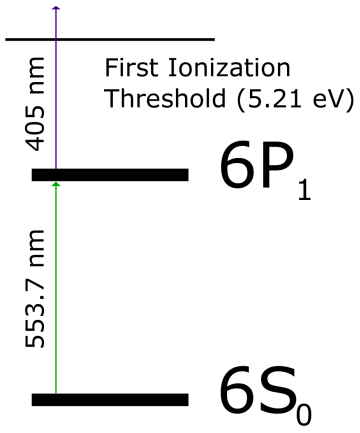

Figure 2.2: Efficient two-step photoionization process for barium, adapted from [77].

There are multiple paths for a two-step photoionization process involving barium, but the most efficient path that has been demonstrated in a lab is by exciting the $6S_0 \rightarrow 6P_1$ with a 553 nm laser and using a 405 nm laser to strip a single electron [77]. This specific ionization path is more efficient because it utilizes a strong electric dipole transition as compared to other schemes using quadrupole transitions [77]. The linewidth of the 553 nm

laser is hundreds of kilohertz while the transitions in different isotopes are spaced two or third orders of magnitude higher, allowing for a high degree of isotope specificity [46]. Depending on the isotope chain that a user wishes to load, the detuning of the frequency from the $6S_0 \rightarrow 6P_1$ transition can be optimized as well as the power for a maximum probability of success [77].

2.2 Doppler Cooling Limit

After ablation, most of the neutral atoms are moving quite quickly, on the order of hundreds of meters per second [74]. These could not possibly be trapped by any trap, let alone a surface trap with a potential < 1 eV. Even low velocities can cause significant broadening of atomic transitions, which can be reduced by orienting the cooling and photoionization beams so that they are perpendicular to the atomic beam. This greatly reduces the impact of Doppler broadening on the transitions and allows efficient cooling to occur. The limit for Doppler cooling is set by how quickly light can scatter on the $6S_{1/2} \rightarrow 6P_{1/2}$ dipole transition [82]. This equilibrium assumption is valid when the secular frequency ω is $\Gamma \gg \omega$, such that the dipole transition is broadened to the point that the motional sidebands cannot be accessed [106]. The secular frequency of the ion refers to the frequency of motion of the ion in the trap, as opposed to the frequency of the trap itself. The secular frequency can be calculated with Equation 2.4.

$$T_{lim} = \frac{\hbar\Gamma}{2k_b} \tag{2.1}$$

The temperature limit is determined by the decay rate Γ, and driving to the $6P_{1/2}$ state allows many cooling cycles to be completed in a short amount of time because the lifetime is 7.9 ns. This can be rewritten as a function of detuning from the atomic transition Δ and saturation $s = (I/I_{sat})/(1 + 4\Delta^2/\Gamma^2) \approx I/I_{sat}$. The saturation is based on the applied intensity I relative to the saturation intensity I_{sat}. The dipole emission pattern ζ is taken to be 2/5 [84].

$$T_{lim} = \frac{\hbar\Gamma}{8k_b}(1+\zeta)\left((1+s)\frac{\Gamma}{2|\Delta|} + \frac{2|\Delta|}{\Gamma}\right) \tag{2.2}$$

This equation is valid for $\Delta < 0$, where the optimal detuning to give the lowest temperature is $\Delta_{lim} = -\Gamma\sqrt{1+s}/2$ [84]. Figure 2.3 provides a useful starting point when cooling

barium. In practice many people just set $\Delta = -\Gamma/2$ as a starting point when Doppler cooling.

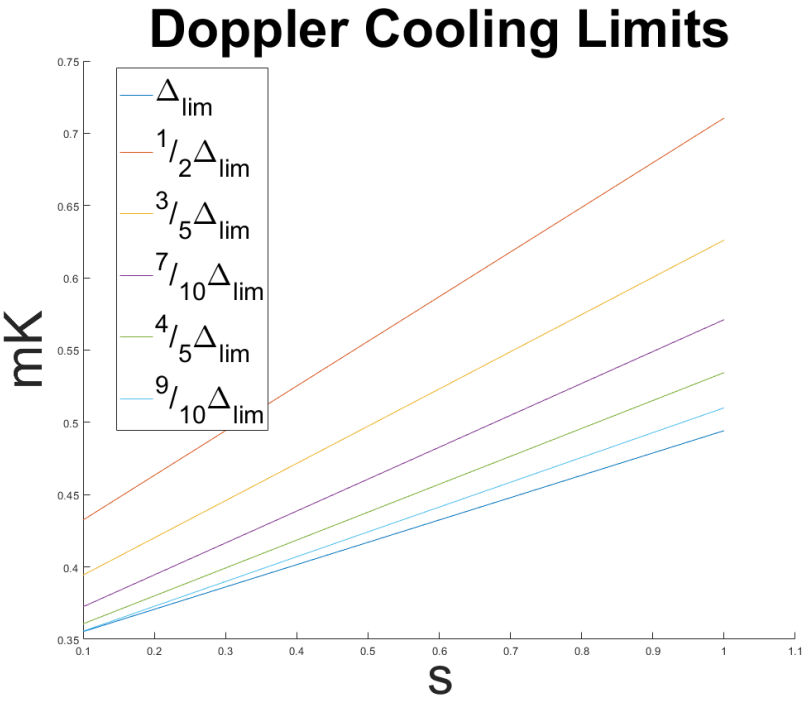

Figure 2.3: Doppler cooling limits for $^{133}Ba^+$ as a function of saturation s with different detunings Δ.

The cooling, measuring, and repumping (CRM) beam will be used to Doppler cool the ions, among other various tasks like state preparation.

2.3 Ion Temperature Measurements

In order to trap long chains of ions, it is necessary to correct the radial micromotion of the ions by making small changes to the DC voltages and thus potential. There are many sources that can cause micromotion like trap contamination from ablation loading. To evaluate these changes, the temperature of the ions can be taken, but different temperature measurement methods are only valid in certain temperature ranges so it is important to make sure that the temperature of both hot and cold trapped ions can be taken.

Before explaining the different ways to measure an ion temperature it is important to understand the regime when ions secular motion is much greater than the linewidth of the transition being driven, $\omega \gg \Gamma$. In this regime, the ions secular frequency is much faster than the lifetime of the state and the classical treatment of radiation pressure is no longer valid. This occurs after the ions have undergone Doppler cooling and when the ions are already in the Lamb-Dicke Regime. The Lamb-Dicke Regime occurs when $\eta\sqrt{2n+1} \ll 1$, where n is a motional quantum number and the Lamb-Dicke parameter is $\eta = k\sqrt{\hbar/2m\nu}$. The Lamb-Dicke parameter depends on the $\vec{k}$ of the incident light projected onto the motional axis of the ion that is oscillating with frequency ν. It depends on the mass m of the ion as well. The ions can be cooled further to a few μK using resolved sideband cooling [11]. This can only be done when $\omega \gg \Gamma$ and can be done in parallel on ions in chains [107]. The process works by detuning the transition such that the red 1^{st} order motional sideband is being driven. The ion will then spontaneously emit a photon that on average has $\hbar\omega$ more energy than the initially absorbed photon [11]. The trap frequency and ion species determine the secular frequency ω, as is shown below. In this project this can be done on the $6S_{1/2} \rightarrow 6P_{1/2}$ transition using the Raman laser or on the $6S_{1/2} \rightarrow 5D_{5/2}$ transition with the 1762 nm laser that has a linewidth stabilized to 1 Hz. Using the quadrupole transition requires coupling to the $P_{3/2}$ state because it is metastable with a lifetime of order seconds. This greatly increases the amount of transitions, and thus cooling, that can be driven in a given time period.

When the ions are near or below the Doppler cooling limit the amplitude of these red and blue 1^{st} and 2^{nd} order motional sidebands can be measured to determine the temperature. At high temperatures the Doppler recooling method can be used to determine the temperature. This works by measuring the fluorescence response of the ion after the ion has had time to heat and comparing this response for different time intervals. Different temperature measurement methods are outlined in Table 2.1.

Probe	Demonstrated Range	Timescale
Resolved Sideband	μK - 2 mK [106]	hundreds of μs
Dark Resonance (co-propagating)	0.7 - 67 mK [83]	hundreds of μs
Spatial	1-2 mK [84]	$>$ milliseconds
Doppler Recooling	1 K-100 K [85]	milliseconds

Table 2.1: Different techniques to measure ion temperature.

The temperature of ions is somewhat ambiguous, meaning that the temperature of an ion is not comparable to the temperature of a collection of many molecules and atoms in the typical sense. Depending on the regime, the temperature and average quantum

number $\bar{n}$ describing the excitation of the motional state is approximated differently. Near the doppler limit $\bar{n}$ can be calculated with Equation 2.3 [108].

$$\bar{n}_{dop} = \frac{\exp \frac{-\hbar\omega}{k_b T}}{1 - \exp \frac{-\hbar\omega}{k_b T}} \tag{2.3}$$

Assuming a radial secular frequency with $V = 200$, $R = 140$ μm, and $\Omega_{RF} = 2\pi \times 44$ MHz, $\bar{n}_{dop} \approx 2$. The RF voltage V is limited < 300 V [51].

$$\omega = \frac{qV}{\sqrt{2}\Omega_{RF} m R^2} = 2\pi \times 3.01 \text{ MHz} \tag{2.4}$$

$\bar{n}_{dop}$ is the limit that can be achieved with Doppler cooling, but with the previously mentioned resolved sideband technique, the cooling limit can be significantly reduced. If Doppler cooling and then resolved sideband cooling is implemented, the temperature can be measured by comparing the strengths of the red and blue sidebands [106].

$$\bar{n}_{sb} = \frac{1}{(r_k)^{1/k} - 1} \tag{2.5}$$

Where k is the sideband order and $r_k = P_b/P_r$ is the ratio of the blue over red sideband power. Assuming $r_k = 3/2$, then $\bar{n}_{sb} = 2$ for the 1^{st} order sideband case. With this method of comparing sidebands, it can be seen that the temperature of the ions can be measured well above the Doppler cooling limit in this trap with the sidebands, meaning that there is no lapse in temperature range that can be probed with this projects specific optical set up.

At temperatures near the doppler cooling limit and even higher, another method for probing the temperature can be implemented based on dark resonances. Dark resonances occur when a coherent superposition is created between two ground states and is characterized by a drop in the fluorescence. In the case of $^{133}Ba^{+}$, examine a three level case when the levels $6S_{1/2}$ and $5D_{3/2}$ are the ground states, being coupled to the $6P_{1/2}$ excited state. When the detuning of the fields coupling each ground state to the excited state are equal then a dark state will occur. In practice, one of the frequencies is swept while the other is kept fixed and based on the degree of the fluorescence loss, the temperature of the ion can be extrapolated, with colder ions having a greater loss. This has been shown to

be able to probe ion temperatures between the Doppler limit and hot ions well above the Doppler limit [83].

For very hot ions Doppler recooling can be used for measuring the temperature [85]. This can be done with the CRM beam, as can the dark resonance temperature measurement. By implementing different temperature measurement techniques, the range of temperatures at which the ion can be measured extends from the ground state all the way up to hot ions of a few kelvin.

2.4 State Preparation and Shelving

The state preparation of most trapped ion qubits starts with optical pumping, a tremendously popular technique developed in the mid 20^{th} century [104]. Optical pumping works by taking advantage of allowed and forbidden transitions and manipulating the polarization of the light such that only specific transitions are being driven. The polarization can be a mixture of linearly or circularly polarized light such that it drives π, σ^+, or σ^- transitions. Typically the fidelity is limited by off-resonant scattering, imperfect polarization, or misalignment of the beam from the quantization axis. In $^{133}Ba^+$, the state that is typically prepared is the $|F = 0, m_f = 0\rangle$ state, corresponding to the computational basis state $|0\rangle$. From here the $|1\rangle$ can be prepared with a microwave pulse. In $^{137}Ba^+$ the state, $|F = 2, m_f = 2\rangle$, can be prepared with σ^+ light.

2.4.1 Optical Pumping

$^{133}Ba^+$ has a high experimental state preparation fidelity [59]. This is due to the simplified hyperfine structure that limits off-resonant scattering errors. For the case of $^{133}Ba^+$, a simple optical pumping model can be assumed using the classical rate equations and in the limit of low intensity $<$ saturation [109]. The model assumes that there are four ground states pictured in Figure 2.4. In reality the ground states must in include the $5D_{3/2}$ hyperfine states, but in this model the branching ratio takes this decay into account. The model assumes there are two frequencies with the same polarization driving $F = 1 \rightarrow F' = 0$ and $F = 1 \rightarrow F' = 1$ transitions [59]. These transitions are either being driven resonantly or slightly of resonance, centered at the $|F = 0, m_f = 0\rangle$ and $|F = 1, m_f = 0\rangle$ states. There is a 5 Gauss magnetic field to split the hyperfine levels and the saturation parameter $s = I_{sat}/10$.

The pumping scheme in Figure 2.4 shows two different tones of the 493 nm transition being applied. This is done in order to properly pump out all of the ground states, save the ground that we want to prepare, $|F = 0, m_f = 0\rangle$. Due to the selection rules, each excited hyperfine state can decay to three out of the four ground hyperfine states. There are other possible schemes for preparing the $|F = 0, m_f = 0\rangle$ in $^{133}Ba^+$, like with π light, but due to the specific experimental set up, this is not possible. This specific pumping scheme has been shown in experiment to lead to high fidelity state preparation [59].

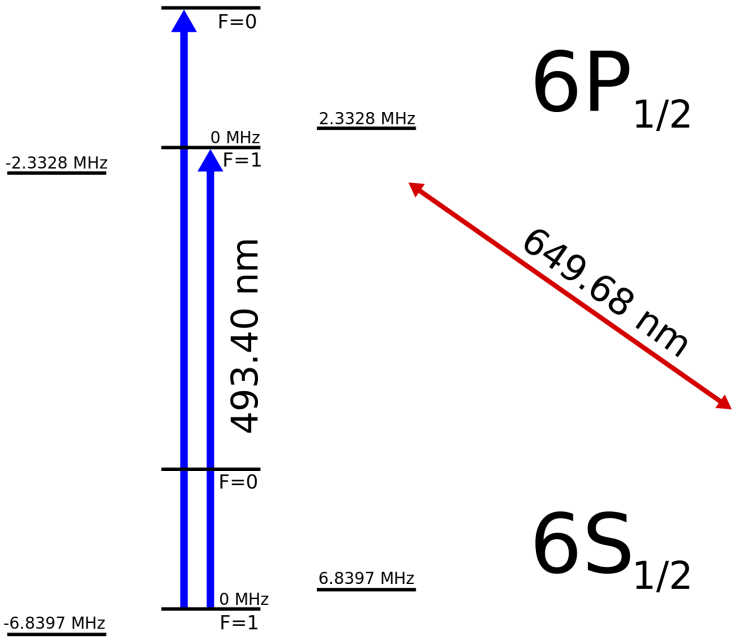

Figure 2.4: Simplified optical pumping model for $^{133}Ba^+$ in a 5 Gauss magnetic field, describing the pumping scheme in Figure 2.5c.

The population of each ground state P_n can be solved for by representing the time evolution based on the population of other ground states and the branching ratios [109].

$$\frac{d}{dt}P_n(t) = \sum_{j \neq n} P_j(t) \left[\sum_i R_{ji}\beta_{ji}\beta_{ni} \right] - P_n(t) \sum_i R_{ni}\beta_{ni}(1 - \beta_{ni}) \tag{2.6}$$

The index n refers to the ground state currently being solved, j is an index for the other ground states, and i are indices referring to the excited states. The change in the population $P_n(t)$ depends on the population of the states $P_j(t)$ that are coupled to $P_n(t)$ via allowed

dipole transitions that are either being driven or decaying with strengths proportional to the dipole transition strengths β_{ji} and β_{ni}. The population $P_n(t)$ is being pumped out at a rate proportional to dipole transition strength of the specific transition being driven β_{ni} and probability $1 - \beta_{ni}$ that after being driven, it will decay to a different ground state. The absorption rates R_{ji} and R_{ni} correspond to the absorption rates of the other ground states and the ground state being pumped, respectively.

$$R_{lm} = \beta_{lm} \frac{\Gamma_m}{2} \frac{I/I_{sat}}{1 + I/I_{sat} + (2\Delta_{lm}/\Gamma_m)^2} \tag{2.7}$$

This was solved in MATLAB numerically using ODE45. The set of Equations 2.6 can be put in a matrix representation and multiple sets of equations can be weighted to account for different transitions [109]. The general absorption rate R_{lm} can take into account Zeeman splitting with the detuning parameter Δ_{lm}.

This simplified model can help to quantify the impact of imperfect polarization or misalignment of an optical pumping beam from the quantization axis. An example is presented in 2.5, showing that for this simplified model of $^{133}Ba^+$ there is an optimal mixture of transitions to drive. The bottom two plots, 2.5c and 2.5d would not be used in an experimental setting. Pure π light on the 650 nm repumper would fail to pump out all hyperfine levels in the $5D_{3/2}$ state and the purely circularly polarized light completely fails to prepare the $|F = 0, m_f = 0\rangle$ state. A more complicated model that takes into account the $5D_{3/2}$ as additional ground states could provide more useful results or the application of this model to $^{137}Ba^+$ could help to quantify the impact of polarization impurities on the prepared state.

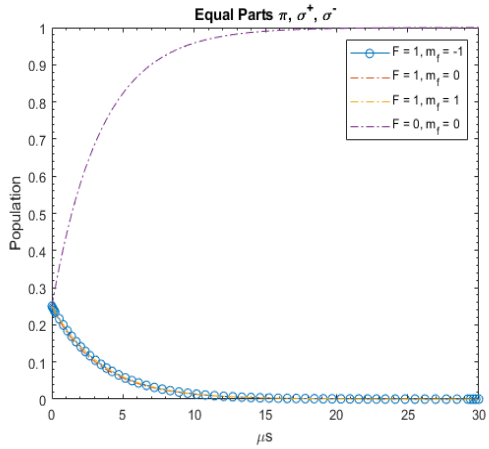

(a) Equal mixture of light.

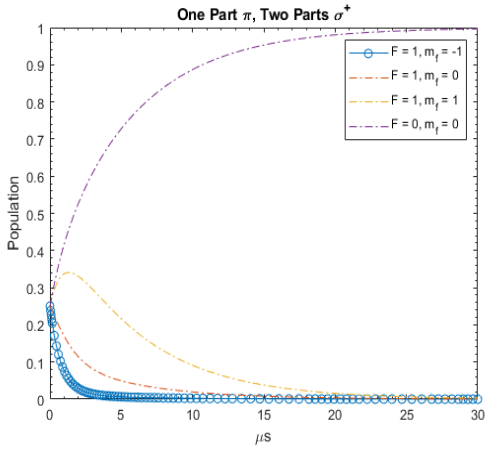

(b) Weighted towards σ^+ light.

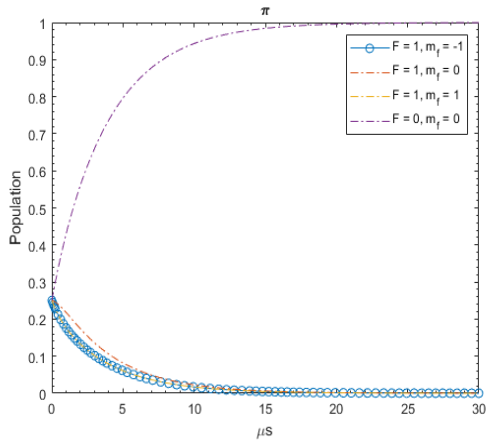

(c) Pure π light.

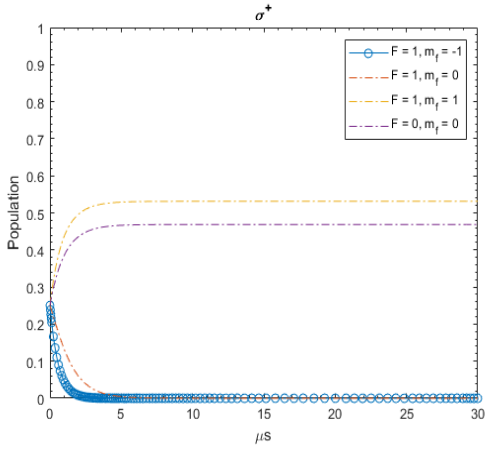

(d) Pure σ^+ light.

Figure 2.5: Preparation of the $|F = 0, m_\mathrm{f} = 0\rangle$ in $^{133}\mathrm{Ba}^+$ based on a simplified model.

Chapter 3

Continuous Wave Optics

In order to efficiently ionize and trap specific barium isotopes, prepare initial states with high fidelity, and perform shelving operations, many different beam paths need to be designed. These beam paths will give the user fundamental control of the ion by driving resonant atomic transitions that are used in the aforementioned processes. Many of the atomic transitions have similar wavelengths, but even these small deviations in the wavelengths need to be accounted for when designing beam shaping and focusing optics for driving multiple resonant atomic transitions with a single beam. In this section, the technical aspects of the optical designs for driving resonant transitions in barium are presented.

In total, the project plans to have ten independently controlled beam paths and seven different wavelengths. Five of these beam paths are continuous wave (CW) lasers, two of these beam paths are quasi-continuous (around 100 MHz), and three paths will be pulsed (Hz). The CW beam paths will drive resonant atomic transitions in $^{133}Ba^{+}$ like the cooling and measurement transition $6S_{1/2} \rightarrow 6P_{1/2}$, while the quasi-continuous beam paths will drive Raman transitions between $6S_{1/2}$ hyperfine levels, and the pulsed lasers will be used for ablation loading.

Each beam path consists of a few main sections, with various optical-mechanical devices allowing the remote control of power, polarization, and beam positioning throughout the entire path. The division of the optics into different sections eases trouble shooting, maintenance, and upgrades in these complicated, delicate systems. The majority of the work presented here focuses on the last two sections of the CW optics, beam shaping and beam positioning, before the beams enter the vacuum chamber and are focused at the ion.

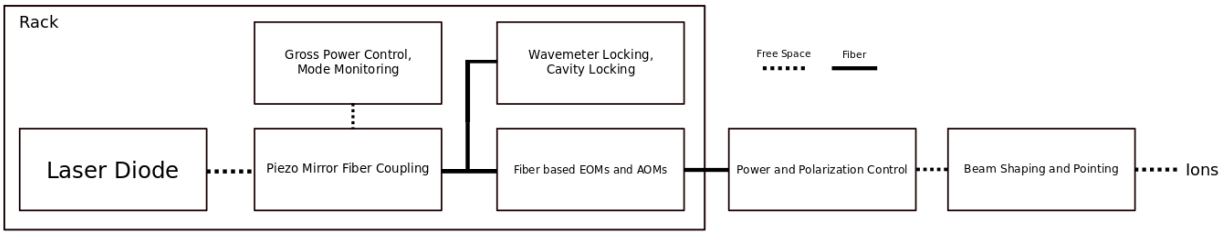

Figure 3.1: Broad overview of the optical system. The main focus of this section is on the final parts of the optical system, mainly the beam shaping and pointing.

Before progressing to the beam shaping and positioning portion of the optics it is necessary to take a look at the "up stream" optics that will polarize the light and be used to stabilize the intensity and frequency. These are common set ups used in many AMO experiments, but for consistency they are mentioned in this text.

The first three modules in the laser rack are meant to stabilize the laser frequency and power on a fundamental level before the light is distributed further down stream via fiber. Depending on the specific wavelength, the light is then taken to acousto-optic modulators (AOMs) and electro-optic modulators (EOMs) as well as a wavelength meter and a Fabry-Perot cavity. The AOMs are crystals that are driven at some acoustic frequency with a piezo-electric transducer that takes a radio-frequency (RF) input [97], imparting a frequency shift and diffraction pattern on the collimated input beam under the Bragg condition [96].

$$n\lambda = 2\Lambda \sin\theta \tag{3.1}$$

λ is the wavelength of light, Λ is the acoustic wavelength, n is the order of diffraction and θ is the glancing angle. For the Bragg condition to be valid and constructive interference to occur, the atomic spacing in the crystal must be an integer of the incident wavelength. The AOMs in this project are used mostly as fast switches, with the 1^{st} order being sent to the ion. These switches can operate in microseconds [97]. Most of the AOMs are fiber AOMs, and they are in a single pass configuration.

The EOMs in this project are used to create 1^{st} order sidebands that, along with the carrier frequency, can be used to drive transitions to different hyperfine levels that are split by a few GHz. The EOMs are used for phase modulation to create sidebands. An EOM is a crystal with a locally applied electric field that can vary in strength, varying the index of refraction, which imparts a phase shift on the light entering the crystal [98]. What is being exploited in this device is Pockel's effect.

$$E = E_0 e^{i\omega t}\left(\sum_{k=0}^{\infty} J_k(m) e^{ik\Omega t} + \sum_{k=1}^{\infty}(-1)^k J_k(m) e^{-ik\Omega t}\right) \tag{3.2}$$

Assuming that the input light is a plane wave and a sinusoidal potential is induced in the crystal due to an RF signal, the modulation can be written in terms of Bessel functions $J_k(m)$, the frequency of light ω, the amplitude of the RF signal m, and the frequency of the RF signal Ω [98]. The most power that can be transfered to the 1$^{\text{st}}$ order sidebands is 34% [98].

Besides the AOMs and EOMs, another major component is the wavemeter that will be used to lock the frequencies. The wavemeter is used more as a coarse locking and can have multiple different wavelength inputs, which is useful for setting initial calibration parameters. Again, wavemeters, AOMs, and EOMs are all standard devices that give AMO experimentalists basic controls in the lab, but there is some variation in this project depending on the exact beam path.

After the initial frequency, amplitude and polarization control of the beams provided by these components the beams will be shaped and focused at the ions. This chapter provides simulated beam shapes from different telescopes based mostly on refractive optics. It also provides basic motivation for why these telescopes exist, and what transitions will be driven in $^{133}Ba^{+}$. It compares and contrasts different designs and provides a basic introduction to Gaussian optics and Zemax's OpticStudio.

3.1 Optical Design Overview

There are two main modes with which the QuantumIon experiment can operate, depending on whether or not the researcher wants to utilize qubits or qudits. Figure 3.2 is the qudit orientation of QuantumIon and serves as an example of the most complicated beam orientation of the trap. The laser beam orientation is fixed, but it is possible for researchers to change the trap axes and the magnetic field direction, which gives control over the quantization axis. The qubit laser orientation is simpler, and actually a subset of the qudit orientation with a change to the magnetic field orientation.

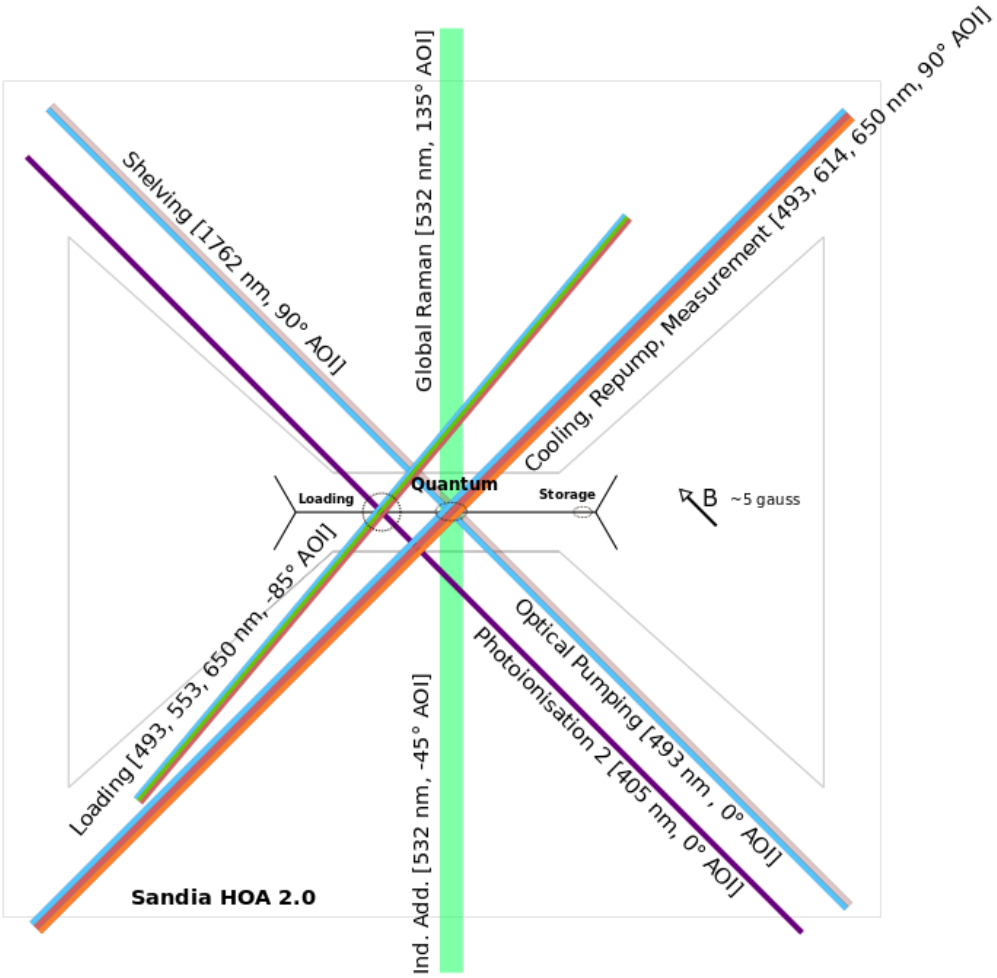

Figure 3.2: A top down figure of the Sandia Chip HOA 2.0 trap, featuring three zones. The angle of incidence (AOI) is taken with respect to the quantization axis. The center to center distance from the quantum zone to the loading zone is 980 microns. The center to center distance from the quantum zone to the storage zone is 1540 microns.

The quantum zone, in the center of the trap, will be where ions can be individually addressed and entangled. The addressing system is being designed for 16 individually addressable ions plus 2 buffer ions on either side of the chain, for a total of 20 ions. The

buffer ions in conjunction with fitting the trap potential to some optimal quartic function [10], can help to maintain a more even spacing between the center 16 ions in the chain, which is important as the telecentric individual addressing optical system is designed to focus onto ions that are evenly spaced (4 μm).

At the quantum zone there are counter-propagating Raman beams to drive transitions between hyperfine levels, there is also linearly polarized light to measure and cool the ions, as well as repump out of the metastable $5D_{3/2}$ and $5D_{5/2}$ levels. The shelving, 1762 nm, is limited to driving $\Delta m_f = \pm 2$ hyperfine transitions rather than the typical $\Delta m_f = 0$ orientation used to drive quadrupole transitions [46]. There is also a circularly polarized optical pumping line to drive $\Delta m_f = \pm 1$ transitions, which is used for state preparation of qudits.

The next zone is the loading zone, which will have three targets available from which ions can be loaded. This allows targets with different barium isotopes to be installed in the trap, however, only two of these targets will allow for isotope-selective loading with the current optical design. The loading zone is chosen such that it is the farthest distance away from the quantum zone, while still allowing beams to pass without clipping an appreciable amount on any portion of the vacuum chamber or trap (power clipping $\leq 10^{-6}$ watts, assuming the power level is normalized and Gaussian). Sandia National Laboratories provides a summary of the clipping power as function of beam waist [51], however these are for ytterbium wavelengths and only correspond to the shortest distance across the isthmus.

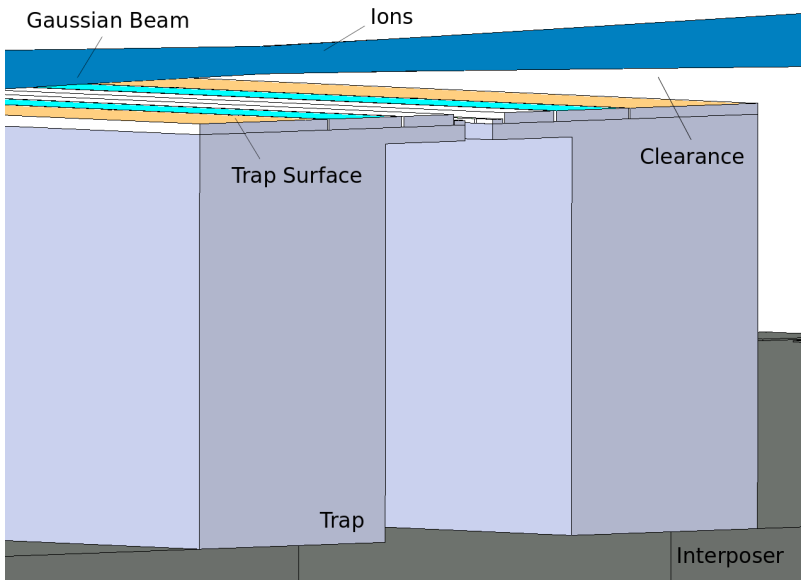

Figure 3.3: Partial cross-section of the Sandia HOA 2.0 Trap with a Gaussian beam traveling across the surface. Note that this beam is only a qualitative example, but it highlights one of the pitfalls of surface traps, being the relatively low NA across the trap. That being stated, there are ways to increase the NA of surface traps by using bump bounds rather than wirebonds [52]. The NA perpendicular to the isthmus is 0.11, the NA at 45° is 0.08.

Finally, the measurement zone in this case is really just the quantum zone. In order to preserve states, ions will have to be shuttled to the storage zone while measurement is performed at the center of the trap. Fast shuttling with minimal motional heating has been demonstrated in surface traps, which is done by applying an increase to the voltage of the electrode for a very short period (hundreds of nanoseconds) at which the experimentalist wishes the ion to stop [65]. This "kick" can be optimized and the ions can be shuttled over hundreds of microns in microseconds. This is an important realization because it means that in the event measurement needs to take place on only select ions, the ions that need to have their state preserved can be shuttled to the edge of the trap. The edge of the trap is 1610 microns away from the center of the quantum zone and is defined by the beginning of the transition zone and Y-Junction [66]. The Y-Junction has very high motional heating rates compared to the center area and is mostly meant for loading in this trap design, although this project will be not utilizing this zone for loading. Since measurement with trapped ions takes milliseconds and these shuttling operations can take place in microseconds, the motional heating rate causing decoherence will be dominated by the base trap heating rate and not heating due to slow shuttling. The base heating

rate for this trap is about 100 quanta/second [51]. This informs the optical engineering by allowing the assumption be made that ions can be shuttled to the edge of the trap, providing room for larger beams and a more consistent power level across the ion chain.

The rest of the chapter will focus on telescope designs. The telescopes were designed for longer focal lengths to allow for more room between the vacuum chamber and the telescope. This extra room allows for necessary beam positioning components to be placed after the beam has started to focus. The typical focal lengths for the telescopes are 400-500 mm. The in-vacuum length of the beam path, from the ion to the outer viewport, is $\approx$ 130 mm, giving 200-300 mm for other components. The target telescope focal lengths are longer than typical telescopes used for addressing ions, which range closer to a couple hundred millimeters. An overview of the optomechanical design used for beam positioning can be found in Appendix C.

3.1.1 Design Considerations

The CW optics were designed on two major assumptions, that the machine needs to be able to correct slow drifts (relative to experimental timescale) in position, power, polarization, and frequency without the need for an operator in the experiment room and that each beam needs to be separately controlled to prevent positional coupling of two different beams at a trapping zone. The former demands the inclusion of beam position monitoring devices, piezoelectric stages and mounts, photodiodes, cameras, etc. Since these items take up significant real estate around the vacuum chamber, the CW telescopes were designed for longer focal lengths to allow for beam positioning devices near the chamber. Space is also needed to filter and pick off beams that share a common viewport. The beam positioning and sensing components are placed after the beams have started to focus, so that deliberate changes in the beam position will not impact the beam quality. The majority of the focal lengths for the CW telescopes are 400-500 mm. Beam pointing stability has been demonstrated in ion trapping experiments utilizing 200 mm focal lengths, allowing the position to be stabilized such that the estimated gate error due to positional drifts changing the intensity is on or below the 10^{-6} level per gate [81].

Once the focal lengths of the telescopes had been decided, the next step is to determine how to shape each beam such that the power is relatively uniform across the ion chain. At the quantum zone there will be 20 ions with 16 ions that can be be individually addressed. Assuming a 4 μm spacing between the center 16 ions and the beams being 45° with respect to the trap axis, the beams require a high level of power uniformity along $\approx$ 45 μm. In general, this requires a beam waist $\approx$ 200 μm for $>$ 95% intensity uniformity. The

uniformity is important for almost all operations, but a specific example that could be taken is the measurement of a chain of ions. If an ion on the edge of the chain is being measured with less intensity, it may not fluoresce enough in the measurement time window to count as a bright state, thus being improperly considered dark.

Taking into consideration the axis of the beam that does not span the ion chain, one finds that the beam waist must be much smaller to avoid clipping the trap appreciably, scattering light and destroying the Gaussian mode. The target for this is to keep the power clipping at $\leq 10^{-6}$ level. This corresponds to beam waists anywhere from 5 - 25 μm depending on the wavelength. Ideally these beam waists would be ≈ 22 μm to reduce intensity fluctuations at the ion from beam pointing instabilities and still not clip significant power on the trap.

Following these desired beam waists at the ion and the focal lengths dictated by the desired optomechanical design, collimators can be chosen such that they benefit the telescope design. These collimators are connected to fibers that transfer light from the optical rack to the optical table and they are the starting point for designing the beam shaping optics. Depending on the wavelengths shown in Figure 3.2, the largest standard collimator (FC) from Schäfter and Kirchhoff was chosen. This reduces the telescope footprint on the optics table because it requires less magnification. There are non-standard larger collimators available which would also reduce the telescope footprint, but the optomechanical devices that are being implemented are for 1 inch optics. Anamorphic beam shapers could reduce the footprint, but they attenuate the beam power significantly more than simple lenses, so these should only be implemented when space constraints demand it. Neither anamorphic beam shapers nor larger collimators reduce the arm length of the telescopes, so it likely would have little impact on increasing the pointing stability.

Once the focal length and AR coatings of the collimators had been decided, the only step left is to independently reshape the two beam axes so that when focused with a standard positive singlet it yields the desired beam waists at the ion. This beam shaping was done with standard cylindrical singlet lenses for the monochromatic beams and achromatic cylindrical doublets for the combined beams. Cylindrical lenses only focus along one axis and leaves the other axes untouched. The use of a standard singlet to do the final focusing is important otherwise the two different beam waists will be focused to different positions along the optical axis.

The beam shaping was done with lenses rather than dielectric concave mirrors or parabolic mirrors. The main challenge with using lenses in these optical designs is that many beams have multiple wavelengths that will disperse differently when refracting, resulting in focal shifts at the ion. Concave mirrors do not have any chromatic aberrations,

and parabolic mirrors do not have chromatic or spherical aberrations. There is a design in Section 3.5.1, which utilizes mirrors to create elliptical beams, but the footprint is significantly larger than the telescopes utilizing lenses. Parabolic mirrors were not considered for these designs because they are difficult to align and in some cases the machining process can cause the finish to be rough introducing diffraction patterns to the beam.

3.2 Optical Simulations

This section is meant to provide a very brief introduction to how OpticStudio works as well as basic resources to get started. There is also a section describing Gaussian optics, which can be applied to all the designs in this text. Finally, there is background relating to aberrations found in the designs.

3.2.1 OpticStudio

The majority of the optics work has been done in Zemax's OpticStudio, which is a ray tracing package originally released in the 1990s that models light propagating through an optical system [67]. This allows users to diagnose and quantify aberrations while optimizing their system. The package can calculate light propagating through an optical system using geometrical optics, Gaussian optics, and physical optics. Geometrical optics models light as rays originating from point sources which either reflect or refract at a surface. Gaussian optics also models light as an individual rays, but it makes a small angle approximation for rays traveling close to the optical axis. This is a subset of geometrical optics. Physical optics models light as a wave, which can take into account phenomena such as diffraction and interference, whereas geometrical optics generally cannot.

There are two main modes in OpticStudio, sequential and non-sequential. The results here uses the sequential mode wherein which rays are traced through the system in the order that they are listed in the lens data editor. Sequential mode is the default setting in OpticStudio and should be used except in niche cases. Important resources for someone using OpticStudio include the manual https://neurophysics.ucsd.edu/Manuals/Zemax/ZemaxManual.pdf and the company website which has articles posted by optical engineers that provide many useful case examples https://my.zemax.com/.

There are many useful tools in OpticStudio that allow a user to diagnose aberrations or constraints in their system, but optimizing an optical system is done with the merit function. The merit function allows users to input operands which can be assigned a

certain weight. The more weight given to an operand, the more importance is placed on that operand when OpticStudio is asked to optimize a system. There are many operands in OpticStudio, but one example is "EFFL", which optimizes the optical system based on the assigned variables to a desired effective focal length. This is particularly useful for designing lenses. There are many operands and chances are at least one exists for navigating to an acceptable solution. On one final note, tolerancing is also possible in OpticStudio which is necessary since most lens manufacturers machine lenses with dimensions up to a certain precision.

3.2.2 Performance Criteria

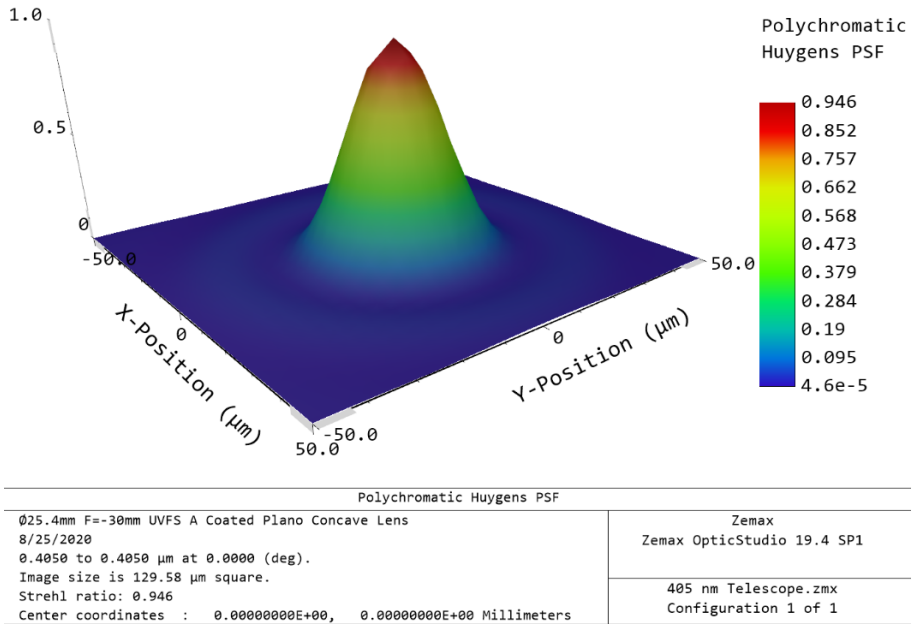

Figure 3.4: Huygens point spread function of the 405 nm beam at the ion. Point spread functions > 0.8 are considered diffraction limited.

In practice, when evaluating optical systems it is important to use all the tools available to search for limiting factors. A typical starting evaluation of the performance of an optical system can be the point spread function (PSF), which is shown in Figure 3.4. With Zemax's OpticStudio ray tracing, objects are modelled as point sources, and due to mostly spherical aberrations in this case, these rays are prevented from converging on one image plane. The

PSF captures these deviations and is used to find a relative intensity in the image plane, causing interference, which produces irregularities in the phase and intensity. The intensity of light at the image plane can be calculated from the calculated PSF convoluted with the object plane [79].

$$Image(x, y) = PSF(x, y) * Object(x, y) \tag{3.3}$$

This specific PSF in Figure 3.4 is the Huygens PSF, which models each ray propagating from the object as a small wave, so it can account for phenomena like diffraction [80]. The Huygens spread function takes more computational time, but it is accurate in more situations than the fast-fourier transform spread function [80].

$$S = e^{-(2\pi\sigma)^2} \tag{3.4}$$

The Strehl ratio S can be approximated when there are small amounts of aberrations, where σ is the root-mean-square (RMS) of the optical path difference (OPD) [78]. The Strehl ratio is the peak of the PSF in Figure 3.4.

It is not easy to exactly predict how an optical system will perform based on the calculated aberrations, nor is it easy to relate aberrations to their exact impact on the image, but there are specific criteria in optical designing, that if met, deem the optical design acceptable. The two criteria, although more exist, used to evaluate all of the CW telescopes are the Rayleigh and Marechal criteria [78]. Meeting the Rayleigh criterion requires the optical path difference at the focus to be $< 1/4$ waves. The Marechal criterion is met if the Strehl ratio is > 0.8 [78]. Meeting these criteria generally indicates the system will be diffraction limited. These are not hard and fast rules, but they are a standard. These standards are met for all of the CW telescopes in the project.

There are many other tools used in OpticStudio to evaluate the performance of these systems, but they are all related to each other in at least one way so there is some redundancy. It is important to check these for consistency, but for all practical purposes the PSF in addition to the OPD is sufficient for evaluating the monochromatic beams presented in this text.

3.2.3 Gaussian Optics

All of the beams in the following sections can be described as Gaussian, however this does not always hold when beams are focused to only a couple microns. The intensity I of a

Gaussian beam can be described as a function of the beam waist $w(z)$, power P, and radius r.

$$I(r,z) = \frac{2P}{\pi w(z)^2} \exp \frac{-2r^2}{w(z)^2} \tag{3.5}$$

This is necessary for estimating the amount of power at other zones in the trap due to neighboring beams (crosstalk) as well as the amount of power that is clipping on the trap. The beam waist can be calculated from the Raleigh range z_r and the beam waist at the focus w_0. This specific waist w_0 corresponds to a radius at which the relative intensity has dropped to $1/e^2$ of the initial value.

$$w(z) = w_0 \sqrt{1 + \frac{z^2}{z_r^2}} \tag{3.6}$$

The Raleigh range is a measure of how quickly the beam diverges and depends on the beam waist at the focus as well as the wavelength λ.

$$z_r = \frac{\pi w_0^2}{\lambda} \tag{3.7}$$

In order to address a chain of ions with a global beam in a surface trap it is necessary to create elliptical beams with cylindrical lenses. Cylindrical lenses focus only one axis of light. This allows a designer to treat two axes independently so that two different beam waists can be created at the ion chain. Most beams have waists that are 20 microns x 200 microns. The smaller beam waist is necessary to fit over the trap and the longer beam waist is necessary to span the length of the ion chain. The longer beam waist is also determined by the desired intensity uniformity from the center ion to the last ion in the chain as well as the crosstalk that occurs at the other trapping zones.

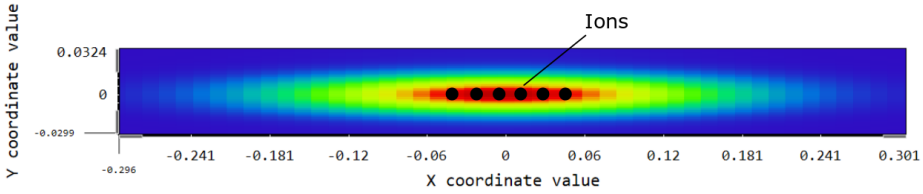

Figure 3.5: Typical beam that is ideal for addressing a chain of 16 ions in the Sandia HOA 2.0 trap. The beam was simulated with cylindrical lenses allowing the focus to have different beam waists depending on the axis. The units are in millimeters. The ion spacing is exaggerated.

3.2.4 Aberrations

An aberration is a generic term for unwanted deviations from a perfect plane wavefront. These are naturally occurring, dependant on the types of optics in the system, and can be broken down into monochromatic and chromatic aberrations [68]. The former can be described by Zernike polynomials wherein which lower and higher order terms contribute independently to wavefront deviations based on the type of aberration that has occurred. Chromatic aberrations can be either transverse or longitudinal, where light of different wavelengths focus at different positions [69].

Zernike polynomials are orthogonal on the unit circle, so this is typically the domain to which they are typically limited. They are the mathematical formalism that is commonly used to describe a wavefront, even when the wavefront is complex and lacking symmetry [70]. The Zernike polynomials in conjugation with their coefficients give a complete description of the wavefront.

$$W_n^m(\rho,\theta) = \sum_{m,n} C_n^m \, Z_n^m(\rho,\theta) \tag{3.8}$$

This describes a wavefront $W_n^m(\rho,\theta)$, valid within the unit circle, where C_n^m is a coefficient for a specific polynomial and Z_n^m is the polynomial itself [71]. The coefficients can be determined by fitting the polynomials to a measured wavefront. This is in polar coordinates, where ρ is the radius confined to the unit circle, θ is the polar angle. There are many other equivalent formalisms of Zernike polynomials in different systems [71].

$$Z_n^m(\rho,\theta) = R_n^m(\rho)\, \cos(m\,\theta) \text{ for m} \geq 0 \tag{3.9}$$

$$Z_n^{-m}(\rho,\theta) = R_n^m(\rho)\, \sin(m\,\theta) \text{ for m} < 0 \tag{3.10}$$

$Z_n^m(\rho,\theta)$ describes the real components of the full polynomial, $Z_n^{-m}(\rho,\theta)$ describes the complex components, and $R_n^m(\rho)$ is the radius function. The radius function must be 1 on the edge of the unit circle to ensure proper normalization.

$$R_n^m(\rho) = \sum_{a=0}^{\frac{n-m}{2}} \frac{(-1)^a\,(n-a)!}{a!\left(\frac{n+m}{2}-a\right)!\left(\frac{n-m}{2}-a\right)!}\,\rho^{n-2a} \tag{3.11}$$

This is valid for a circular aperture, but with the correct basis transformation, elliptical apertures can be fitted [71].

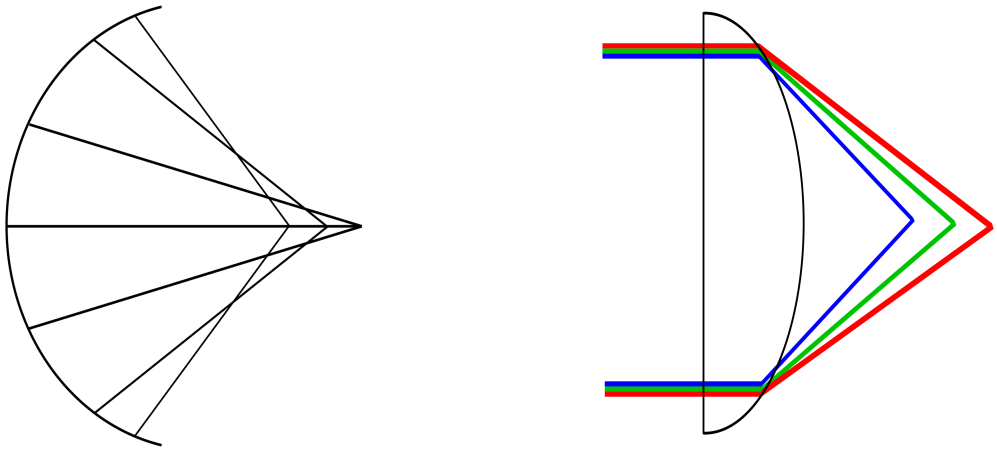

(a) Spherical aberrations. (b) Longitudinal chromatic aberrations.

Figure 3.6: Two of the most common aberrations found in the following sections.

The aberrations in the monochromatic telescopes are dominated by the spherical aberrations introduced by the refractive optics, while the polychromatic telescopes also have to deal with focal shifts along the longitudinal and transverse directions due to the variation in wavelengths. The monochromatic aberrations in all of the following designs are dominated by fourth and sixth order Zernike polynomials relating to spherical aberrations. These are Z_4^0 and Z_6^0, respectively, where $R_4^0 = 6\rho^4 - 6\rho^2 + 1$ and $R_6^0 = 20\rho^6 - 30\rho^4 + 12\rho^2 - 1$. Aspheric lenses are specifically designed to help reduce these spherical aberrations, but since the majority of the beams are rather large at the focus these aberrations do not impact the beam quality significantly. This would be more of an issue if the beam was being focused to a waist of a few microns.

Besides spherical aberrations, chromatic aberrations are present in the combined beams. In an optical system, aberrations that occur along the longitudinal optical axis can be referred to as "axial color". In any medium besides a vacuum, light of different wavelengths λ experiences a change in phase velocity which causes dispersion. This change in velocity depends on the frequency of the light and this is what is occurring in Figure 3.6b, causing the wavelengths to focus at different positions on the optical axis. The index of refraction n for a given medium can be described by the Sellmeier equation [72].

$$n^2(\lambda) = A + \frac{B\lambda^2}{\lambda^2 - C} + \frac{D\lambda^2}{\lambda^2 - E} \tag{3.12}$$

The coefficients $A, B, C, D,$ & E are measured experimentally, and more terms can be added to improve the fit. The wavelength λ is given in microns. Having the Sellmeier

coefficients allows one to find the dispersion of the medium.

$$V = -\frac{\lambda}{c}\frac{d^2 n(\lambda)}{d\lambda^2} \tag{3.13}$$

While this is a useful result, commonly optical engineers rely on the specific Abbe number of a given glass when designing lenses that reduce chromatic aberrations [72].

$$v = \frac{n_d - 1}{n_f - n_c} \tag{3.14}$$

The Abbe number is related to dispersion, where n_f, n_f, and n_c are the indices of refraction of the corresponding Fraunhofer lines. Flint glass usually has higher dispersion, while crown glass has lower dispersion. Achromatic lenses reduce chromatic aberrations by eliminating the effects of the dispersion by coupling two or more pieces of glass that have significantly different Abbe numbers. Achromatic lenses can be doublets, triplets, or even more depending on how many wavelengths need to be corrected [73].

3.3 Loading Telescopes

3.3.1 405 nm Photoionization Telescope

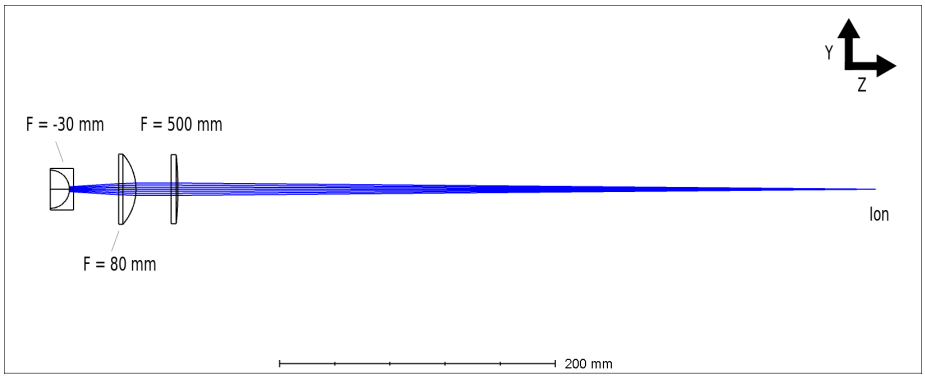

Figure 3.7: Ray tracing of the 405 nm Photoionization Telescope. The first two lenses re-collimate the beam and the final lenses focuses it at the ion.

The 405 nm telescope will be used to drive the non-resonant ionization transition after neutral barium has been excited to the $6P_1$ state. It will be focused at the loading zone.

Figure 3.7 shows the beam shaping optics that will be used to take a collimated 405 nm beam and re-collimate the beam to a larger diameter before being focused with a 500 mm plano-convex lens. Negative lenses are used to save space. The magnification $M \approx 2.66$, which was chosen so that the beam waist $w_0 \approx 18\,\mu m$ at the ion. This waist provides enough clearance over the trap such that there is minimal clipping on the trap itself as well as the interposer. The space between the ion and the focusing singlet is left for beam positioning and sensing optomechanical devices. The spacing between the focusing singlet and the beam shaping optics will be exactly determined by the mounts. The focusing singlet will be mounted on a piezoelectric motor z-axis stage to allow for $< 1\,\mu$m steps of the focus at the loading zone.

This is the shortest telescope in the project and the waist is circular at the ion. This keeps the ionization volume smaller in comparison to the elliptical beams used for addressing the ion chains. The smaller ionization volume reduces the loading efficiency, but it allows ions to be trapped closer to the trap minimum preventing considerable acceleration of the ion, which would heat other ions that have already been trapped [123]. This is the only circular beam in the system, besides the ablation paths. The PSF is well above the Marechal criteria, which was shown earlier in Figure 3.4. More information on this telescope can be found in Table C.1 and C.2.

3.3.2 493, 553, & 650 nm Loading Telescope

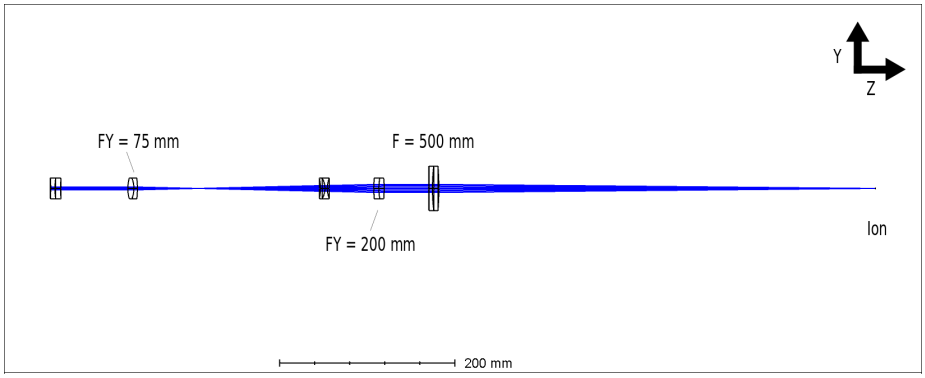

(a) Y-axis view of the telescope. FY corresponds to cylindrical lenses focusing on the y-axis. Magnification in y-axis $M_y \approx 2.66$.

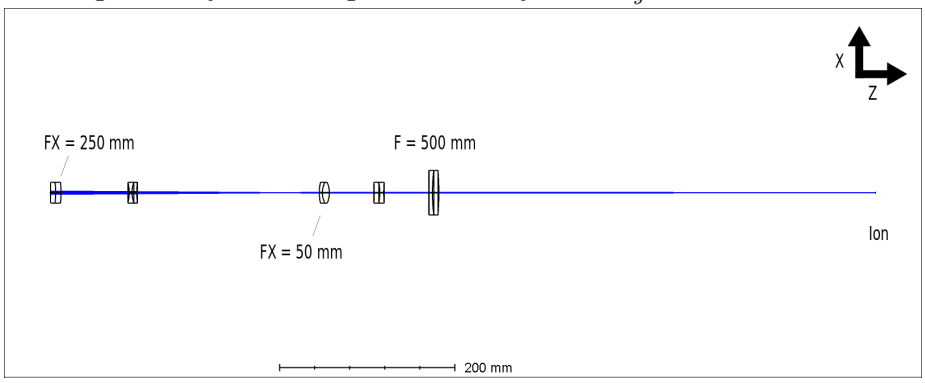

(b) X-axis view of the telescope. FX corresponds to cylindrical lenses focusing along the x-axis. Magnification in x-axis $M_x \approx 1/5$.

Figure 3.8: Ray tracing of the combined 493, 553, and 650 nm loading beam.

The loading telescope will be used to excite the neutral barium atoms and cool after ionization. The beam is 5° from parallel to the cooling, measuring, and repumping (CRM) beam at the quantum zone, so that the beams can be spatially separated and picked off after passing through the vacuum chamber. Spatial separation of the loading beam and the CRM beam is necessary because they contain the same frequency of light, so they cannot be separated with dichroics.

Since the loading zone is 980 microns from the quantum zone, it may be possible to store a reservoir of ions at this location so that the quantum zone can be loaded more quickly in the event ions are heated or kicked from the trap. If the ions are crystallized it

may be possible to store > 20 ions at this location. The elliptical shape of the loading beam would allow many ions to be cooled. The 553 nm beam drives the $6S_0 \rightarrow 6P_1$ transition so that the 405 nm beam can ionize the atoms.

The telescope itself is made of five lenses. Two lenses are used to reshape the collimated beam entering the telescope on the left of Figure 3.8 along the x-axis and two lenses are used to reshape along the y-axis. The final lens focuses both axes at the ion. The beam shaping lenses are cylindrical achromats and the focusing lens is a standard achromatic doublet. The lenses reshaping the x-axis and y-axis are interleaved to save space and negative lenses are not used because they are difficult to source, however, they can be designed. There is considerable space between the ion and the telescope that will be filled with sensors. The beam waists at the ion depend on the wavelength, but they range from $w_{y0} \approx 17 - 22\,\mu m$ for the y-axis and $w_{x0} \approx 200 - 240\,\mu m$ for the x-axis.

Figure 3.9 holds pertinent information relating to the optical performance of the loading telescope. In particular, analyzing the impact of dispersion on the focal points of the different wavelengths contained in the beam is necessary to ensure that all wavelengths clear the trap. There is minimal lateral chromatic aberrations, aberrations that would move the focus of different wavelengths above or below the optical axis. The longitudinal chromatic aberrations do however need to be considered in this design. In this case, the ideal image plane of the 553 nm portion of the loading beam is $\approx 650\,\mu m$ behind the 493 nm image plane. The image plane of the 650 nm beam is $\approx 900\,\mu m$ past the 493 nm image plane. This causes slightly more clipping on the trap, but it is well below an order of magnitude increase, so the Gaussian nature of the beam will still be present after passing the ions. This is important because significant scattering of 493 nm will cause decoherence in ions that are in other parts of the trap and the design intends to reimage the beam onto a CCD after it has passed through the vacuum system.

Reducing axial color in a system can be done by using shorter focal lengths, designing multiple achromatic lenses together or designing apochromats, or implementing concave mirrors for the final focusing. The axial color compounds at every lens and is exacerbated at longer focal lengths. The axial color is shown in Figure 3.9b, with the entrance pupil being defined by the collimator output that has a 1.72 mm beam waist. The chromatic aberrations are reflected in the optical path difference (OPD) as well as the ray-fan plot (RFP). The RFP uses marginal rays, which are rays on the edge of the entrance pupil and looks at the difference between where these rays land on the image plane compared to the optical axis. The OPD plots the difference of each successive ray relative to the optical axis across the pupil at the image plane. Without aberrations, the OPD and RFP would have values of 0 across the normalized pupil.

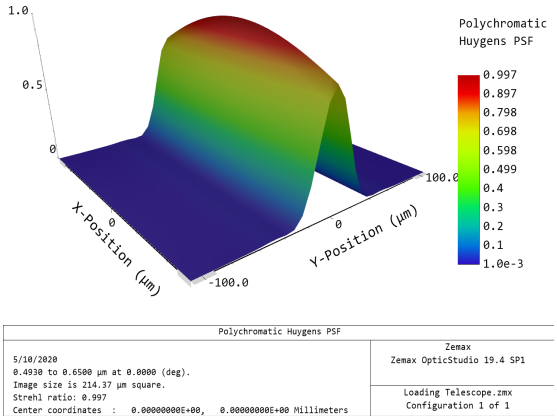

(a) An almost ideal point spread function ensuring diffraction limited performance.

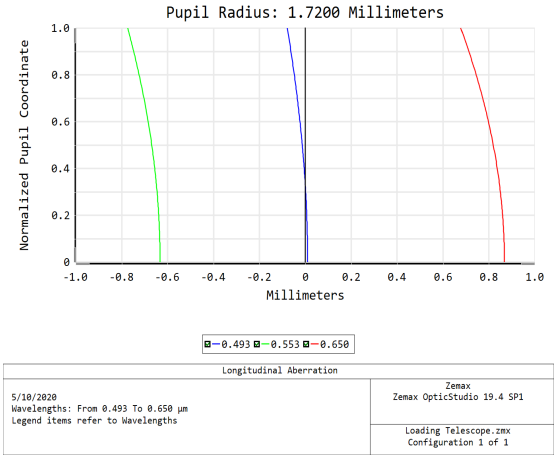

(b) Longitudinal chromatic aberrations, showing < 1 mm shift in focus between the different wavelengths.

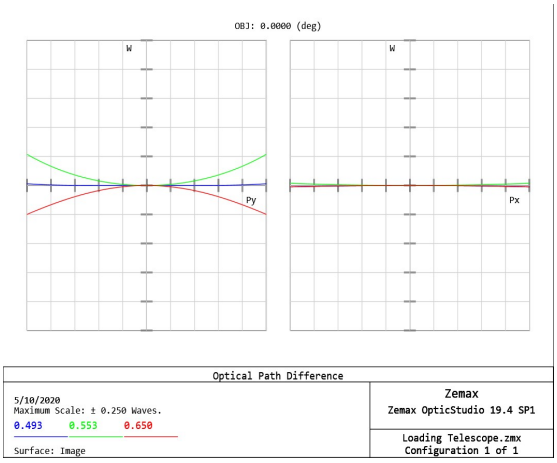

(c) Optical path difference scaled to 1/4 waves, again highlighting the diffraction limited performance.

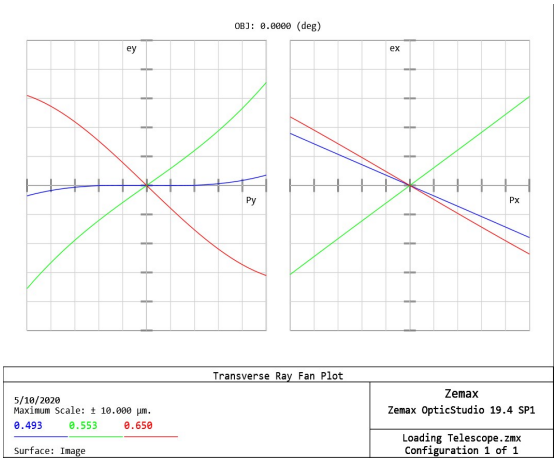

(d) Ray fan plot, dominated by defocus of the green and red wavelengths, but otherwise demonstrating the minimally aberrated system.

Figure 3.9: Various plots showing the loading beam telescope has relatively low aberrations and will be diffraction limited.

Figure 3.9d plots this distance against the normalized pupil coordinate. Although small in comparison to the 553 nm and 650 nm aberrations, the 493 nm RFP shows characteristic spherical aberrations with a shape similar to that of a cubic function. The aberrations in the 553 nm and 650 nm beams are dominated by defocusing along the optical axis,

corresponding to the Zernike polynomial Z_2^0 with a coefficient, $R_2^0 = 2\rho^2 - 1$. There are also spherical aberrations present. The OPD is scaled to 1/4 waves, corresponding to the Rayleigh criteria. The interference, reflected in the OPD caused by spherical aberrations, at the image plane is well below the 1/4 wave limit.

To frame these chromatic aberrations better, consider the trap dimensions and the Rayleigh range of the beams. The trap has an isthmus which is 1.2 mm and the beam is travelling 40° from perpendicular to the isthmus giving an effective travel distance of ≈ 1.56 mm across the trap surface. If the defocus on the 553 nm and 650 nm is such that they are ≈ 650 μm and ≈ 950 μm from the image plane, respectively, then the 553 nm would still be focused over the trap, while the 650 nm focal point would be slightly off of the trap surface. This is assuming that the 493 nm is perfectly focused at the ions. Another way to look at this is to look at the Rayleigh range in the y-axis, this is the range at which the beam cross section is twice its original value. The Rayleigh range for these wavelengths and beam waists are > 2 mm, so the defocus would cause the beam waists to be only a couple of microns larger at the loading zone, corresponding to beam radii of ≈ 21μm and ≈ 23.5μm for the 553 nm and 650 nm beams, respectively. The beams are still able to clear the trap below the 10^{-6} power level. The axial color could be further reduced by using a concave mirror to do the final focusing, but this only results in ≈ 100 micron reduction in the error. This combined with the > 0.99 polychromatic PSF in Figure 3.9a makes this a viable design choice for the loading beam. More information on this beam can be found in Table C.3 and C.4.

3.4 Cooling, Measuring, and Repumping Telescopes

The cooling, measuring, and repumping (CRM) beam is arguably the most important CW beam in the system, as this provides the ability to Doppler cool the ion, measure the ion, and pump out of the long lived metastable $5D_{3/2}$ and $5D_{5/2}$ states. This is the bread and butter of the CW optical beam paths and will be used in every experiment. Without this, the user lacks even the most rudimentary control of the ions.

3.4.1 493, 614, & 650 nm Telescope

The design for the 493, 614, & 650 nm CRM beam is very similar to the loading telescope design except the beam is reshaped so that it can be focused with a 400 mm lens rather than a 500 mm lens. This reduces the axial color such that the 614 nm and 650 nm focuses ≈ 500 μm from the focus of the 493 nm light.

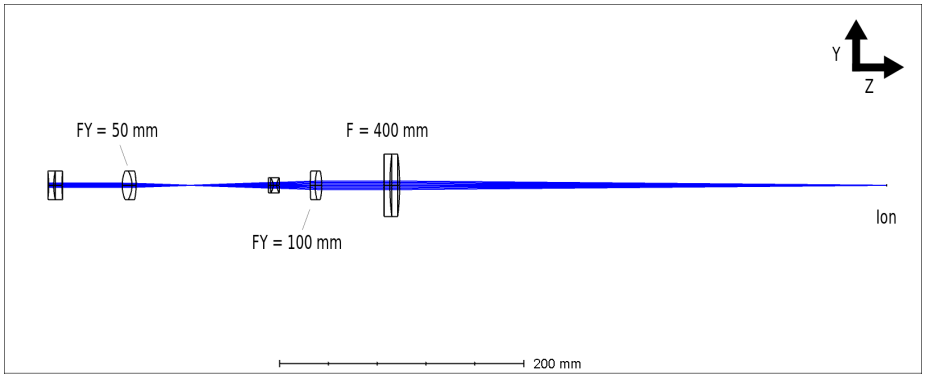

(a) Y-axis view of the telescope. FY corresponds to cylindrical lenses focusing on the y-axis. Magnification in y-axis $M_y \approx 2$.

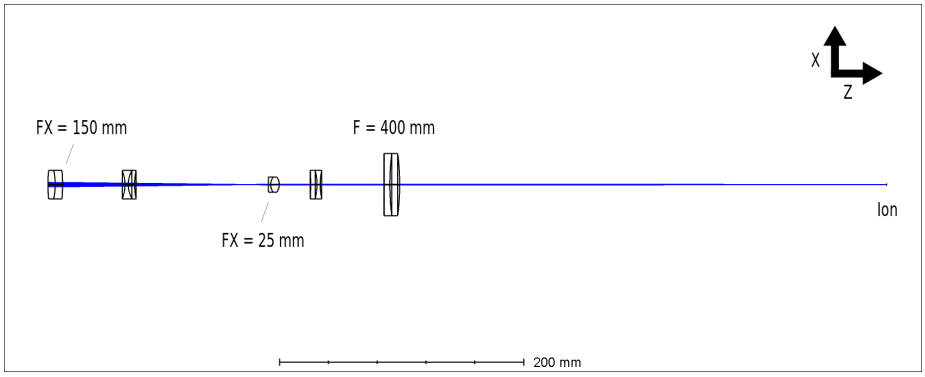

(b) X-axis view of the telescope. FX corresponds to cylindrical lenses focusing on the x-axis. Magnification in x-axis $M_x \approx 1/6$.

Figure 3.10: Ray tracing of the combined 493, 614, and 650 nm CRM beam.

The spherical aberrations in this design are low, with the most evident aberration in the RFP being the defocus. Again, this will cause a negligible amount of increased power clipping on the trap itself. The design meets the previously mentioned criteria and will be diffraction limited.

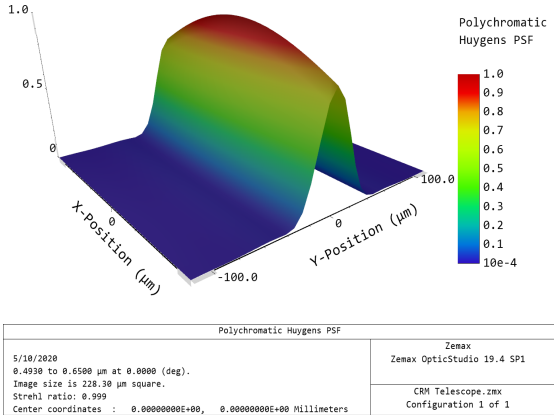

(a) High polychromatic point spread function, meeting the Marechal criterion.

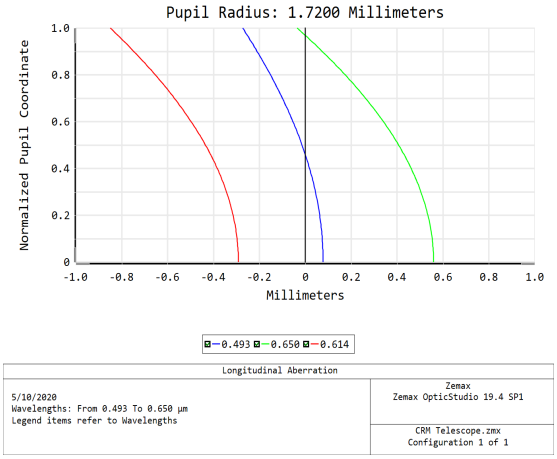

(b) Longitudinal chromatic aberration with < 1 mm focal shift over a 400 mm focusing distance.

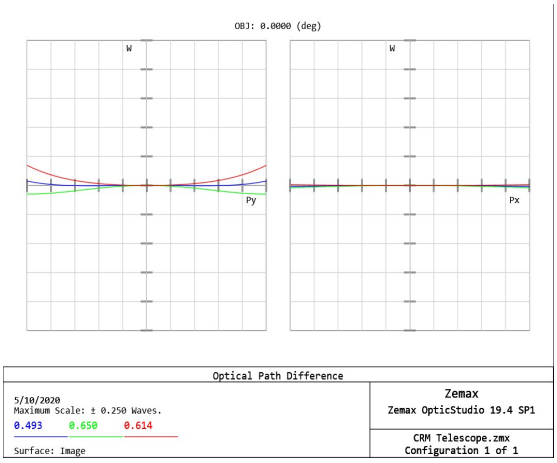

(c) Optical path difference plot scaled to the Rayleigh criterion. The simulated aberrations are $< 1/20$ waves.

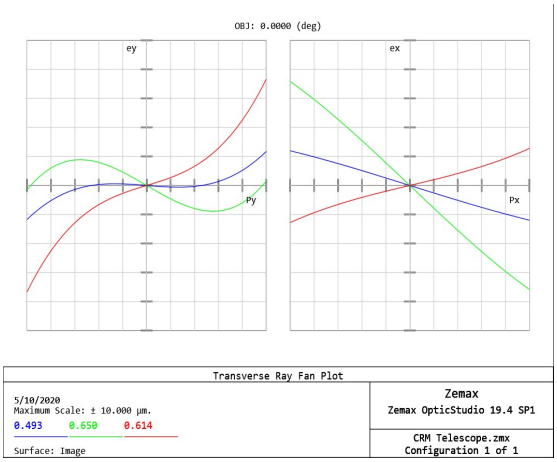

(d) Ray fan plot showing both spherical and defocus aberrations present in the CRM beam.

Figure 3.11: A collection of plots demonstrating, the low aberrations present in the CRM beam.

3.4.2 493 nm Telescope

The 493 nm optical pumping telescope in this project is for the qudit, $^{137}Ba^{+}$. This will be circularly polarized and along the magnetic field direction (parallel to the quantization

axis) to drive σ^+ and σ^- transitions. The $6S_{1/2}$ level in $^{137}Ba^+$ has 8 hyperfine levels, considerably more than $^{133}Ba^+$ because of the nuclear spin $I = 3/2$.

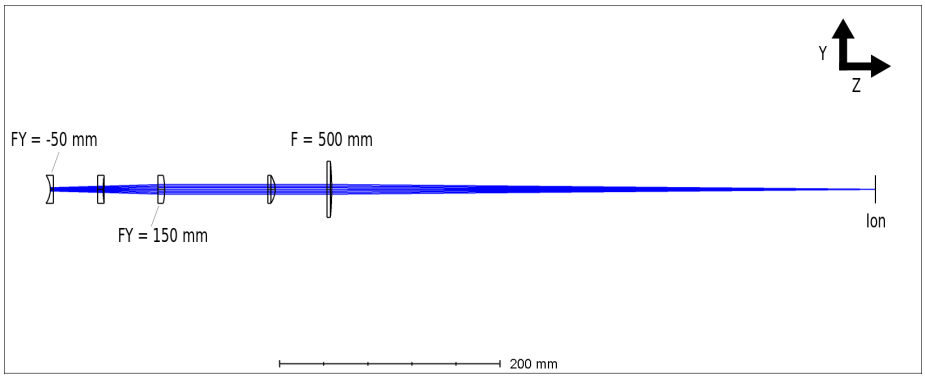

(a) Y-axis view of the telescope. FY corresponds to cylindrical lenses focusing on the y-axis. Magnification in y-axis $M_y \approx 3$.

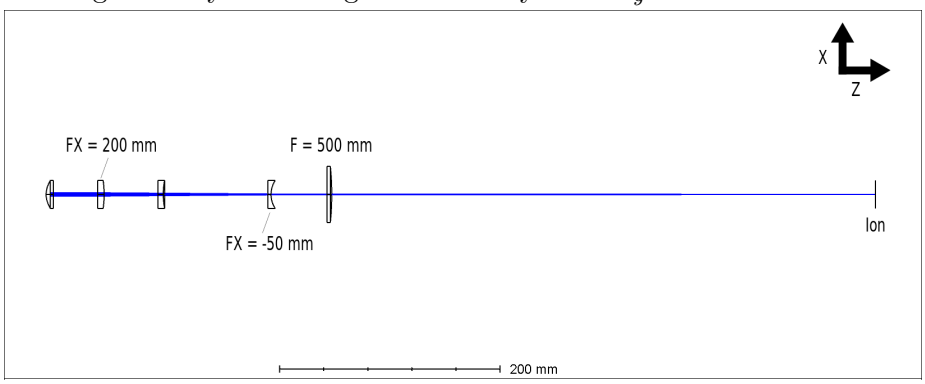

(b) X-axis view of the telescope. FX corresponds to cylindrical lenses focusing on the x-axis. Magnification in x-axis $M_x \approx 1/4$.

Figure 3.12: 493 Optical Pumping Ray Tracing.

This telescope utilizes two cylindrical lenses for each axis to re-shape and re-collimate the beam before being focused with a spherical plano-convex lens. This is similar to the achromatic telescopes in that the cylindrical lenses are interleaved to reduce footprint. The aberrations can be found in Figure 3.13 and more details are in Table C.7.

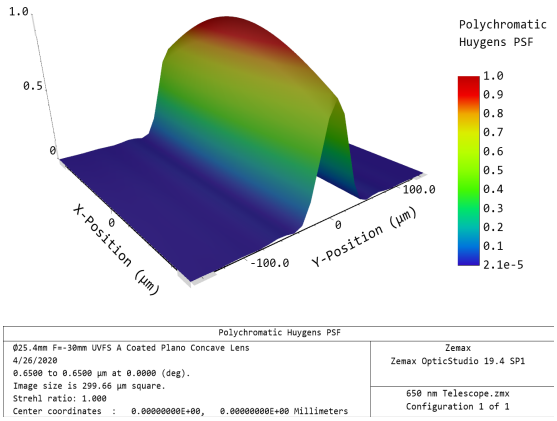

(a) An almost ideal point spread function ensuring diffraction limited performance.

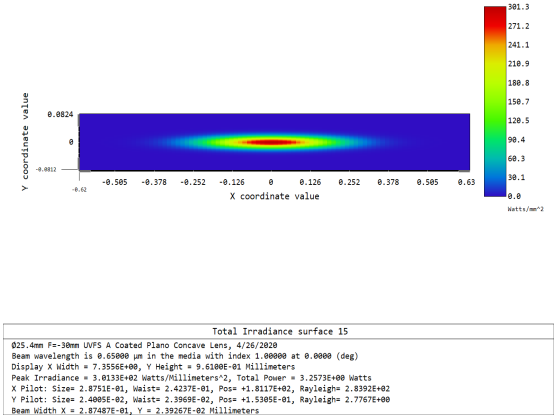

(b) Simulated physical beam, showing the beam waists, 24 μm (Y axis) and 239 μm (X axis), necessary to address a chain of ions in the Sandia HOA 2.0 trap.

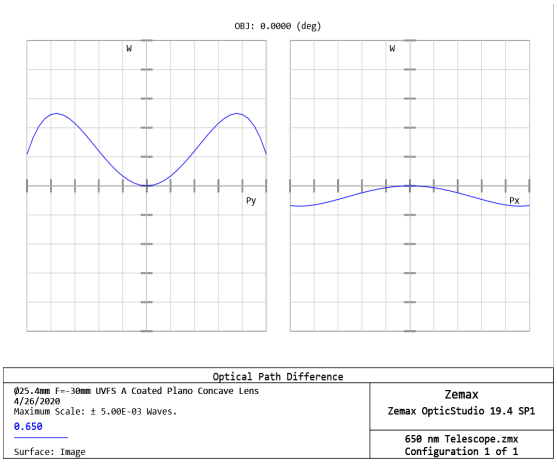

(c) Optical path difference plot, showing spherical aberrations from the cylindrical and plano-convex lenses.

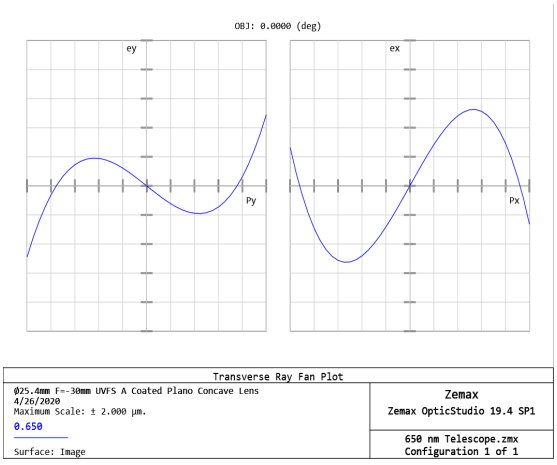

(d) Ray fan plot, showing spherical aberrations from the refractive optics used to shape and focus the beam.

Figure 3.13: 493 nm optical pumping aberrations.

3.4.3 1762 nm Telescope

The 1762 nm beam drives the $6S_{1/2} \rightarrow 5D_{5/2}$ quadrupole transition. The orientation with respect to the magnetic field allows $\Delta m = \pm 2$ quadrupole transitions. In this project, the shelving beam is necessary for both high fidelity state preparation of $^{133}Ba^{+}$ and to measure the qudit states in $^{137}Ba^{+}$.

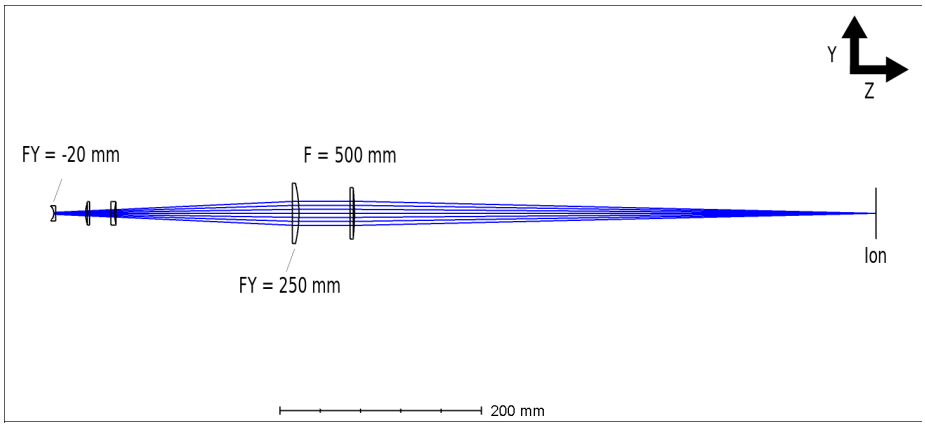

(a) Y-axis view of the telescope. FY corresponds to cylindrical lenses focusing on the y-axis. Magnification in y-axis $M_y \approx 12.5$.

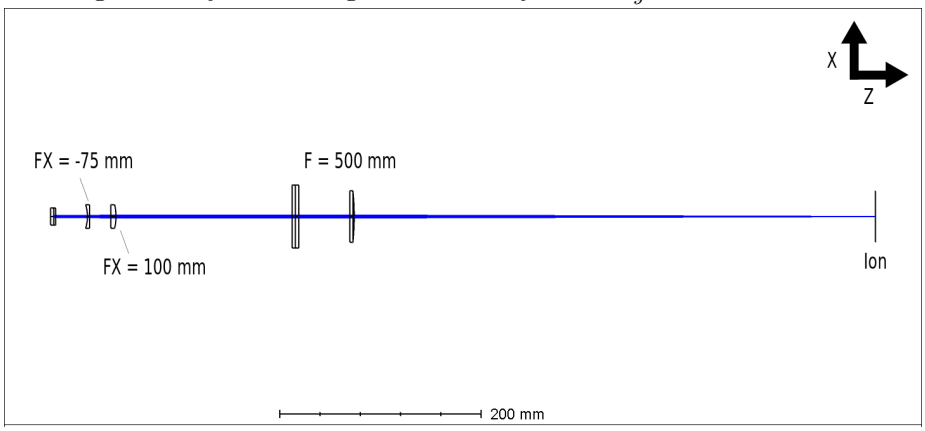

(b) X-axis view of the telescope. FX corresponds to cylindrical lenses focusing on the x-axis. Magnification in x-axis $M_x \approx 3/4$.

Figure 3.14: 1762 nm shelving ray tracing.

The shelving telescope needs to be magnified quite a bit more than the visible telescopes simply due to the wavelength. There is a slight de-magnifcation that must occur in the

x-axis to obtain a beam waist $\omega_{x0} = 243\ \mu$m at the ion. The wavefront will be consistent and relatively flat across the ion chain as shown in Figure 3.15c. The telescope is further described in the Appendix C.

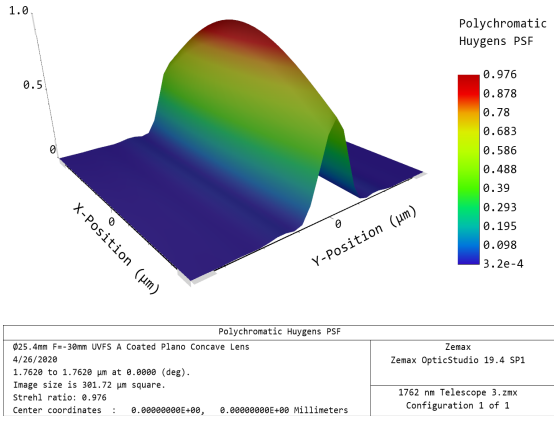

(a) Point spread function for the 1762 nm image at the ion.

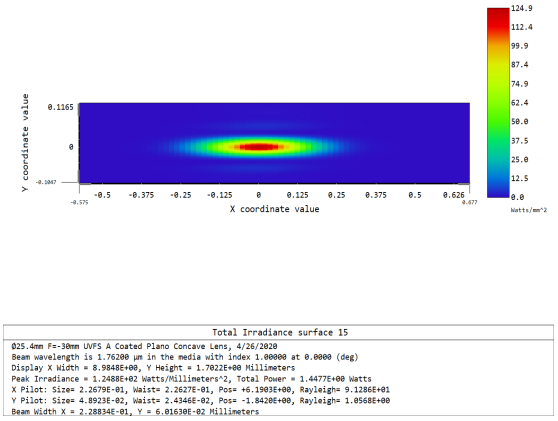

(b) Simulated physical beam at the ion, showing 22 μm (Y axis) and 243 μm (X axis) beam waists.

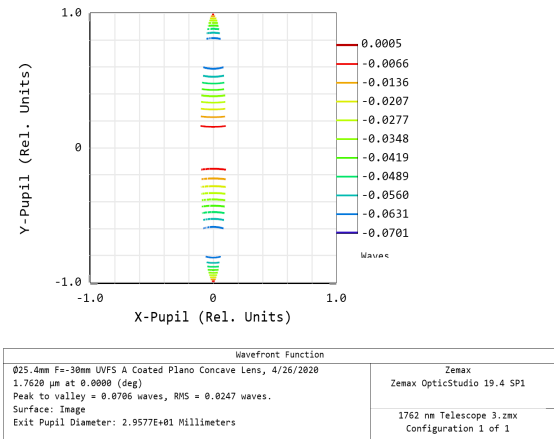

(c) Wavefront map at the ion, showing near constant phase across the ion chain.

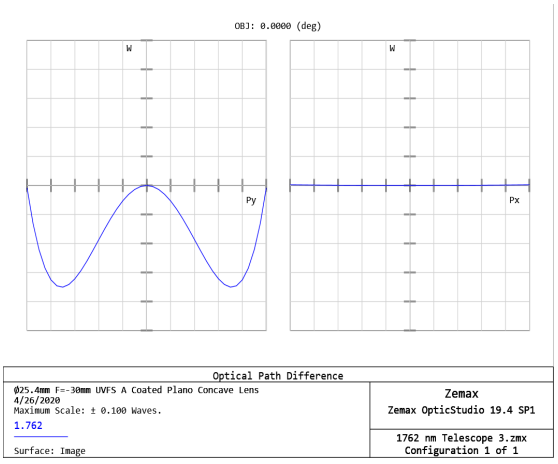

(d) Optical path difference with characteristic spherical aberrations, meeting the Rayleigh criterion.

Figure 3.15: 1762 nm shelving aberrations with constant phase and diffraction limited performance.

3.5 Other Telescopes

In this section, alternative designs for the previous telescopes are presented. The finalized designs presented earlier were chosen mostly based on space constraints, but the following designs could also be viable options. Many of the sensors utilized in the beam paths are off-the-shelf (OTS) components in order to reduce the amount of homebrew designs and increase the consistent performance of individual pieces in the system. This of course influences the optical designs, which is why the following designs were considered, but ultimately decided against.

3.5.1 Mirror Telescope

This design utilizes mirrors to do the elliptical beam shaping and focusing onto the ions. The obvious benefit from this is that there are no chromatic aberrations. There are cylindrical concave, spherical concave, and spherical convex mirrors in this design. The input is a collimated beam with a 3.42 mm diameter (493, 553, 614, 650 nm) and enters 5° to the normal of the first mirror. The first mirror is cylindrical and focuses in the x-axis only. The second mirror is a convex mirror and re-collimates the x-axis to a smaller beam waist while simultaneously expanding the y-axis. The y-axis is re-collimated by the third mirror at a larger beam waist. The beam has now been shaped and needs to be focused at the ion. The final lens is a spherical concave mirror that focuses both axes at the ion. The collimation was optimized in OpticStudio.

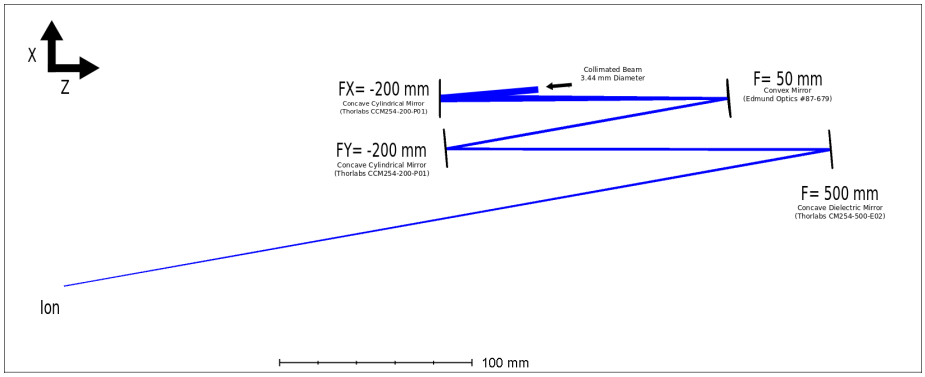

Figure 3.16: Ray tracing of a mirror telescope, completely free of chromatic aberrations.

This design provides very similar beam waists compared to the finalized designs, and with a little tweaking the optimal beam waists could be achieved. This is evident in the

physical optics simulation in Figure 3.17b, where the beam at the ion for the 493 nm portion is plotted. The PSF is very high and the OPD is very low, meeting both necessary criteria. The wavefront is also relatively flat at the ion so the phase will be consistent across the chain, this is shown in Figure 3.17d.

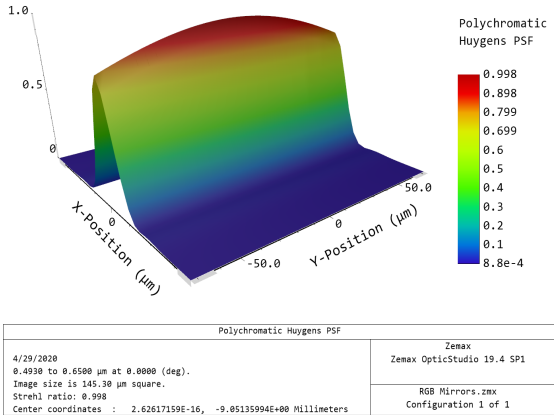

(a) Point spread function of the mirror telescope.

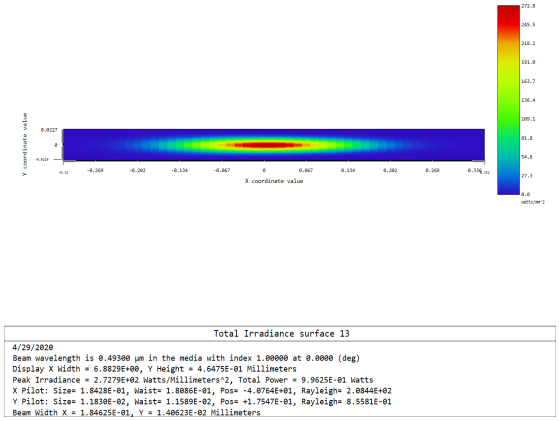

(b) 493 nm physical image simulation.

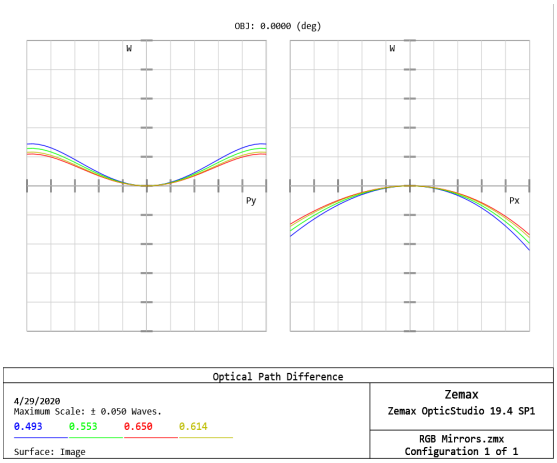

(c) Optical path difference of the image plane.

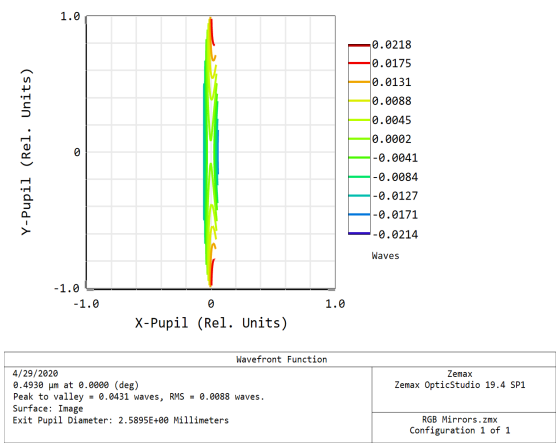

(d) Wavefront plot of the image plane.

Figure 3.17: Results for a mirror telescope to shape and focus elliptical beams.

This design was not chosen because the footprint was slightly larger and the mechanical design would be a crucial component to reducing the aberrations in the telescope, which would require more proving out. This design is viable if the chromatic aberrations are found to be a limiting factor with regard to intensity stabilization.

3.5.2 Custom Achromatic Lenses

Simple achromatic lenses can be designed by picking glasses that eliminate the effects of dispersion through the system. This is useful in optical systems where achromatic aberrations dominate. The dispersion throughout the entire optical system must be zero, which can be done by picking two glasses with Abbe numbers, V_1 and V_2, and total power Φ_{total} [87]. The total power $\Phi_{total} = 1/F$, where F is the focal length of the system.

$$\Phi_1 + \Phi_2 = \Phi_{total} \tag{3.15}$$

$$\frac{\Phi_1}{V_1} + \frac{\Phi_2}{V_2} = 0 \tag{3.16}$$

The power of the lenses, Φ_1 and Φ_2, can be solved for after the glasses of the lenses and the total power of the lenses have been picked. Equation 3.15 ensures the desired power and equation 3.16 enforces that the dispersion is 0 across the system.

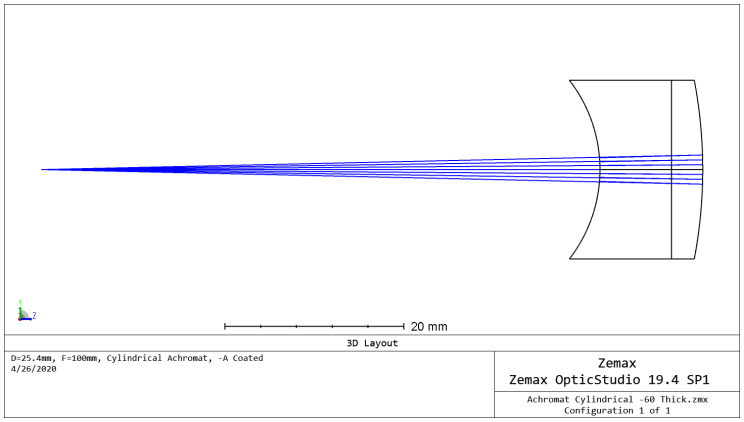

Figure 3.18: Custom achromatic doublet.

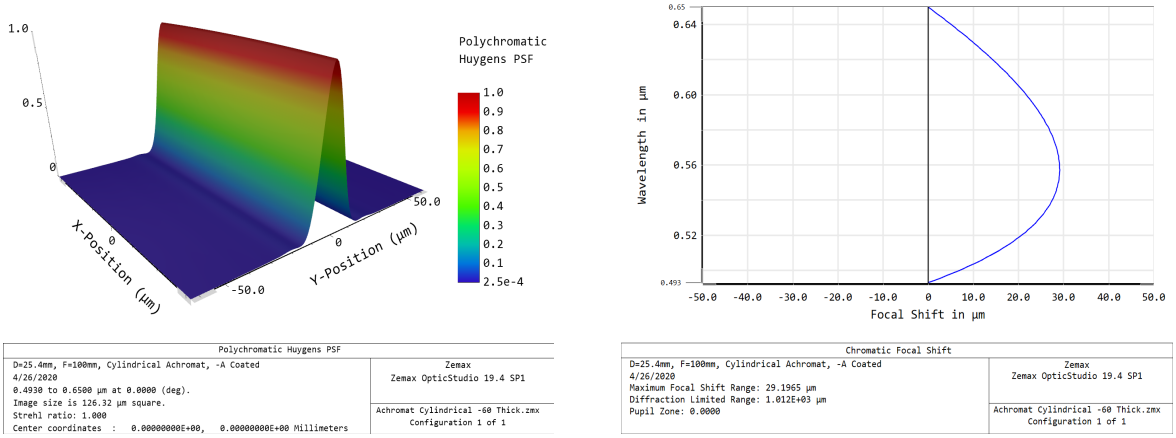

(a) Point spread function.

(b) Focal shift.

Figure 3.19: Results for a custom achromatic lens.

Using this first order equation, achromatic lenses can be designed for any given focal length. Further optimization can be done by including these doublets in larger systems and designing from there. Achromatic doublets can also be designed with singlets that have a finite radius on both sides, but this requires a more complex cementing process.

Figure 3.18 shows a ray tracing of a negative cylindrical achromatic doublet with $F = -60$ mm. This could be particularly useful in reducing the footprint of telescopes, since the vast majority of the OTS cylindrical achromatic lenses are positive.

3.5.3 Alternative 1762 nm Telescope

This alternative telescope is not considered because of its incredible length, but it does have one benefit that the final design lacks, which is that there are intermediate image and Fourier planes. These planes allow the image position or angle to be changed at the ion by utilizing a glass plate to apply the specific translation. Specifically these planes can be used to change the most sensitive axis, the y-axis, which has a beam waist that is ten-fold smaller than the x-axis. By placing glass plates at these planes and tilting them, the position and angle of the image at the ion can be changed independently, without coupling other axes, unlike a pair of piezo mirrors. This would simplify beam positioning calibration routines.

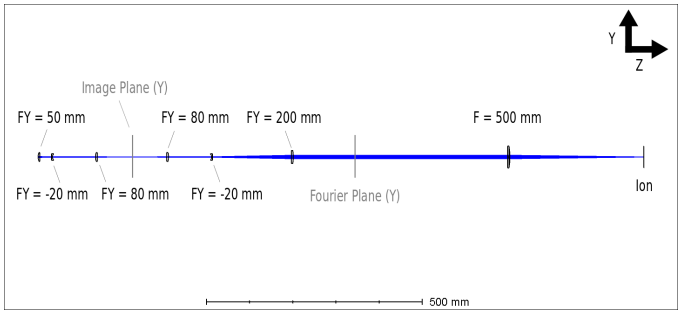

(a) Ray tracing for an alternative 1762 nm telescope.

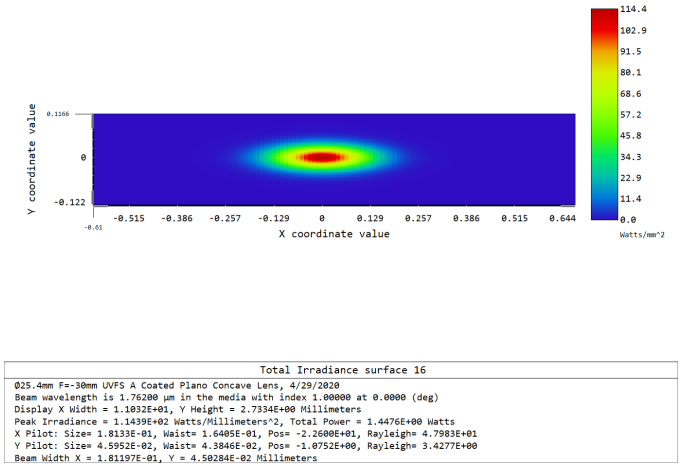

(b) Simulated physical beam of the image.

Figure 3.20: Telescope for the 1762 nm shelving beampath with intermediate planes.

The exact beam shape at the ion needs to be optimized, but this will suffice for a case example. The difficulty with including the intermediate planes stems from the fact that the image plane must be demagnified onto the ion so that it is less sensitive to vibrations and positional changes from the glass plate, which requires significantly more beam shaping, increasing the total telescope length [3].

Chapter 4

Beam Positioning

This chapter presents the optomechanical portion of the CW optics design. The main necessities for the optomechanical design is to ensure independent control of separate beam paths, full positional and angular control of the focus at the trapping sites, and appropriate power and positional sensors that can be used to develop calibration routines or correct for drifts. These drifts happen much slower than the experiment time, but over the course of a day the Rabi frequency could change significantly from these intensity fluctuations. There are other optics to control the beam power and polarization at the ion, before the beam shaping and positioning optics. The AOMs and EOMs are in optical racks, not pictured in these schematics. These schematics represent the CW optics on the optical table and near the vacuum chamber.

4.1 Optomechanical Layout

These optical designs are on the optics table, starting from a single-mode optical fiber which transfers light from the laser rack to the optics table. The black text in the following schematics indicate optical objects, or mounts. The red text indicates a control device, whether it be a photodiode, CCD, 2D position sensor, motorized rotational waveplates, linear stages, or piezo mirror mounts. The blue text is a tag that connects these optical schematics to control schematics, which are not presented here. The schematics are mostly qualitative in the sense that there are no relative sizes or distances.

In each beam path, the collimated light encounters a half-wave plate followed by a polarizing beam splitter and another half-wave plate. The wave-plates are on motorized

rotation stages so the gross power can be adjusted after the fiber collimator and linearly polarized light can be sent to the trap. There is a photodiode sandwiched between the waveplates to act as a pick off for feedback onto the motorized rotation mounts for gross power control. There are some differences in the beampaths, for example, the optical pumping 493 nm beam path has a quarter wave-plate for preparing circularly polarized light, but each beam path has a very similar set up. After the waveplates, the beam is picked off onto a CDD for mode monitoring of the fiber coupling. This is the standard beam preparation for the CW optics, which were primarily designed by Matt Day, a post-doc working on the project.

After the beam preparation, the beam goes to the telescopes for beamshaping and focusing, which is one of the primary areas of design presented in this thesis. There are apertures for gross alignment of the beam into the telescopes. The beamshaping portion of the telescopes will have fixed relative distances in order to optimize the re-collimation of the circularly collimated beam into a collimated beam that is elliptical. The final lens of the telescope is mounted on a linear piezo stage with a 12 mm travel range to adjust the focus along the optical axis and at the ion. After the beam has been reshaped and it is starting to focus, the beam encounters a pair of piezo mirror mounts which give full angular and positional control (in the XY plane, if the optical axis is taken to be in the Z direction) of the focus at the ion. The beam is picked off and focuses onto a 2D position sensor before going into the chamber. This creates an image plane identical to that at the ion. A 1:1 mapping can then be inferred between the position of the focus at the ion and what is measured on the 2D position sensor.

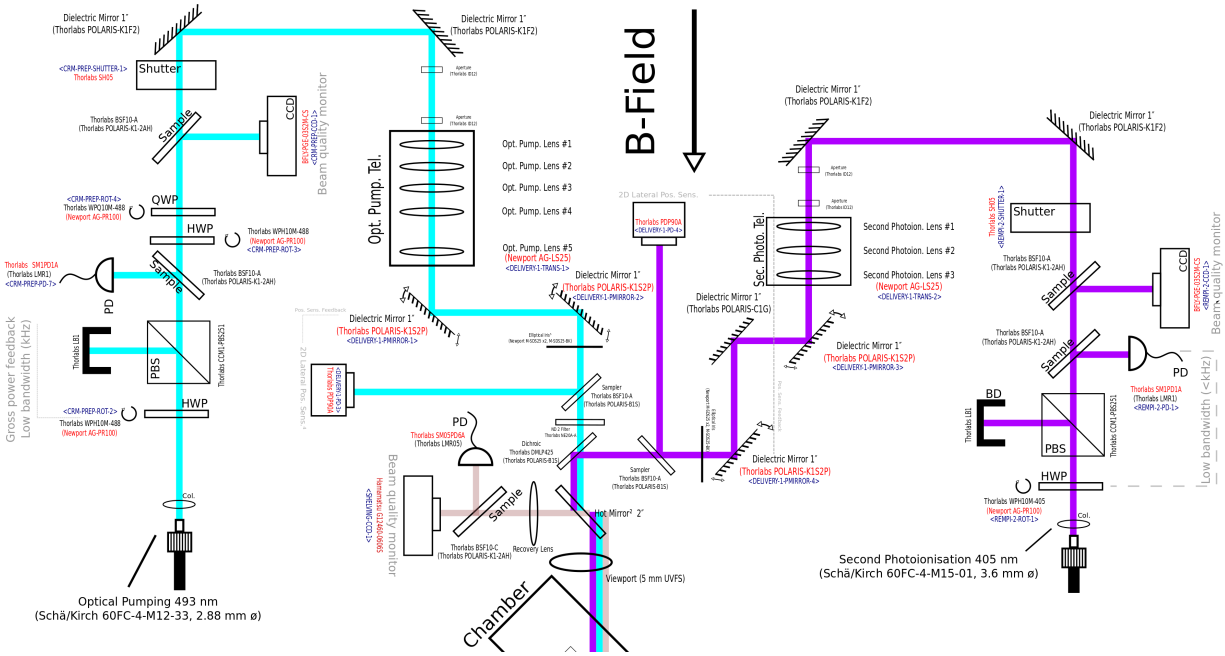

Figure 4.1: 493 nm optical pumping and 405 nm photoionization beam path.

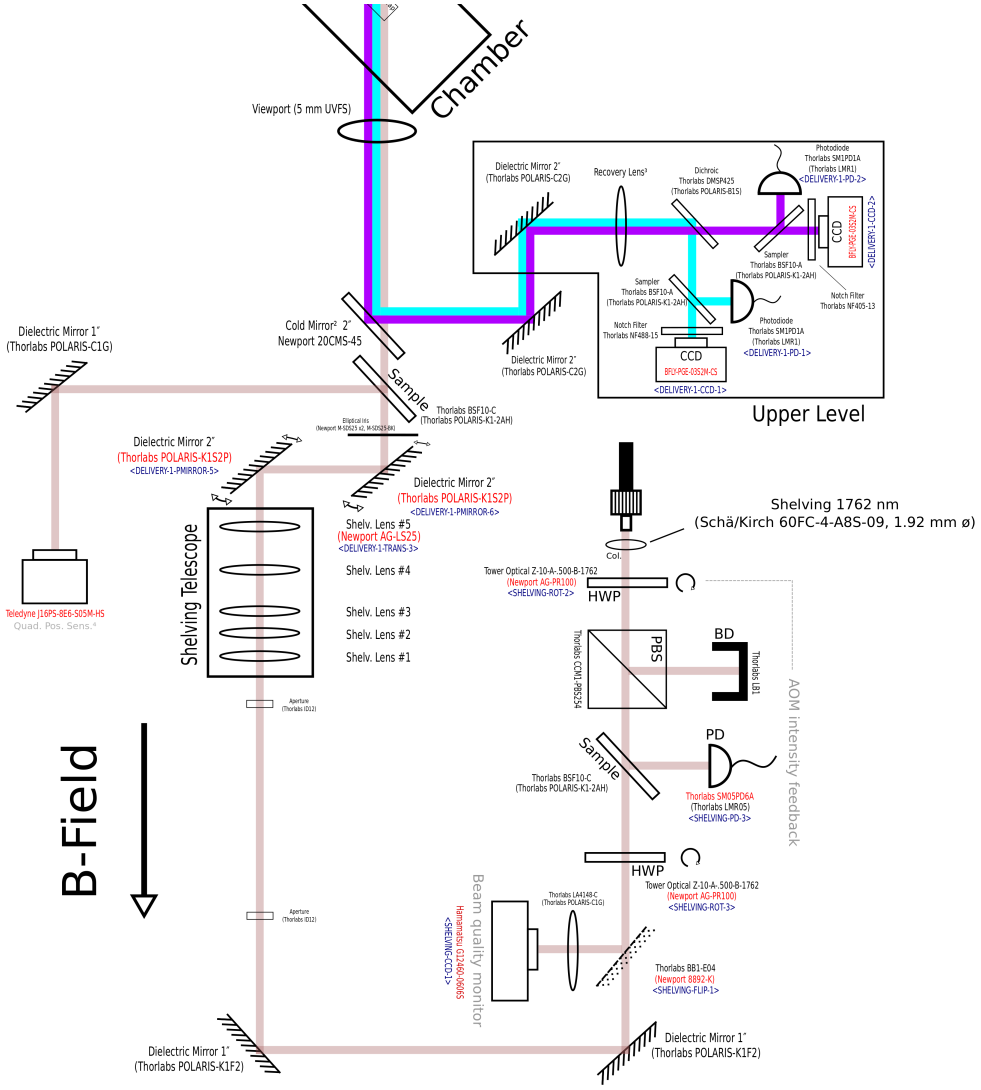

Figure 4.2: 1762 nm shelving beam path.

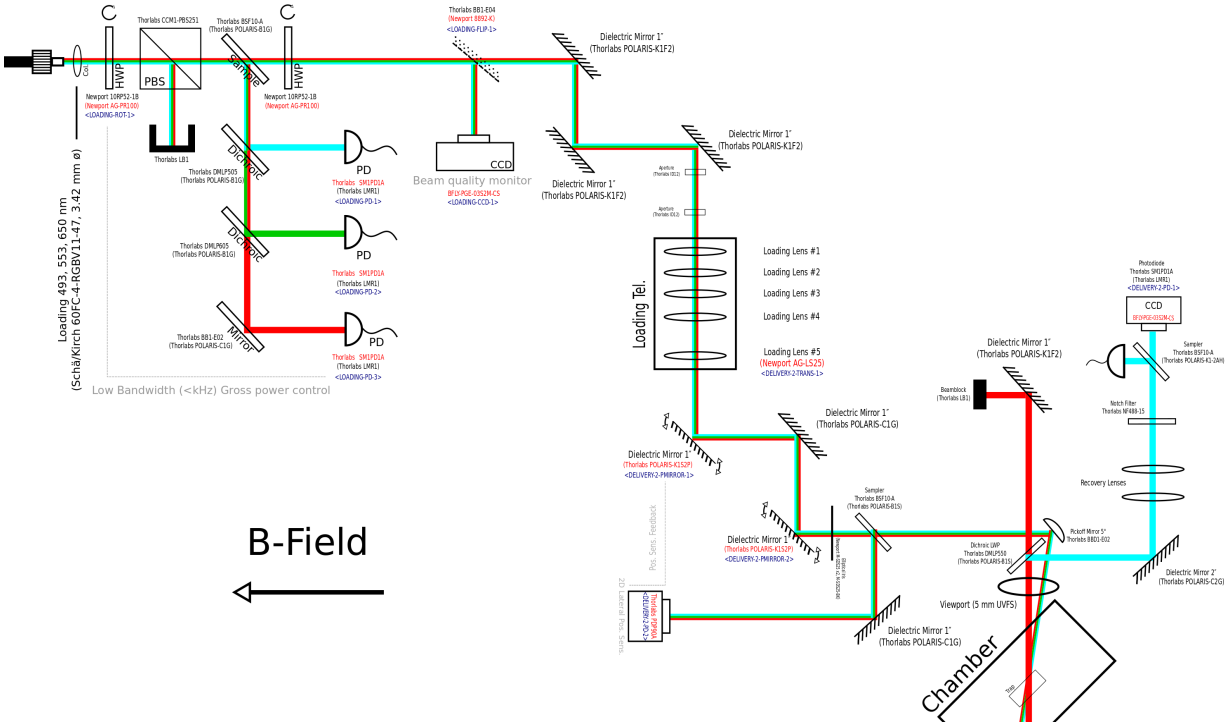

Figure 4.3: 493, 553, 650 nm Loading and 650 nm Repump beam paths.

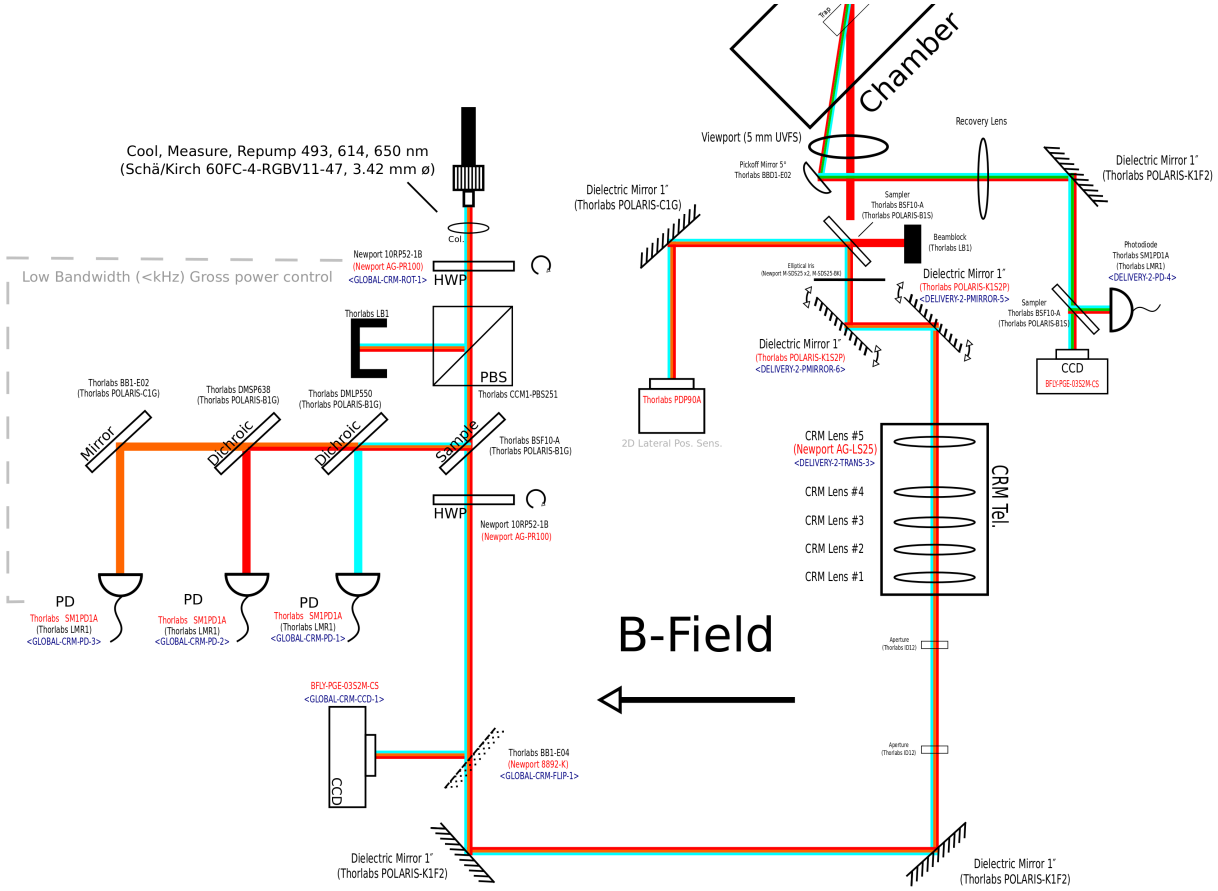

Figure 4.4: 493, 614, 650 nm Cool/Measure/Repump beam path.

4.2 Positioning Estimations

In order to ensure the integrity of the optomechanical design, the minimum step sizes and total throw of the focus at the ion must be estimated. The linear stage (Newport AG-LS25) used to position the focus along the optical axis has a minimum step size of 50 nm and a total travel range of 12 mm. The 12 mm travel range is enough range for even course alignment and the 50 nm step size, assuming perfect repeatability and closed loop, could allow re-alignment of a defocused beam such that there is $< 1 \cdot 10^{-9}$ between the original beam intensity and the re-aligned intensity at the ion (intensity is normalized).

The piezo mirror mounts (Thorlabs POLARIS-K1S2P) are placed $\approx$ 450 mm away from

the focus of the ion and they have a total angular throw of 500 μrad each. Assuming the focus is perfectly aligned to begin with, each piezo mirror mount could correct for drifts up to 225 μm. The total combined throw of the system would then be $\approx$ 450 μm. The room is stabilized to $\pm$ .2° C, but for estimation purposes, thermal fluctuations can be assumed to be $\pm$ 2° C.

$$\alpha = \frac{1}{L}\frac{\Delta L}{\Delta T} \tag{4.1}$$

The thermal expansion coefficient α for aluminum is $24 \cdot 10^{-6}$/C. If the length of a custom aluminium breadboard (used to mount an optical beam path) is one meter, then the maximum thermal drift is $\approx$ 48 μm. This overestimation in the drift shows that the placement and total throw of the piezo mirror mounts will allow for focal drifts at the ion to be corrected without the need for a person to physically enter the lab and perform course alignment procedures.

The minimum step size of the piezo mirror mount can be estimated based on the minimum voltage step size (2 mV) and assuming a linear relationship between the voltage and angular deviation. Specifications give angular deviations of 0.5 μrad for voltage steps of 0.1 volts [125], so the minimum angular deviation with 2 mV step sizes is $\approx$ 10 nrad. The piezo mirror mounts are $\approx$ 450 mm away, so the minimum step size is $\approx$ 4.5 nm at the ion. This is more than enough to stabilize the intensity. More optomechanical drawings can be found in Appendix C.1.

The optomechanical design can be further evaluated by considering fluctuations in the air temperature of $\pm$2° C and evaluating the impact that this has on the focusing lens in the CW telescopes. The focusing lens is considerably more sensitive than the collimating portion of the CW telescopes. Fluctuations in position, either induced by vibrations or thermal stress, can translate directly to the position of the focus at the ion.

This analysis was done in a solution package from the finite element modeling software, ANSYS. The transient thermal solver was applied to the lens and mount assembly and then linked to a static structural solution that gave deformations induced by the thermal gradients for each time step. Based on the magnitude of the deformations, the beam will be displaced at the ion and this deflection of the beam at the ion can be estimated for this limiting case.

A time varying convective heat load was applied to the front faces of the assembly, $2\sin(t/\pi) + 22$, where t is the time in minutes. This is meant to simulate slow thermal drifts of 2° C around the starting ambient temperature of 22° C. The thin film coefficient was taken to be 50 W/m^{2}C, simulating forced air convection [126]. This is a relatively high

thin film coefficient for air. For comparison, stagnant air can have a coefficient down to 1 W/m^2C. The high thin film coefficient allows the model to saturate quickly with heat.

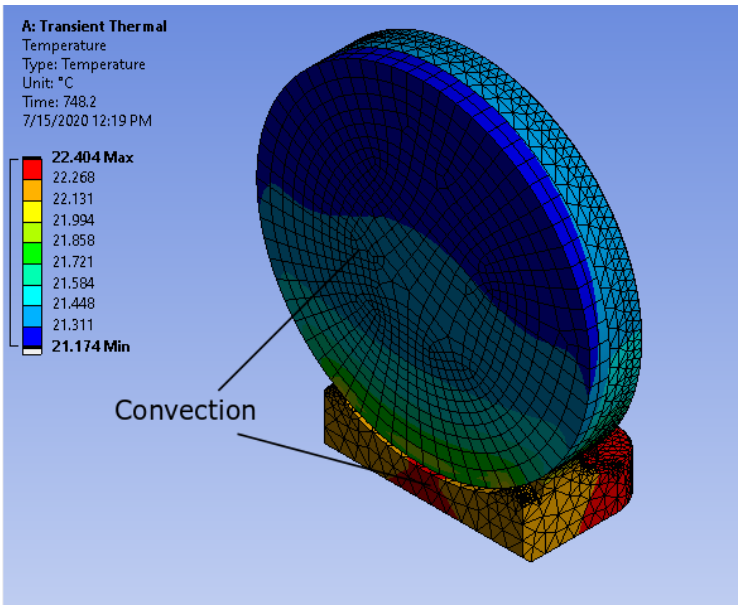

Figure 4.5: Temperature of a lens (Thorlabs LA1380-A) glued on a fixed optics mount (Thorlabs POLARIS-C2G), under a time-dependant convective heat load.

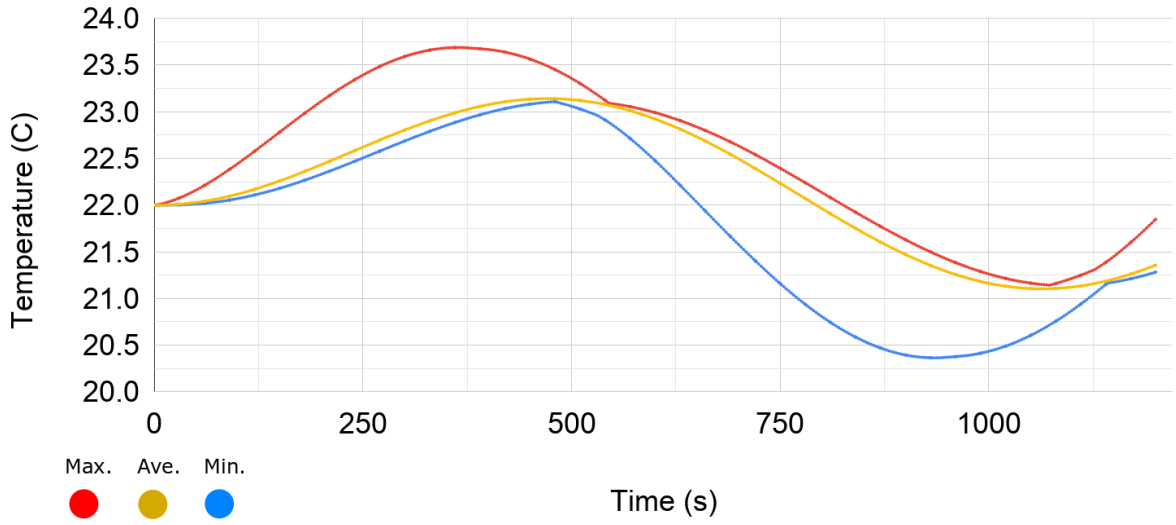

Figure 4.6: Time dependence of the temperature for the lens and mount assembly. Maximum, minimum, and average temperatures are taken from any element in the model.

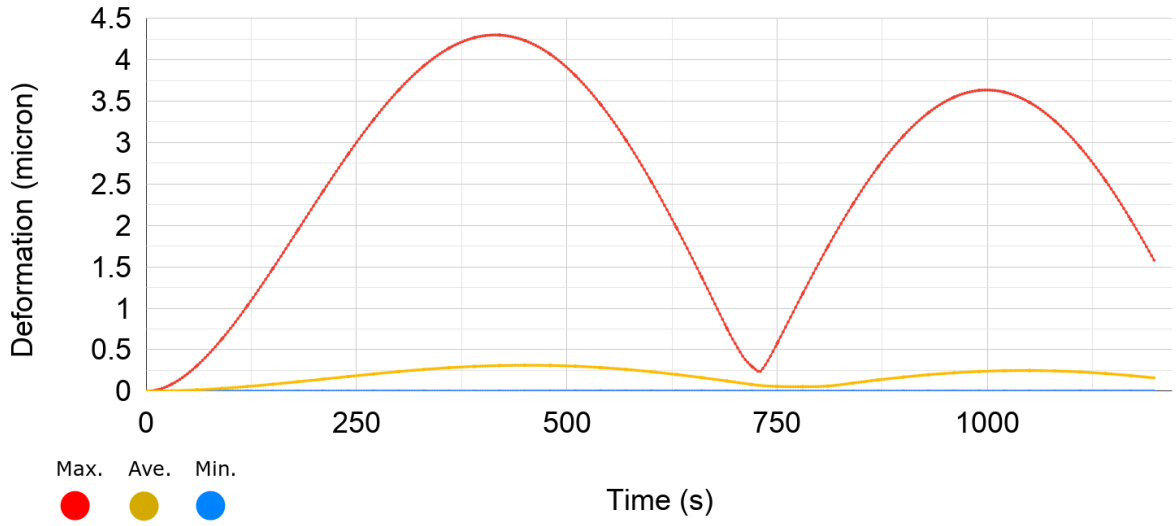

Figure 4.7: Deformation of the lens and mount assembly induced from stress caused by the thermal gradient. The maximum and minimum deformation is taken from any element in the model.

This simulation is a gross overestimation of how turbulent the conditions will be in the environmental room that encapsulates the entire experiment, but it serves to further validate the optomechanical design. If the maximum deformation from this cycle displaces the lens from a position that perfectly focuses at the ion then, based on the distance of this lens from the ion (500 mm), the focus could deviate $\approx 42.5\mu$m. This displacement can be compounded with the earlier estimation for total possible displacement due to thermal fluctuations of $\approx 90\mu$m. If the total possible throw of the piezo mirror mounts are ≈ 225 μm each, then this shows that the optomechanical is fully capable of correcting for even relatively extreme variations in temperature.

This does not take into account any stress-induced aberrations that could cause the intensity and uniformity of the beam at the ion to vary, but further analysis can be done in OpticStudio by importing the deformed STL file in non-sequential mode and optimizing to find the focus.

Chapter 5

Trapped Ions in Vacuum

In order to trap ions, or chains of ions, an ultra-high vacuum (UHV) must be constructed so that background gas collisions with the ions are rare and the probability that an energetic collision removing an ion from a trap is greatly reduced. There are two classifications of vacuum systems that can be constructed to house ion traps; room temperature and cryogenic systems. In general, the standard for trapped ion experiments is to reach 10^{-11} mbar, which can be done with either system, however, cryogenic vacuum systems have increased chain lifetime and can form longer chains [10]. It has been reported in a cryogenic surface trap that the ion chain lifetime scales as $1/N$, where N is the number of ions in the chain [88]. While this is of course highly dependant on the specific surface trap, environment, and loading procedure it still shows that it is much harder to capture longer chains. Chains have been captured with $N > 50$ in both cryogenic and room temperature surface traps [10], but individually addressing or fully connecting this many ions has not been close to demonstrated.

The vacuum system described in this thesis is a room temperature system because cryogenic systems are significantly more expensive and require a certain amount of expertise. Room temperature systems also do not suffer from mechanical vibrations like cryogenic systems [10]. Room temperature vacuum systems for trapped ion qubits cater best to the remote-entanglement (RE) architecture of scaling trapped ion qubits as compared to other architectures because the vacuum pressure requirement could be as low as to only require experimental chain lifetimes for chains of 16 or 17 ions. The RE architecture refers to modules of trapped ion chains representing a single elementary logical unit (ELU) (this could be thought of as a single logical qubit), that are entangled via photonic interconnects [89]. This architecture satisfies DiVincenzo's criteria for quantum computing and quantum communication [90], whereas other trapped ion architectures like the quantum

charge coupled device (QCCD) [91] only satisfy the quantum computing criteria. Cryogenic vacuum systems provide a path for possibly scaling longer ion chains to be used for quantum simulation or even small-scale QCCD architectures, something that would likely not be possible in room temperature systems.

There are a few major differences between the room temperature and cryogenic vacuum systems. The first obvious difference is the type of collisions that ions in a chain will undergo. In cryogenic systems the background gas makeup is, for all practical proposes, hydrogen. Hydrogen in general is the most abundant gas in UHV systems, but there are still considerable amounts of CO, CO_2, N_2, and H_2O in room temperature UHV systems whereas these can be entirely frozen out in cryogenic systems [10]. This means that ion chains in room temperature vacuum systems undergo both elastic collisions, mostly from hydrogen molecules, as well as violent, inelastic collisions due to the aforementioned heavier molecules. The collisions with heavier molecules are much more likely to initiate ion chain melting that cannot be recovered by Doppler cooling [10].

The base pressure of the vacuum system impacts the performance of a trapped ion computer in two major ways. The first major way is that it limits the chain length of the ions that can be reliably captured. As the chain length grows, it becomes increasingly difficult to capture the chain and still have enough time to run many experiments before a collision with the background gas causes the ion chain to either be re-cooled or reloaded. Assuming each ion chain is one logical qubit, the base pressure ultimately dictates how well protected a qubit can be with quantum error correction schemes, because encoding into more qubits means capturing longer chains. The other major way that the base pressure can impact the performance of a trapped ion computer is through anomalous heating. Anomalous heating refers to motional heating of the ion, which eventually accumulates in the ion heating out of the Lamb Dicke regime. Anomalous heating is caused by both voltage noise and surface contaminates moving on or near where the ions are being held, changing the local potential [101]. At higher base pressures, monolayers will also build up faster on the surface of the trap, which will increase heating rates.

Besides the aforementioned effects that the vacuum system can have on the performance of a trapped ion computer, the ion chain can also be used to infer information about the vacuum system. The ion chain itself can actually be used as a pressure gauge. Depending on the dynamics of the ion chain following a low energy or elastic collision, the pressure at the trapping site can be inferred. Using the ions to standardize the pressure can be a better way to measure pressure because often vacuum gauges are placed far from the trap. There are at least two ways to estimate the pressure using ions described in the following sections.

5.1 Collisions

A great deal of information can be inferred by monitoring the collisions that ions undergo while in the trap. Ultimately this allows a designer to optimize the system to hold chains for longer periods of time. This chapter is on ion-neutral collisions that occur between the trapped ions and background gases, but the electric field noise and ion-ion collisions are also relevant when attempting to understand how to prevent losing ions [88].

5.1.1 Elastic and Inelastic

Elastic collisions in ion traps have been measured by preparing the zig-zag configuration, rather than a linear chain, and observing the ion chain flip between two symmetric orientations of the zig-zag mode [10]. This can be used to measure the partial the pressure of hydrogen or overall background pressure near the ion trap, but depending on the electric field noise the ions can flip without a collision. This technique is based on a model that only takes into account elastic collisions.

The inelastic collisions are of more concern because they are more likely to induce ion-ion collisions in the chain that will cause catastrophic melting and loss of an entire ion chain. These can be measured by looking at the dark count rate of ions in the chain [10]. Inelastic collisions can cause the internal electronic state of the ion to change such that it gets excited to a state that then decays to a state not being pumped. In $^{133}Ba^{+}$ this would correspond to the electron getting stuck in the metastable $5D_{5/2}$ state. The typical dark count rates per ion were measured to be $2 \cdot 10^{-4}\ s^{-1}$ per ion at room temperature [10]. The dark count rates in cryogenic systems can be an order of magnitude lower than the dark count rates in room temperature systems [10].

Using the dark count rate or elastic collision model is a better way to standardize the pressure in a vacuum chamber for ion traps. Standard gauges have to be placed far from the ion trap where the pressure can vary by an order of magnitude so reporting pressures with the dark count rate or elastic collision rates can make comparisons between systems more accurate. The estimation from elastic collisions yields significantly higher vacuum pressures estimates, but this depends on the frequencies of the surface trap involved in the experiment [10].

5.2 Trap Contamination

Reducing atmospheric exposure of the chip trap is important for reducing contamination and thus achieving better heating rates. The Sandia HOA trap that will be used in this experiment comes packaged in a hermetically sealed container and should only be opened in clean room environments as large particulates can cause the closely spaced electrodes (3 μm) to short. The process of installing and baking the vacuum system will expose the trap surface to contaminants that will increase the heating rate. In a perfect world, the trap would be manufactured, cleaned, and packaged without ever being exposed to the atmosphere. This is not a perfect world and there are a couple steps that need to be taken during the vacuum assembly process like installing the chip trap and baking the vacuum chamber that can expose the trap to higher than UHV gas loads. By looking at the Hertz-Knudsen equation, an estimation of the most harmful steps in the bring-up phase can be evaluated [93].

$$\frac{dN}{dt} = \frac{AP}{\sqrt{2\pi m k_b T}} \tag{5.1}$$

This describes the rate of deposition of molecules on the surface trap based on the area $A \approx .000025$ m^2, pressure P in pascals, temperature T and mass m of the impinging molecule.

The first major step in the assembly process that will expose the surface trap to the clean room is installing the trap into a zero-insertion force (ZIF) socket. This will be done after all pumps, diagnostics, supporting frames, and internal structures have been assembled. The ZIF socket will then be placed into the experiment chamber and the final imaging viewport attached. The next major step, during which the trap will be exposed to higher gas loads, is the final baking at low temperatures (150° Celsius). These two steps will expose the surface of the trap to significantly more molecules and increase the trap heating rates.

Assuming N_2 molecules, 25° Celsius, and one atmosphere of pressure, the absorption rate is significantly higher during the installation process rather than the baking process at 450° Celsius and $1{\cdot}10^{-6}$ mbar.

$$\frac{dN_{room}}{dt} = 1.079 \cdot 10^{23}, \quad \frac{dN_{bake}}{dt} = 6.54 \cdot 10^{13} \tag{5.2}$$

Taking into account the approximate time it takes for both of these processes, we can estimate the trap will have been exposed to $N_{room} \approx 3.8844{\cdot}10^{26}$ if the installation process

takes one hour. $N_{bake} \approx 3.95 \cdot 10^{19}$ if the baking process takes a week. Again, this just describes the amount of molecules that has impinged on the surface of the trap, not how many have actually been absorbed. Finally, the impingement rate can be estimated at the estimated base pressure of $5 \cdot 10^{-12}$ mbar.

$$\frac{dN_{UHV}}{dt} = 1.40 \cdot 10^{9} s^{-1} \tag{5.3}$$

This is assuming room temperature and H_2 molecules. Clearly the most harmful step by far is the installation of the trap in the clean room, so the trap should be the very last step in the installation process. Many ion trapping groups are focused on reducing the trap contamination or cleaning the trap surface *in situ* with low energy RF plasmas [33], argon-ion beams [34] and even pulsed UV beams [35]. The pulsed UV beams are not ideal as they have been shown to cause damage to the trap electrodes, but they did reduce heating rates by an order of magnitude. The *in situ* cleaning of surface traps benefits room temperature traps significantly more than cryogenic traps.

Even at UHV, significant monolayers will build up on the trap surface over time, but the monolayer deposition rate depends significantly on how often the trap is loaded as well as the final base pressure. In this project *in situ* cleaning was not considered because the experimental chamber lacked room for the RF coil that generates the cleaning plasma and also the ability to create a flow of argon, but it is something that would significantly benefit room temperature surface traps.

Chapter 6

Vacuum Fundamentals

In order to design and construct an UHV system, it is important to have a base layer of terminology and knowledge that will aid a person in their process. This chapter is focused on providing basic information related to working with ultra-high vacuum (UHV) systems. This is intended for someone that has never worked with UHV systems and will be a good starting point before embarking on any projects involving vacuum systems.

Range	Pressures (mbar)
Low Vacuum	1 - 10^{-3}
Medium Vacuum	10^{-3} - 10^{-5}
High Vacuum (HV)	10^{-5} - 10^{-9}
Ultra-high Vacuum (UHV)	10^{-9} - 10^{-12}
Extreme-high Vacuum (XHV)	$< 10^{-12}$

Table 6.1: Different pressure ranges. Ion traps require at least UHV.

6.1 Sealing

There are three standard ways that seals can be created to ensure vacuum. These seals are to be used for different systems, depending on the design of the system and what base pressure it can reach. The seal is made between two flanges on different pieces of the vacuum chamber.

The first seal is a Klein-Flansche (KF) flange for room temperature systems, rated to high vacuum. This consists of a fluorocarbon ring around a smaller, aluminum ring

used primarily when pumping at pressures higher than UHV because they can be quickly detached. Often they are referred to as an O-ring and used in conjunction with flexible bellows, but they are not suitable for ultra-high vacuum. These can be moderately baked, but a residual gas analyzer (RGA) can often pick up trace amounts of fluorocarbons so ideally this will not be used during baking in systems going to UHV. This seal is made by clamping an O-ring between two opposing KF flanges.

The second seal to consider when working with vacuum systems is the con-flat (CF) flange which makes a metal to metal seal between the "knife-edge" on the CF flange and a metal gasket. The metal gasket has to be softer than the metal of the knife-edge. Typically the CF flanges are made from stainless steel and the gaskets are copper. This is rated for UHV and even pressures $< 1 \cdot 10^{-13}$ (XHV) [40]. This is the type of flange used on every port of the vacuum system in this project.

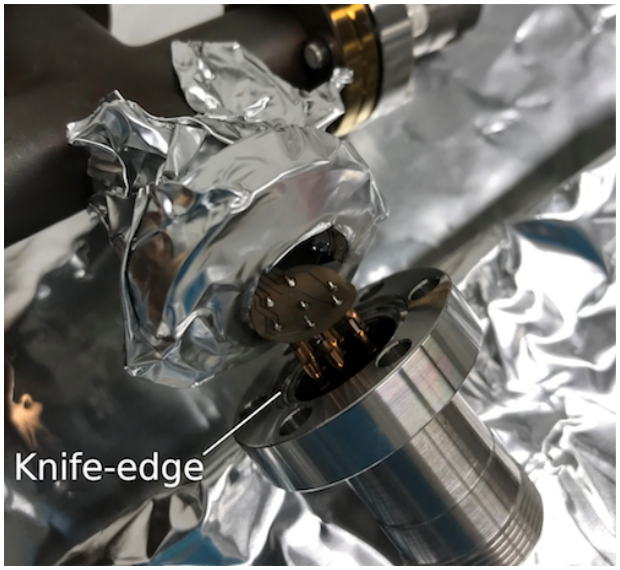

Figure 6.1: Example of a CF flange on a previous project.

The knife-edge is not actually sharp, but it is important not to damage the knife-edge because it could compromise the seal or cause the entire flange to be replaced. Depending on the specific situation different metal gaskets can be used. During baking processes gold plated copper gaskets are better to use because bare copper can oxidize at high temperatures, causing it to stick to the flange itself. Annealed copper gaskets can be used for fragile connections that can only handle so much torque like with viewports. Annealing the copper makes it softer so less torque needs to be applied to make the seal. CF flanges

and copper gaskets can be used for long, high temperature bake outs up to 450° Celsius, but it is not recommended to go above this for prolonged periods because then the copper gasket can become annealed and leaks can develop [40]. CF flanges can be used during "vacuum firing", which is when the system is brought up to 800°-900° Celsius for a couple of hours under vacuum [16]. This is a relatively short time compared to typical bakes which last about a week.

Flange O.D.	Flange I.D.
1 1/3 in	16 mm
2 3/4 in	40 mm
4 1/2 in	63 mm
6 in	100 mm
8 in	160 mm

Table 6.2: Conversion table between flange diameters [40].

Table 6.2 can be used as a reference for converting between the two commonly used diameters in order to identify different CF flange sizes.

The final seal, which is commonly seen in vacuum systems, is the indium seal. This can be used for both room temperature or cryogenic vacuum systems. Indium will bond with other metals or even glasses if the oxide layer is properly stripped and enough pressure is applied. Indium sealing is used in packaging ion traps as one of the steps in a multi-stage vacuum system like the machine at ColdQuanta. This reduces the footprint of the entire vacuum system to a product that can fit in the palm of a hand.

6.2 Pumping

There are many ways to pump out a vacuum system, but the process and techniques involved are highly dependant on the current vacuum pressure. This chapter covers fundamental assumptions made when calculating base pressures of different vacuum systems and how to accurately make these calculations to obtain an upper limit on the base pressure.

6.2.1 Molecular Flow

The pressure of the gas at UHV is incredibly low and for all practical purposes the gas at UHV is an ideal gas. The gas can be described by the pressure P, volume V, number of molecules N, and temperature T.

$$PV = Nk_bT \tag{6.1}$$

If the mean free path of a molecule $\lambda \gg D$, where D is the diameter of the tube, the molecule is in the molecular flow regime and does not often collide with another molecule. Based on a molecular density at $1 \cdot 10^{-9}$ mbar of $4 \cdot 10^4$ molecules/liter [121], the mean free path $\lambda \approx 5000$ km for H_2. The diameter of the tubes in the system are 150 mm, so the Knudsen number $Kn = \lambda/D \approx 20.8$ [94]. A system with a $Kn > 10$ is considered to be in the molecular flow regime.

6.2.2 Conductance

Conductance is simply the volume flowing past a cross section during some given time period. This must be calculated in order to find the effective pumping speed. In a vacuum system this would correspond to the volume of gas flowing past a point in a tube of diameter D towards a pump. The conductance between two regions can be calculated by adding the conductance of each portion of the chamber in series [121].

$$\frac{1}{C_{tot}} = \frac{1}{C_1} + \frac{1}{C_2} + \frac{1}{C_3} \ldots \tag{6.2}$$

In any vacuum system, conductance to the pumps must be maximized in order to decrease the base pressure. Most of the time, the conductance is the limiting factor on the base pressure. There are many rough estimations when it comes to calculating the conductance of different apertures, conical reducers, bends, etc... For basic estimations it does not matter so much which exact approximation is used, but that each major element is accounted for when calculating the base pressure. There are many different approximations in various handbooks [118][119][120]. The conductance (liters/second) for a tube of diameter D and length L in cm is given below and valid when L $> 5D$ [121].

$$C = 12.1\frac{D^3}{L} \tag{6.3}$$

There can be approximations made to the diameter and length to create more accurate models for the cases of a conical reducer and bend.

Type	Approximation
Bend	$L_{eff} = L_{tot} + (4/3)(\theta/180°)D_{eff}$ [120]
Conical Reducer	$D_{eff} = (2D_1^2 D_2^2/(D_1 + D_2))^{1/3}$ [118]

Table 6.3: Different approximations used for calculating conductance.

The bend approximation refers to simply when a tube is not entirely straight, which is most often used when there is 90° angle in the path to the pump. Conical reducers have a varying diameter so the conductance will be highest at the larger diameter of the tube. Using these approximations in conjunction with the quoted pumping speed of the pumps, an estimated base pressure can be calculated.

6.2.3 Effective Pumping Speed

The effective pumping speed (EPS) is a quantity that takes into account the conductance as well as the quoted pumping speed of the pumping device. The pumping speed at the experiment chamber should always be conductance limited otherwise the pumps are not properly sized for the system. When designing a vacuum system start with maximizing the conductance to the pumps and then estimate the gas load in order to estimate the base pressure.

The quoted pumping speed of any given pump is the pumping speed directly at the start of the mounting flange. This pumping speed may also be quoted at higher pressures than UHV, so it is important to keep in mind at which pressure the pump was tested. Unless the experiment chamber is millimeters from the pump, the conductance will limit the pump to some EPS. The EPS is given below [119].

$$\frac{1}{E_{eff}} = \frac{1}{P_{sp}} + \frac{1}{C_{tot}} \tag{6.4}$$

The effective pumping speed E_{eff} depends on both the pumping speed P_{sp} and the total conductance C_{tot}. Finding the total EPS at a given port reduces to simply adding the effective pumping speed of all the pumps.

$$E_{tot} = E_{eff1} + E_{eff2} + E_{eff3} \ldots \tag{6.5}$$

By setting equal the estimated gas load at the experiment chamber to the effective pumping speed one can find the estimated base pressure. These basic equations give a

good starting point for a designing a system, but often it is easier and more accurate to use a Monte-Carlo package like MolFlow+ to simulate base pressures. These simulations are presented in the following chapter.

6.3 Gas Sources

There are many gas sources in a vacuum system, and this is usually the most difficult portion of calculating the base pressure. The gas load can vary wildly depending on the type of materials used, the heat treatment of the installed materials, the leak rates of feedthroughs or viewports, and the surface treatments of the internal chamber body. Often there is limited outgassing data on exotic materials like plastics, which hinders ones ability to accurately estimate the gas load. This can be solved by building an outgassing measurement chamber which relies on standard techniques used by groups like the American Vacuum Society [95]. Regardless of the availability of accurate outgassing measurement rates, this chapter outlines the basic gas sources that occur in all vacuum systems.

6.3.1 Desorption

Desorption is by far the largest contributor to the total gas load at the experimental chamber. Both the surface area and the mass of the materials installed in the vacuum chamber impact the outgassing rate. The heat treatment of the material can be described as a function of a diffusion constant $D(t)$, baking time t, and thickness d [14].

$$F_0 = 4D(t)\frac{t}{d^2} \tag{6.6}$$

Generally the higher F_0 indicates a lower outgassing rate, but if different materials are being compared this may not hold true.

$$D(t) = D_0 e^{E_0/RT} \tag{6.7}$$

Equation 6.3.1 describes the diffusion rate as a function of a constant D_0 (describing how well permeation takes place at the surface), temperature T, the ideal gas constant R, and minimum activation constant E_0 [14]. It is evident from this equation why higher temperature bake outs are better and why even only a few hours at 900° Celsius can have as much of an impact on the outgassing rate as a longer bake at lower temperatures.

6.3.2 Leaks

In addition to the desorption contributing to the total gas load, leaks can also contribute significantly. Any major leaks will prevent the system from obtaining UHV, but smaller virtual leaks or high leak rates on specific custom items can also limit the vacuum. Unfortunately the leak rates of items like custom viewports and feedthroughs vary each time they are manufactured, but they are usually specified to guarantee a maximum leak rate. The leak rates for the viewports on this project is $< 1 \cdot 10^{-9}$ mbar ls^{-1} for helium. The leak rate for the feedthrough was tested to $< 2 \cdot 10^{-10}$ mbar ls^{-1}. The leak rates for the CF flanges are $< 1 \cdot 10^{-11}$ mbar ls^{-1} [99]. It is important to consider these leak rates in base pressure calculations as there are a total of 10 flange and viewport connections on the experiment chamber that contribute to the total gas load.

6.4 Vacuum Technologies

This chapter gives a brief introduction to the different pump technologies and gauges used in many systems as well as the technologies used on this project. In general, many of these technologies were developed, or at least honed at CERN, so thanks be to large scientific collaborations.

6.4.1 Pump Types

There are many pumps that are used to reach UHV, many of which only work at specific pressure ranges. This is described in Table 6.4.

Pump Type	Pressure Range (mbar)
Roughing	1000 - 10^{-4}
Turbomolecular	$10^{-4} - 10^{-10}$
Ion getter	$< 10^{-6}$
Non-evaporable getter (NEG)	$< 10^{-6}$
Titanium sublimation pump (TSP)	$< 10^{-6}$

Table 6.4: Operational pressures for a variety of pumps [41].

While the ion getter, NEG, and TSP will all work at the specified levels or even higher pressures, these should not be utilized until the lowest base pressure has been reached

with the turbomolecular pump. Using this pumps at higher pressures will significantly reduce their lifetime. At UHV the ion getter, NEG, and TSP can last for years while still maintaining UHV.

A roughing pump refers to the first pump used to create an initial vacuum so that the turbomolecular pump can begin to operate. Often the roughing pump comes with a turbomolecular pump as a complete "station", however it is preferably to use roughing pumps that are dry. Any lubricant that makes its way into an ion trapping chamber would be a horrendous disaster. The turbomolecular removes gas kinetically by alternating fixed and rotating sets of blades that push molecules toward the roughing pump. There are stationary blade that are angled to prevent back draft, while the rotating blades are angled to push gas into the stationary blades. When the turbomolecular pump is operating at HV, the blades are rotating at 1000 Hz or more, so serious leaks that develop in this stage can be quite dangerous. Most stations ramp up the turbomolecular pump slowly in case there is a high gas load.

An ion getter pump works by trapping free electrons in a cyclotron motion inside of a, typically, cylindrical anode that ionize neutral background gases. The ionized neutrals are then accelerated toward titanium or tantalum cathodes. When the ionized molecule collides with the cathode it typically bonds to create something like titanium oxide or diffuses into the bulk of the cathode [41]. Energetic molecules will cause the cathode material to sputter onto the surface of the anode. Generally the ion pump current is proportional to the base pressure, so this can also be used to estimate the pressure of the vacuum system. There are different ion pumps, some of which are designed for different gas loads like the noble diode and starcell pump [41]. The noble diode is more efficient at pumping noble gases, but has a reduced pumping speed for getterable gases. Getterable gases are molecules that are more reactive like H_2, N_2, CO_2, CO, and O_2. Non-getterable gases are noble gases and hydrocarbons. The starcell pump has a different anode which increases the ionization rate of noble gases [4]. Both the noble diode and starcell have considerably lower pumping rates for most getterable gases at UHV. The starcell ion pump has about 1/2 the pumping speed as the standard diode at UHV for N_2, but the pumping speed of H_2 is comparable to that of the standard diode at UHV [4]. This project uses a starcell ion pump because it has higher pumping speeds for CH_4 [1], while still maintaining high pumping speeds for the most abundant gas at UHV, H_2.

Non-evaporable getters (NEG) refer to a class of getters that are a TiVAl alloy. Molecules bond to the surface of the NEGs by chemisorption or physisorption. NEGs in particular are incredibly porous so the surface area is relatively large, allowing them to capture more molecules [5]. When the surface of an NEG becomes saturated with chemisorbed or physisorbed molecules, the getter can be heated to a high temperature with a high current,

driving the surface adsorbates into the bulk of the material, creating a fresh coat for getting [6]. These are "non-evaporable" as compared to a TSP because a TSP must evaporate a fresh coat of titanium onto the surrounding chamber walls to continue pumping when the current coat becomes saturated. Bulk NEGs can be reactivated many times, but it is still best not to expose them to atmosphere if it can be avoided [7]. There are many different NEG alloys, but there are two broad categories, cold compressed and sintered. The sintered NEGs undergo a process by which particulates are heated and eventually bond together without liquefying. These are not prone to particulating. Sintered NEGs are used in this project because they can be placed close to the trap. These are the main hydrogen sinks for the vacuum system in this project. Cold compressed NEGs are not used because they can particulate, but they are cheaper. NEGs have been used to obtain XHV even at room temperature [8].

The TSP is similar to the ion pump in that it uses titanium to react with gas molecules and capture them on the surface. Typically these are three-filament sources that are run at a high current, sublimating the titanium and coating nearby vacuum chamber walls. Titanium is significantly more reactive at lower temperatures so often a cryoshield is used in vacuum. This is a metal shield, in-vacuum, which allows liquid nitrogen to be run internally, cooling the surfaces that the titanium will coat to < 100 kelvin [42].

6.4.2 Gauge Types

Same as with the pumps, different gauges must be used at different pressures, these are outlined in Table 6.5.

Gauge Type	Pressure Range (mbar)
Pirani	1000 - 10^{-4}
Spinning Rotor	$10^{-1} - 10^{-5}$
Hot/Cold Cathode	$< 10^{-4}$
Extractor	$< 10^{-4}$

Table 6.5: Operational pressures for a variety of gauges [39].

There are many more gauge types for vacuum systems, but these are relevant to this project. There are two gauges on the vacuum system, one is a "full range" gauge, which has both a pirani and cold cathode gauge. The pirani gauge works for higher pressure by relating the heat loss on a probe wire that is in vacuum to the pressure. The cold cathode gauge works in a similar manner to the ion pump, by utilizing a cathode and anode to

accelerate electrons, which then ionizes gas. The ionized gas is then collected on a filament and the current is used to determine the pressure [39]. There is a slight magnetic field associated with the cold cathode gauge resulting from permanent magnets used to create the cyclotron motion of the electrons. The cold cathode gauge is less accurate than hot cathode gauges (HCG) by about a factor of two, but it does not heat the chamber walls and create a local pressure rise. In fact the cold cathode gauge starts to act as a pump overtime [38].

The spinning rotor gauge is mainly used for outgassing measurement experiments or when higher accuracy is needed. The accuracy of these gauges is about 1% as compared to a hot cathode gauge with an accuracy of 15%. This gauge relates the viscous drag of a spinning metal ball to the background pressure. The spinning rotor gauge is quite expensive and not used in this project.

The final gauge is the extractor gauge which is similar to the HCG in that it uses an anode grid and cathode plate to accelerate electrons and ionize neutrals. The main difference is the placement of the collector filament. In the HCG, the collector filament is placed centrally, inside the anode grid. This makes the filament susceptible to errors, like collection of electrons from the cathode. In the extractor gauge design, the filament is smaller and placed inside a cavity under the anode grid [44]. The ionized neutrals are accelerated into the cavity, which also works as a reflector, and collected by the filament [44]. This can measure down to the x-ray limit. This gauge is used in this project because the cold cathode gauge will be highly inaccurate at the base pressure.

6.4.3 Chamber Materials & Surfaces

The exact materials and surface treatments used in conjunction with heat treatments are important variables that need to be addressed when designing a vacuum system. The standard material used to manufacture the flanges and tubes for UHV vacuum systems is stainless steel because of its low outgassing rate after baking. This is a product of industry in that stainless steel has been manufactured for many years and suppliers can easily work with it. More specifically austenitic stainless steel is used in UHV manufacturing, which is an essentially non-magnetic material. The most common austenitic stainless steel used is 304, 316, and 316LN. There is also 316LN-ESR, which is even more refined than 316LN, sporting an even lower magnetic permeability and outgassing rate [37]. ESR stands for electroslag remelt and it is a refinement process for alloys.

Besides steel, other materials are less commonly used in UHV systems because they are less available and more expensive, but some sport significantly lower outgassing rates than

stainless steel. Specifically, titanium has been shown to have outgassing rates two orders of magnitude lower than stainless steel [12]. Titanium is used in this project for the majority of the vacuum chamber because it is significantly lighter than stainless steel and it has a lower outgassing rate. Aluminum also has better outgassing rates than stainless steel, but even less manufacturers work with this than titanium [17]. Finally there has been at least one instance of groups looking at beryliuum copper, but this has not yet been used to manufacturer UHV systems [13]. Among titanium and aluminum there are different alloys that will influence performance at UHV, but the heat and surface treatments of the material can be just as relevant.

Another other major variable regarding the total gas load from the vacuum chamber is the application or absence of thin films and surface treatments. Typically UHV chambers are prebaked in vacuum for about a week and then baked in atmosphere for a day to create an oxide layer, which acts as a barrier to hydrogen desorbing from the walls. This is standard, and doing the final atmosphere bake with pure oxygen can create a thick oxide layer on the interior of the walls, but there are even better surface treatments that can act as a barrier to desorption. For example, coating a stainless steel chamber with amorphous silicon can reduce the outgassing rate by an order of magnitude or coating the chamber with a TiN film can reduce the outgassing rate by four orders of magnitude [116]. Coating with amorphous silicon can be incredibly cheap with manufacturers like Silcotek able to coat pieces for a few hundred dollars. Coating with TiN is more experimental and it is unclear if manufacturers offer this.

NEG thin films are also commonly sputtered onto the walls of vacuum chambers, turning the vacuum chamber walls from a gas load to a pump. The films have similar properties when compared to bulk NEGs described in Section 6.4.1, but the pumping speed becomes significantly reduced when it is exposed to atmosphere because there is simply less material and it becomes saturated more easily. The pumping speed will drop like $1/N$ where N is the number of exposures to atmosphere. The ideal films are only a couple of microns thick because thicker films will begin to peel [115]. Reported pumping speeds of these thin films are about 0.35 $ls^{-1}cm^{-2}$ [114]. Pressures in the 10^{-13} mbar range have been reached in large vacuum systems with inner diameters of 100 mm [117]. This was not used in this project because the coatings are prone to producing particulates even with thinner films and it is difficult to coat complex geometries evenly because of varying diameters [124].

It is hard to directly compare all of these films and surface treatments because most experiments will only study one or two of these at a time. This means that different heat treatments are used in the different experiments and that directly impacts the final reported outgassing rates. That being said, NEG films are the best surface treatment because it turns the outgassing source to a pump. The oxide films only act as a barrier to

the outgassing, it is just passivation of the surface.

Similarly it is difficult to compare all the outgassing rates of the materials directly to each other because all of the different heat treatments in each study. Stainless steel can obtain outgassing rates close to titanium alloys if they are vacuum fired, but the rates are still at least 1/2 an order of magnitude higher than titanium alloys baked at significantly lower temperatures. Titanium alloy chambers are rarely prebaked at high temperatures or vacuum fired because the outgassing rates are already extremely low and higher temperatures will destroy the oxide layer. A simple bake at 150° Celsius for 24 hours will yield outgassing rates lower than any treatment of stainless steel [12].

The main portion of the vacuum chamber in this project is made of Kobe Steel KS100. This is an annealed titanium alloy and will have a thick oxide layer ≈ 10 nm. With proper baking this could yield an outgassing rate of $7{\cdot}10^{-16}$ mbar $ls^{-1}cm^{-2}$ [12].

Chapter 7

Vacuum Chamber Design

The vacuum chamber presented in this thesis was designed around all of the necessary beam paths that are used to initialize, measure, and cool ions as well as implement high fidelity gates. Specifically, the chamber is designed around the Raman numerical aperture (NA), with a higher NA allowing individual addressing beams to more tightly focused along the ion chain such that there is less crosstalk at neighboring ions. The NA is defined by the index of refraction n and the angle that the marginal ray makes with the optical axis θ, such that the NA $= n \sin\theta$. The NA limits the two qubit gate fidelities when using Raman transitions to do individual addressing and this consideration was the first constraint set in the vacuum chamber design. For the experimental chamber (where the ion trap is housed), an off-the-shelf (OTS) vacuum chamber was decided. Every OTS chamber offered by Kimball Physics was considered in this design process, eventually landing on the 8 inch "Spherical Square" chamber because it had the highest Raman NA while still maintaining high NA for the other viewports. The high NA on the other viewports is necessary because there are multiple zones that are being addressed on the ion trap.

Figure 7.7 shows an overview of the optical design and the experimental chamber. The trap will be mounted upside down, such that it is facing and parallel to the optics table. The trap is housed in the experimental chamber, which is one of three main portions of the vacuum system. The other two main portions of the vacuum system is the pump chamber and the diagnostic chamber.

7.1 Design Constraints

There are many design constraints that mechanically limit the performance of the machine. This chapter outlines these constraints, provides possible future avenues to increase the performance and analyzes design constraints that are coupled.

7.1.1 Trap Geometry

The geometry of the trap package limits the beams that can be used to address the ions. Most notably, the numerical aperture (NA) across the surface of the trap is between 0.08-0.11 depending on the angle from normal to the isthmus. This requires that beams with a high aspect ratio of about 10:1 to be shaped in order to clear this NA and still address a chain of ions with uniform intensity. The typical ion chain length will be about 60 μm, assuming 16 ions that are spaced 4 μm. The wirebonds on the end of the trap also prevent beams from being sent length-wise along the trap axis.

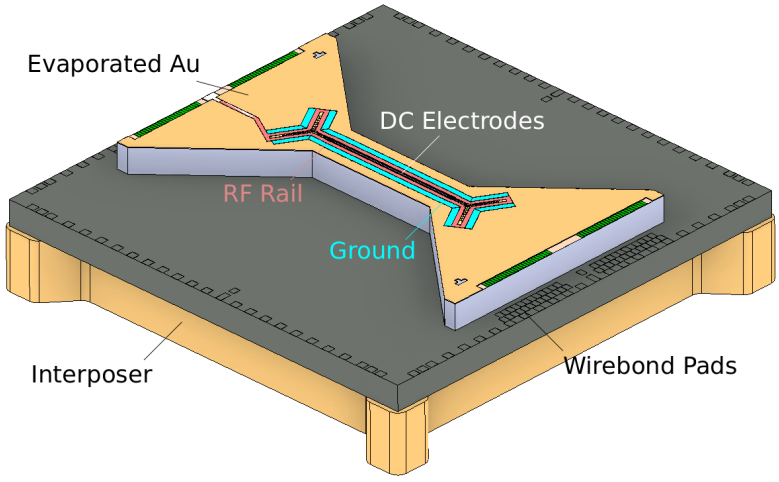

Figure 7.1: Overview of the trap package fabricated at Sandia National Laboratories.

7.1.2 Raman and Imaging Numerical Aperture

The most obvious design constraint that should be considered in the system is the numerical aperture of the Raman re-entrant (RRE) viewports. This is constrained by both the

width of the re-entrant itself and the placement of the loading zone on the chip trap. In this experiment, there are two places along the trap axis that lasers will be focused to manipulate the ions. One is the quantum zone, in the center of the trap, that will be used for high fidelity operations. The other is the loading zone which is meant to reduce contamination at the quantum zone from loading ions and act as a reservoir so that ions can be more quickly loaded into the trap. This zone is about 1 mm away from the quantum zone, which is shown in Figure 3.2. The loading zone needs to be spatially separated from the cooling, measuring, and repumping (CRM) beam because it contains the same frequency of light and the polarization of the CRM beam needs to have the ability to change. This is why the beams are offset 5° in Figure 7.7. Moving the loading zone closer to the quantum zone would allow the RRE to be moved closer to the trap, but would increase contamination from loading at the quantum zone. The other constraint on the NA of the RRE is the width of the re-entrant itself, which limits the clear aperture of the objective focusing onto the ions. In this design, the glass of the RRE is exposed to increase the NA, but otherwise it is limited by the beams that are 45°/50° from the trap axis.

There are a couple of alternative approaches that could have been taken in lieu of using re-entrant viewports that were ultimately decided against. In-vacuum objectives would increase the NA because they could be placed much closer to the trap, however, this would require many custom pairs of objectives mounted on vacuum compatibility stages like ones available from SmarAct GmbH, greatly increasing the complexity and cost of the project. This does have an advantage in that collimated light is being sent into the vacuum chamber, reducing the amount of optomechanical devices outside the chamber. Other than in-vacuum objectives, some designs of chip traps have planar [110] or laser written waveguides [111] that can focus at the ions, but this is more fundamental research and must be integrated into the chip design from the beginning.

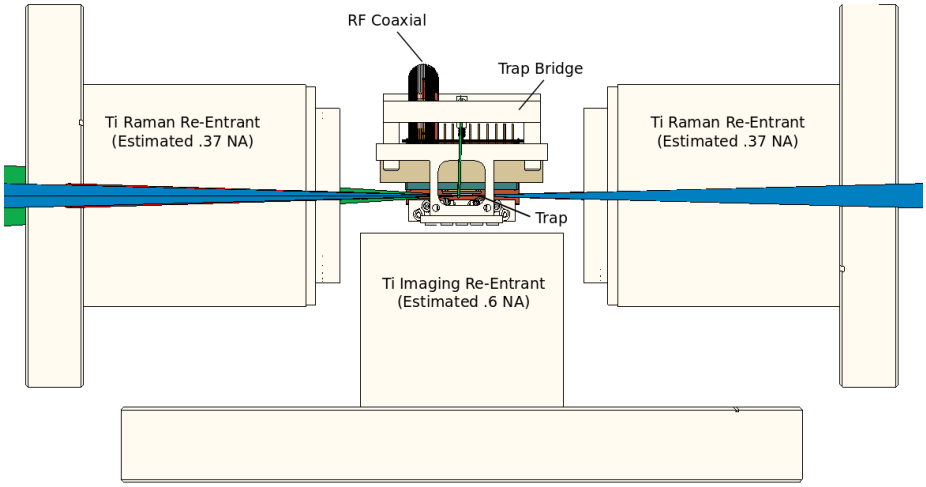

Figure 7.2: Numerical apertures of the re-entrant viewports with each component to relative scale.

7.1.3 Electrical Connectivity and Pumping

The electrical connectivity and pumping are necessary, but secondary in comparison to the optical design. The main constraints imposed by the electrical connectivity are related to the shear number of independent electrodes on the trap requiring a certain size feedthrough. For this connection, the minimum standard connector that can be easily welded onto a vacuum flange is a micro sub-D connector, which has 100 pins with a 0.05 inch pitch. The connection requires a port on the experiment chamber to be used, reducing laser access. This ultimately limits the amount of isotope selective targets that can be installed, but it is necessary to keep the connection short because increasing this connection length would drastically increase the gas load at the trapping site.

The electrical connectivity between this feedthrough and trap will be done with a flexible printed circuit (FPC), while the RF will be carried with a co-axial cable. The FPC is made out of Pyralux® AP, which is partially copper and partially Kapton laminate, rolled together without epoxy. This can be used at UHV, but it has significantly higher outgassing rates than other materials. The width of the FPC is limited by the zero-insertion force (ZIF) socket that mates with the trap package as well as the mounting structure. The FPC is entirely one layer that is folded back on itself to provide more surface area for the many traces. One side of the FPC contains the DC traces and one side contains a ground plane, which is just a layer of copper. The ground plane and DC tracings will be connected

with vias through the FPC. Using a folded FPC made of Pyralux® AP will reduce the crosstalk between DC electrodes and provide better grounding. The connections of the FPC to the vacuum feedthrough will be made with push pins that are soldered on the FPC and that can be pushed onto the micro sub-D connector. The other end of the FPC will be soldered to the ZIF socket. This allows the ZIF and FPC assembly to be cleaned separately from the rest of the chamber and if the FPC needs to be replaced, it can simply be desoldered from the ZIF.

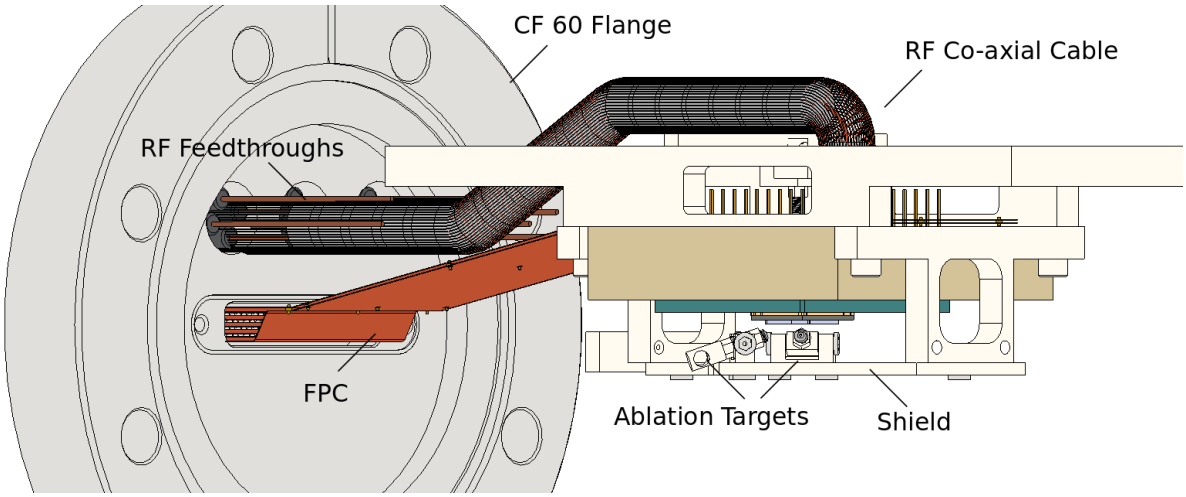

Figure 7.3: Connection of the FPC and RF co-axial cable to the feedthrough.

The design work for the FPC and homebrew co-axial RF cable has been done by Richard Rademacher, a Ph.D. student that is also working on the QuantumIon project. Other projects using chip traps have implemented feedthroughs that directly mate with the ZIF socket [9], but this would require utilizing a larger port that would be useful to pump on. Some groups use bare copper wires that are spaced with macor disks, which reduces the outgassing from the internals like a FPC, but the assembly procedure would be time consuming.

The pumping port on the experimental chamber has a diameter of 14.7 cm, which gives a conductance $\approx$ 1164 liters/sec to the main UHV pumps. This does not constrain the system besides requiring a single port on the experimental chamber, but it is ideal that the pumping port is on the largest port of the experimental chamber.

7.2 Chamber Assemblies

This chapter explains the design of the chamber, which can be broken up into three main sections; the diagnostic chamber, the pump chamber, and the experimental chamber. The diagnostic chamber contains all of the gauges, the residual gas analyzer (RGA), and the valves for initial evacuation. The pump chamber has three different types of pumps installed and will used for mounting the structure. The experimental chamber is where the trap will be mounted with the ablation targets and the feedthrough for electrical connections. The majority of the chamber is titanium, but there are stainless steel components and four places on the chamber there is stainless steel to titanium mating.

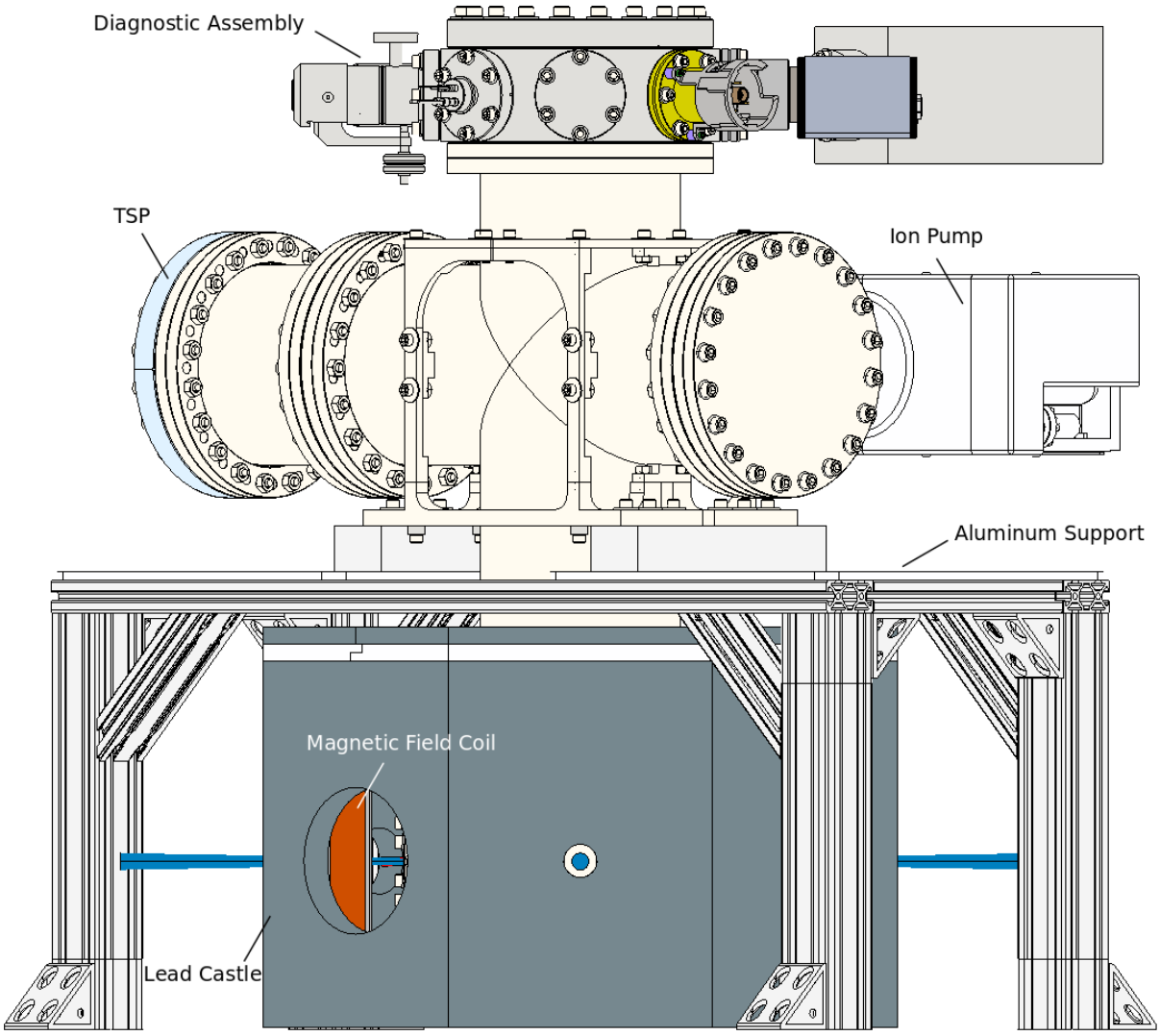

Figure 7.4: Overview of the mounted chamber. A lead castle is necessary for shielding the radioactive barium. The mounting structure is designed to prevent shear forces on titanium welds and provide room for two levels of optics. In reality, the ion pump will be supported as well.

The chambers were designed to allow high conductance to the diagnostic port, while still maintaining a fair distance from the experiment itself. The 5-way cross was designed so that there is no line of site from the TSP to the ion pump or NEG pumps. The height of

the chamber, bolt to bolt, is < 30 inches. This is relatively tall compared to most vacuum chambers in ion trapping experiments and will increase the center of mass of the total weight load on the optics table. The height of the vacuum chamber, the imaging cavity, and the amount of lead wall increase the center of mass of the weight load on the optics table such that, if stability is to be ensured when the table is levitated, the optical table legs must be recessed like in Figure 1.2.

7.2.1 Diagnostic Chamber

This portion of the vacuum chamber houses the diagnostic equipment. The chamber is a stainless steel octagon, chosen to match the thermal expansion coefficient of all the stainless steel CF flanges on the diagnostic equipment. There are two gauges, a residual gas analyzer, a feedthrough, as well as an all metal leak valve and an all metal bake valve. The CF 150 flange on the spherical octagon allows for high conductance to other portions of the vacuum system. Despite this high conductance, there will likely be a substantial pressure differential between this area and the area near the trap at UHV. The trap site has a significantly higher gas load and is quite far from the diagnostic equipment ≈ 60 cm.

The residual gas analyzer (RGA) is attached to the diagnostic subassembly in order to provide basic information about the partial pressures of the gases in the system. It could also be used for leak checking with helium. This particular RGA is from Stanford Research System (SRS) and is specified up to 200 amu. Barium Chloride is 208 amu, but as previous experiments on an Extorr RGA failed to detect this it seems unlikely the SRS model would as well. An electron multiplier addon is necessary for partial pressure measurements $< 10^{-10}$ mbar. This model has a built in Pirani gauge for low level pressure measurements and to shut off the RGA if the pressure rises above a set threshold. RGAs have been installed in XHV environments, but this included a long prebake at high temperatures. Base pressure measurements of those systems were taken when the RGA was switched off. The RGA filament can be baked up to 300° Celsius without the electrical control unit. It is likely that the large RGA filament operating at 70° Celsius will have to be turned off while the trap is in use if it causes the pressure to rise appreciable amounts.

The cold cathode and pirani combination gauge acts as a full range gauge from atmosphere to UHV with $\pm 25\%$ accuracy at UHV. There is a slight magnetic field associated with the cold cathode gauge due to permanent magnets, but the advantage is that it can operate at room temperature without raising the pressure of the chamber. This can be baked to 180° Celsius. In the event that the extractor gauge interferes with trap operations, this gauge can be used to ensure that the chamber is still at UHV (although the ion pump current could be used as well).

The extractor gauge will measure pressures from HV to XHV, $\approx 10^{-13}$ mbar. This is a modified hot cathode bayard-alpert gauge such that the collection filament is shielded from the anode. Due to the x-ray effect and local desorption primarily spurred by the anode, the collection filament can see a number of errors that cause the current to be much higher than what is normally representative of the background pressure in a typical hot cathode gauge.

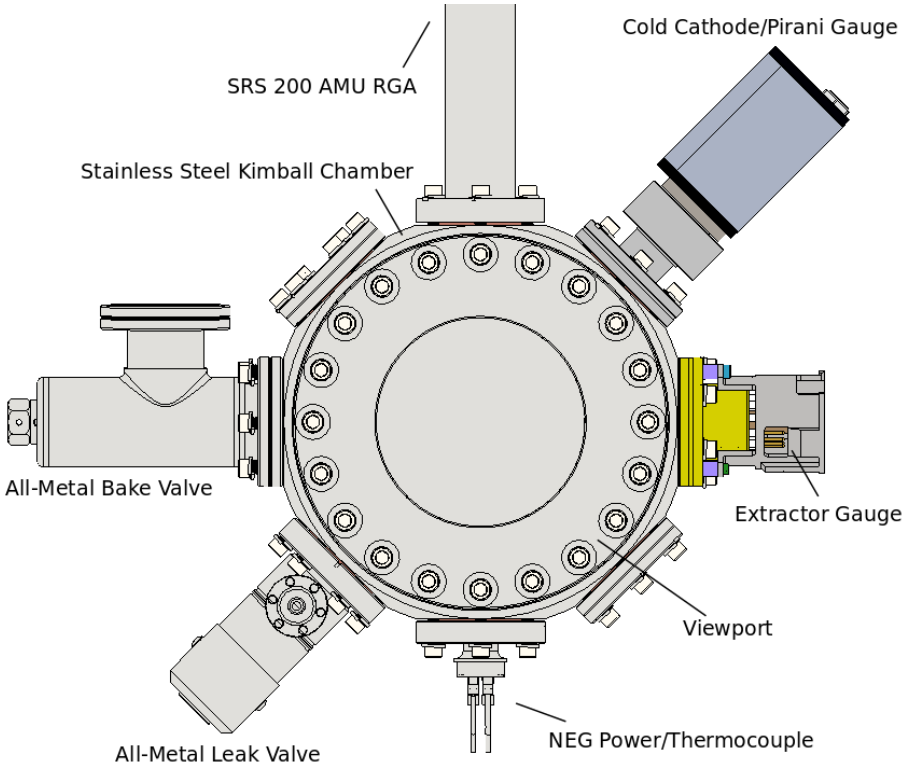

Figure 7.5: Overview of the diagnostic chamber used to measure the base pressure, scan partial pressures, and evacuate the chamber.

The all metal leak valve can be used to introduce argon or another inert gas into the system. This is commonly used for *in situ* trap cleaning applications, but due to the placement of the all metal bake valve to which the turbomolecular pump will be connected, it is unlikely that flow of this gas will take place at the trap site. This may be useful in the event of a small leak so that the chamber can be back filled to preserve the NEGs and trap. The electrical feedthrough provided by SAES will supply the necessary current to

activate the NEG modules. The modules can be wired in series or parallel, but in this case they will be wired in series. Once activated the NEGs will not need to be re-activated until they become saturated. There are also two extra blanks in the event additional diagnostic components need to be attached.

7.2.2 Pump Chamber

The pump chamber houses two NEGs from SAES Getters that are a ZrVTiAl alloy with 1400 liter/sec pumping speeds for H_2 at 10^{-6} mbar. These are the main UHV pumps in the chamber and they must be activated together to avoid saturating each other. These pumps will not capture Argon or hydrocarbons. As previously mentioned, these are placed ≈ 150 mm away from the trap, and with line of sight to the experimental chamber, so the conductance is very high. These pumps do not have line of sight to the trap surface because the trap is mounted upside down. They are mounted on aluminum bridges that will be connected to the Kimball chambers with groove grabbers. The placement of the NEGs limits the conductance to the other pumps, but increases the effective pumping speed of the NEGs.

The TSP is mainly included in the event that the NEGs fail. The placement of the NEGs limits the conductance and could decrease the effective pumping speed of this by up to a factor of two, depending on the specified pumping speed of the TSP at UHV. Activating the TSP could possibly saturate the NEGs, so this should be used in the event that UHV is being lost or initial base pressure is attempting to be recovered. It may be possible to activate the NEGs and TSP at the same time, but it is unlikely that this will cause a significant reduction of pressure at the trapping site if the NEGs are functioning properly.

The ion pump is simply for pumping the non-getterable gases. The specific pump is a starcell 75 liter/second pump, connected with a zero-length reducer. The smaller ion pump was chosen to reduce the weight since the majority of the gases at UHV will be getterable, which can be pumped by the NEGs. The starcell was chosen because it has higher pumping speeds for argon and methane, which are not pumped by NEGs. It has similar pumping speeds for hydrogen molecules as compared to standard diodes, but lower pumping speeds for nitrogen molecules.

The deflection of the frame was simulated in Inventor, with < 100 μm deflection for a load of 1000 lbs. The entire chamber including the frame will be ≈ 200 lbs. The parallelism between the experimental chamber mounting port and the frame is 0.1°, which will make it easier to initially align beams across the trap.

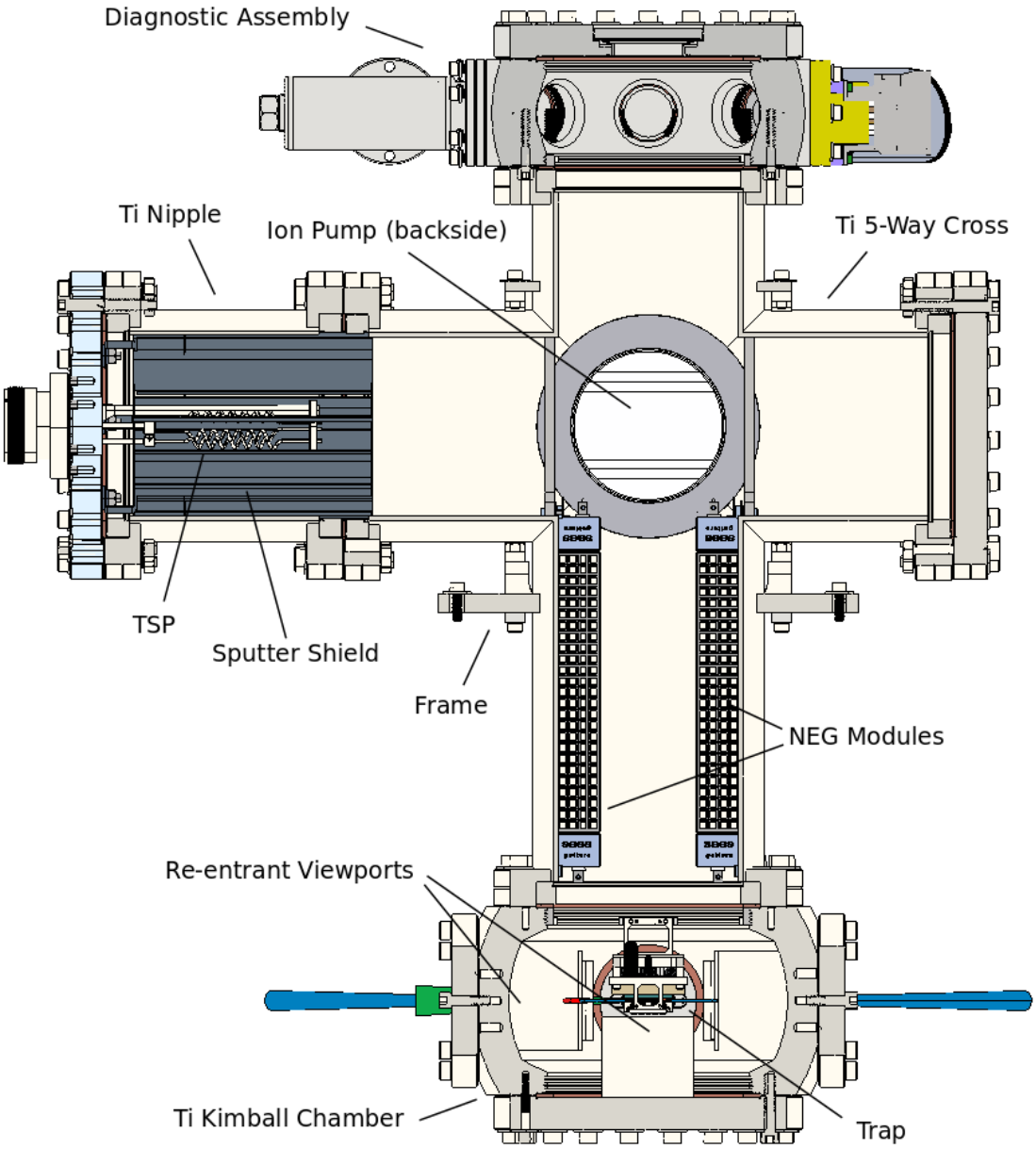

Figure 7.6: Overview of the pump chamber with non-evaporable getters, a TSP, and a starcell ion pump.

7.2.3 Experimental Chamber

The experimental chamber houses the trap and provides all of the optical access to the trap. All of the loading will be done with ablation targets, of which there can be multiple designs depending on how far the targets are placed from the trap. What is shown here is an orientation for working with $^{137}Ba^{+}$ qudits, which is discussed in the optical sections.

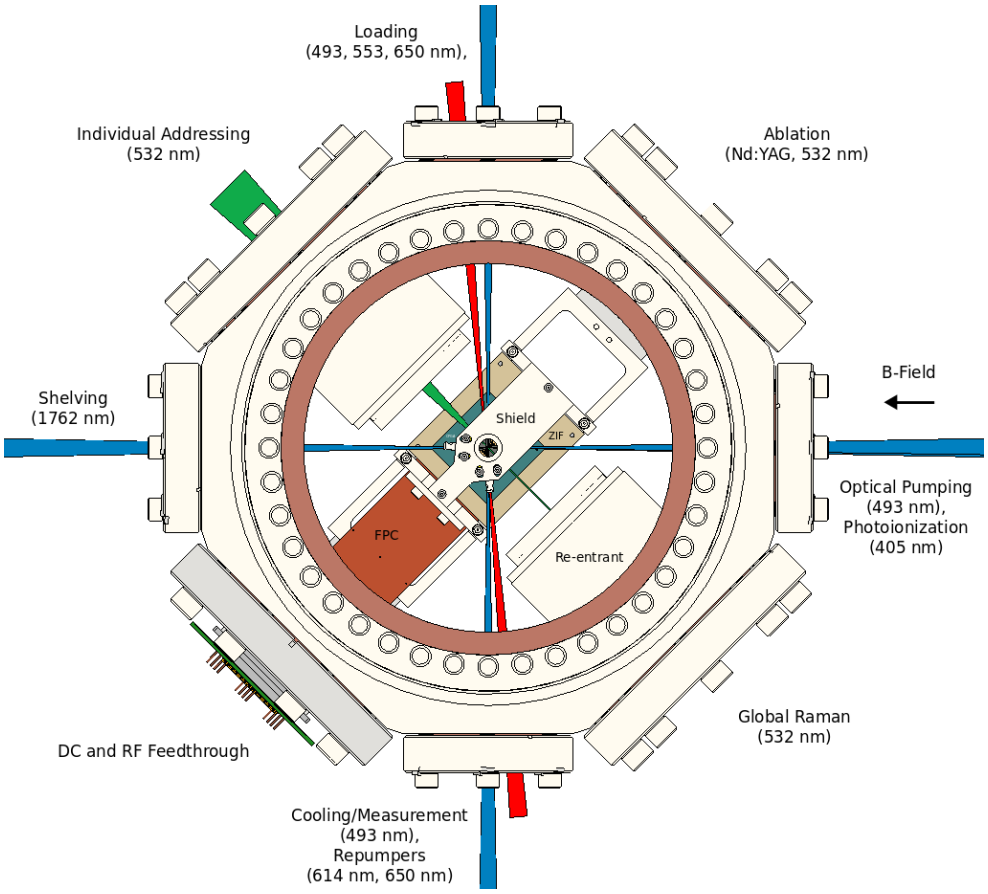

Figure 7.7: Overview of the delivered beams, viewports with text to indicate the initial beam delivery direction. Note that the beams are not perfectly pictured, as many overlap and must be filtered with dichroics. Imaging re-entrant not pictured, but it will be mounted on the port in the foreground. Circular Gaussian beams are drawn in Inventor using the parametric equation tool and revolve. Elliptical Gaussian beams can be approximated by specifying two ellipses and using the loft function to connect them.

The trap is mounted to the Kimball chamber with groove grabbers from each side to ensure greater stability. The trap mounting structure also has cross beams, which increases the frequency of the normal modes. The normal modes of the mounting structure were simulated in Inventor and were on the order of kHz. This will be made out of titanium to match the thermal expansion coefficient of the chamber during baking.

All of the ablation targets are referenced to the trap through the shield and support structures. The ablation targets are designed so that alignment occurs when the ablation tubes are set against the grounding shield. The grounding shield was chosen over using an indium tin oxide (ITO) coated viewport for shielding because, depending on the thickness of the coating, transmission can be only $\approx 85\%$ [112].

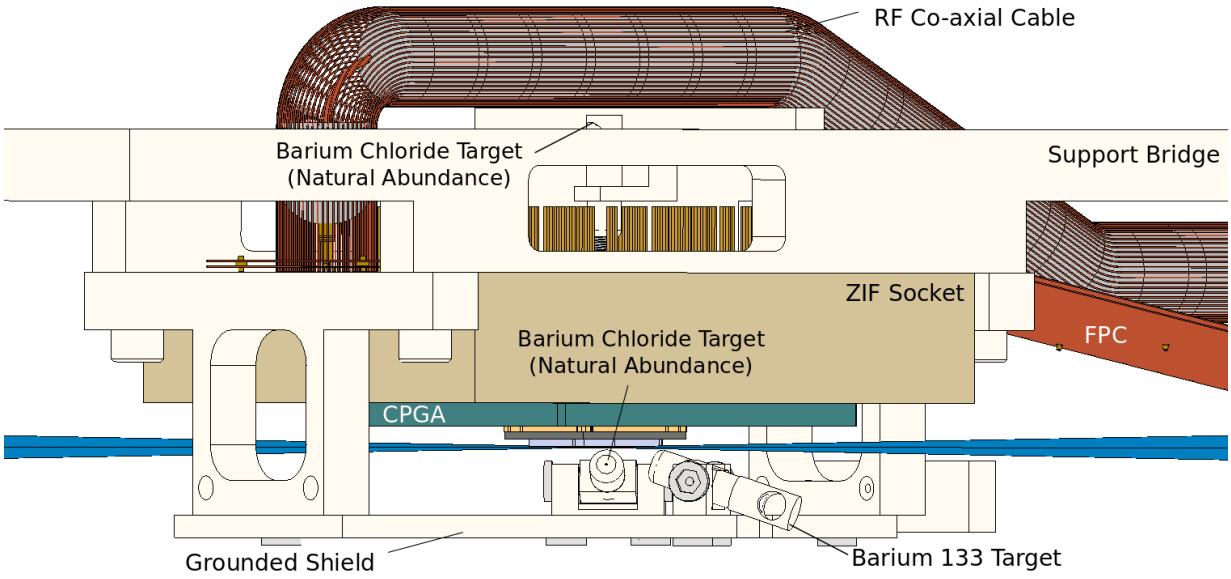

Figure 7.8: Overview of the internals that support the trap. There are three ablation targets and a ground plane to protect the trap potential.

7.3 Molflow Simulations

Molflow is a free Monte Carlo package developed and maintained by a group at CERN. It simulates UHV systems, which can be useful both for estimating the base pressure of this vacuum system as well as simulating different ablation target designs. The package

assumes molecular flow, so particles do not interact. Based on the assigned outgassing rates and sticking coefficients of each surface, the program will calculate the probability at each step of a particle being pumped or desorbing. The desorbing trajectory is pseudo-random. Different gas species can be simulated, but for the most part these simulations will be assuming hydrogen desorption. This program and the basic calculations described in the previous chapter give similar results.

7.3.1 Base Pressure Estimation

The outgassing rates of the materials in the vacuum chamber are approximated from previous literature and summarized in Table 7.1. There will be slightly different heat treatments of the materials in this project, but this is a good basis and will give an accurate estimate of the base pressure.

Material	Outgassing (mbar-l $cm^{-2}s^{-1}$)	Bake Temp.	Bake Time
Stainless Steel	$2{\cdot}10^{-14}$ [14]	400° C	77 hrs
Titanium Alloy	$7{\cdot}10^{-16}$ [12]	150° C	40 hrs
Alumina	$1{\cdot}10^{-12}$ [19]	150° C	2 hrs
PEEK	$6.95{\cdot}10^{-13}$ [18]	200° C	100 hrs
Kapton	$1{\cdot}10^{-12}$ [18]	200° C	100 hrs
MACOR	$5.2{\cdot}10^{-13}$ [20]	250° C	24 hrs

Table 7.1: Outgassing rates used to calculate the following base pressures.

These outgassing rates and the previously mentioned leak rates are used to calculate the base pressures. The pumping speeds of the NEGs, TSP, and starcell ion pump are approximated with nitrogen or hydrogen pumping speeds.

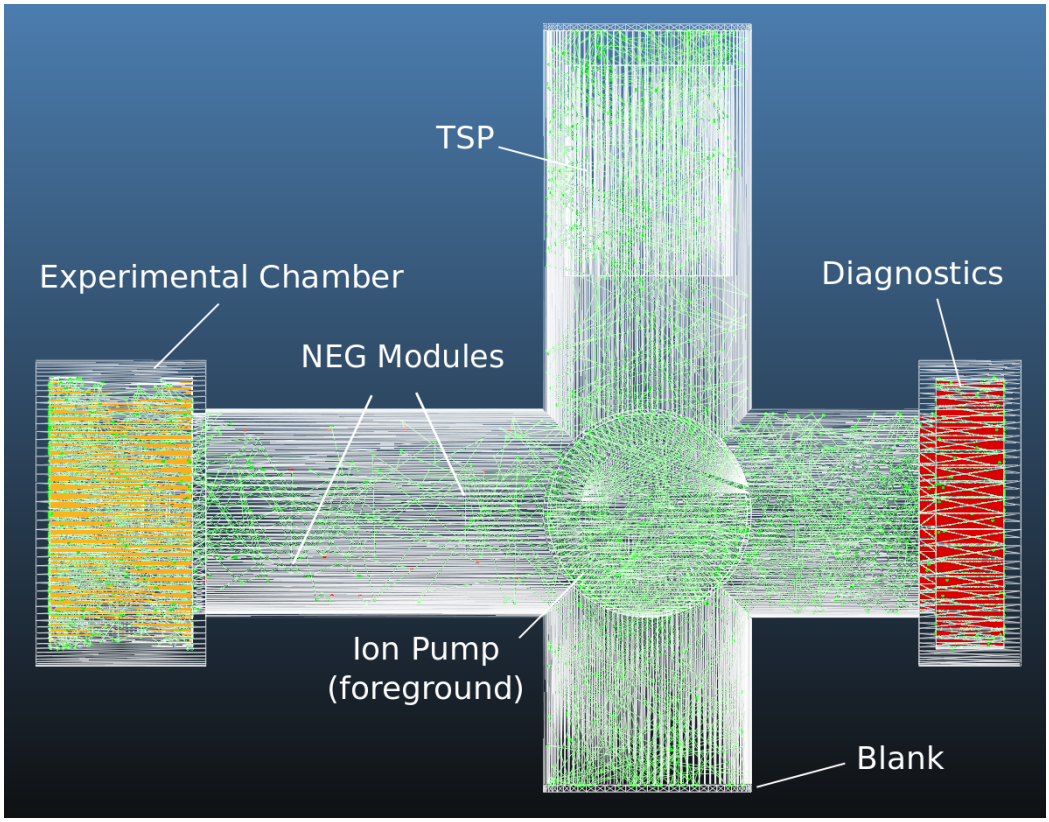

Figure 7.9: Example Molflow simulation with green lines representing the trajectory of molecules. The colored chambers indicate simulated pressures based on the reflection count.

Figure 7.9 shows the simulated vacuum chamber using the Molflow software. The simulation is somewhat simplified from the actual physical system. The geometries are made up of simplified faces as attempting to model the surface of something like a NEG would lead to a complex mesh that would take extraordinary computing power. Any leak rates are approximated by rolling them into the outgassing rate of the surrounding surfaces, creating a higher effective gas load. In this Molflow model, the simplified geometries are created in Inventor and exported as a .stl file. The simplified model includes a FPC, ZIF socket, trap package, grounding shield, and imaging re-entrant viewports as well as Raman re-entrant viewports. The NEGs, TSP, and ion pump are included in the simulation.

The different simulations are ran based on a few different assumptions. These different assumptions account for unknown variables relating to leak rates of the viewports and

feedthroughs and outgassing rates of different materials.

Scenario	Leakage (mbar·l/s)	Trap Pressure (mbar)	Gauge Pressure (mbar)
Optimal	$1{\cdot}10^{-13}$	$1.19{\cdot}10^{-12}$	$\approx 4{\cdot}10^{-13}$
Internal Dominated	$1{\cdot}10^{-13}$	$3.78{\cdot}10^{-10}$	$\approx 9.6{\cdot}10^{-11}$
Leak Dominated	$1{\cdot}10^{-12}$	$1.05{\cdot}10^{-11}$	$\approx 2.5{\cdot}10^{-12}$
SS Chamber	$1{\cdot}10^{-13}$	$4.57{\cdot}10^{-12}$	$\approx 1.1{\cdot}10^{-12}$
NEG Failure	$1{\cdot}10^{-13}$	$3.23{\cdot}10^{-12}$	$\approx 1.5{\cdot}10^{-12}$

Table 7.2: Estimated base pressures based on different outgassing rates of the internals and assumptions of the limiting factors. The leak rates correspond to rates used for each CF seal or viewport.

The optimal case assumes that the gas load at the trap site is limited by both the leak rates and the outgassing rates of the internals and walls. This scenario assumes similar contributions from these sources with a leak rate of $1 \cdot 10^{-13}$ mbar·l/s per viewport or CF seal. It is possible that these leak rates are higher, but if the leak rates are taken to be the rate at which they are guaranteed by the manufacturer, than the system would not reach UHV. This is not plausible as many ion trapping systems reach UHV with viewports from MPF, the manufacturer. The leak rates of CF flanges are so low that vacuum chambers can routinely hit pressures $< 10^{-12}$ mbar [6], so they are often not the limiting factor unless there is a defect in the manufacturing process. For comparison, the leak rates of the all-metal leak valve is $1 \cdot 10^{-12}$ mbar·l/s when it is closed, and this is a variable seal.

The internal dominated case is a worst case scenario if the internals are simply baked during the last step with the titanium chamber. It is identical to the optimal case, except the FPC and ZIF socket have signifincaly higher outgassing rates resulting from short, low temperature bakes [18][21]. This displays the need for different and longer temperature treatments for the internals.

The leak dominated case is a worst case scenario if the internals are properly baked for multiple days at high temperature. This assumes a leak rate of $1 \cdot 10^{-12}$ mbar·l/s per viewport or CF seal. This is still likely an overestimate because pressures of 10^{-12} mbar have been reached with stainless steel vacuum chambers, limited by the internal outgassing rates that have comparable viewport configurations [15].

The stainless steel (SS) chamber case is identical to the optimal case, except all titanium materials were now taken to be pre-baked 304 stainless steel. The leak rates are identical to the leak rates in the optimal case. The NEG failure has identical properties to the optimal case as well, except the NEGs have a sticking factor of zero. In the event that

the NEGs become saturated and cannot be reactivated without rebuilding the system, an acceptable base pressure can still be maintained with the TSP.

The base pressure of the vacuum system is ultimately determined by the types of temperature treatments that the high outgassing internals undergo. Whether the vacuum chamber is mostly titanium or stainless steel, the ZIF and FPC need to be baked at moderate temperatures (200° C) for at least a week otherwise these will serious limiting factors. The ZIF socket can also be made out of materials like Macor that have better outgassing properties. The titanium chamber provides a slight benefit over the stainless steel chamber in terms of base pressure, but if the internals are not properly treated this is not relevant. Again, the main reason the chamber is made out of titanium is due to the weight of an entirely stainless steel chamber. This chamber will be $<$ 200 lbs, while a stainless steel chamber would be $>$ 300 lbs.

The pumping speeds of the NEG modules were taken to be half of the stated value from the manufacturer because the pumping speeds were taken at HV and not UHV. This translates to a .15 sticking factor which was assigned for both the NEG modules and TSP pump [122]. The simulations were ran $>$ 100 million hits, converging quickly.

7.3.2 Ablation Target

The ablation targets were simulated in Molflow as well, which allows the contamination at the quantum zone to be evaluated. The ablation targets are designed with a single aperture, so the atomic flux is not collimated. Integrating two consecutive apertures is necessary to collimate the atomic flux, but this greatly reduces the flux at the loading zone.

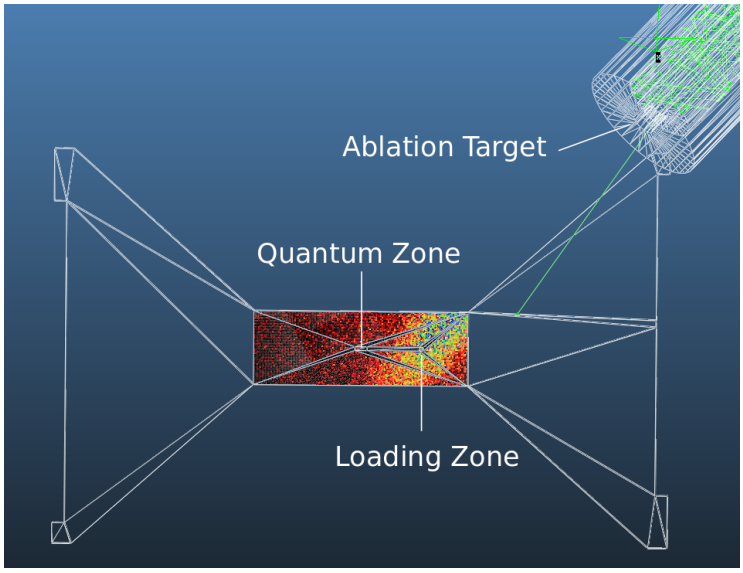

Figure 7.10: Ablation simulation of the flux at the loading zone in comparison to the flux at the quantum zone.

The aperture in the simulation is 400 μm in diameter and the ablation target is 16 mm away from the loading zone. The ablation tube is $>$ 5 mm away from the trap electrodes and will be grounded. There are two identical ablation set ups in the system, but only one is pictured here. The flux present at the quantum zone (3 center electrodes) is 15% of the flux present at the loading zone (3 end electrodes). Atoms or molecules deposited onto surrounding evaporated gold, which are not electrodes, will also increase the anomalous heating rates. The flux that impinges on the surface of the trap is $<$0.1% of the total flux from the ablation target and $\approx$ 0.0002% of the total flux makes it to the loading zone. The trajectory and distribution of the atomic flux is based on work relating to collimated atomic beams from a different group [113]. It is difficult to estimate the exact deposition rates at the various zones on the trap, but by introducing another aperture, this atomic beam could become at least partially collimated. This would greatly reduce the deposition rates at the other zones.

7.4 Baking

Due to the complexity of chamber, baking will be done in four stages. There will be a higher temperature prebake for the stainless steel components, a lower temperature prebake for

the diagnostics, an even lower temperature prebake for the internals, and a final bake with the assembled vacuum chamber.

Material/Item	Max. Temp.	Bake Temp.	Bake Time
SS Kimball Chamber	450° C	425° C	120 hrs
SS CF 150 Nipple	450° C	425° C	120 hrs
SS NEG Mounts	450° C	425° C	120 hrs
SS TSP Shield	450° C	425° C	120 hrs
SS Groove Grabbers	450° C	425° C	120 hrs

Table 7.3: Prebaking of large surface area stainless steel components to high temperature. This will be the first prebake and the final 24 hours will be an air-bake to create an oxide layer. The stainless steel (SS) nipple is for mounting purposes only and not part of the final chamber.

Material/Item	Max. Temp.	Bake Temp.	Bake Time
Ti Kimball Chamber	300° C	300° C	120 hrs
Ti Internals	300° C	300° C	120 hrs
RGA Filament	300° C	300° C	120 hrs
Custom Feedthrough	350° C	300° C	120 hrs
Extractor Gauge	400° C	300° C	120 hrs

Table 7.4: Prebaking of diagnostic equipment and titanium experiment chamber. The stainless steel components from before will be included again for extra baking and mounting purposes.

Material/Item	Max. Temp.	Bake Temp.	Bake Time
FPC/ZIF	200° C	200° C	120 hrs

Table 7.5: Prebaking of internals. Again, the components from before will be included again for extra baking. This bake will take place after the ZIF socket and FPC have been soldered together and cleaned.

The final bake will be done at 180° C for 48 hours and it will include the entire chamber and frame. It may be possible to bake the FPC and ZIF socket concurrently with the prebake of the stainless steel materials to reduce total baking time. The trap will only be included in the final bake.

Chapter 8

Final Remarks

Both vacuum and optical designs are presented for an open-access trapped ion computer. The vacuum design includes all relevant mechanical aspects like mounting the trap, ablation targets, and vacuum chamber, as well as electrical and optical access for controlling and addressing chains of ions in a Sandia chip trap. The pumping and diagnostic considerations are designed around the optical access and simulated results indicate base pressures well into the UHV regime ($< 1 \cdot 10^{-11}$ mbar), which is sufficient for trapping tens of ions for up to minutes at a time. Optical designs and simulations for driving resonant or near-resonant atomic transitions in chains of barium ions are also presented based on off-the-shelf refractive optics for two separate trapping zones. Optical simulations of the CW beam paths show >95% intensity uniformity across a chain of 16 ions that are spaced by 4 microns with minimal power clipping on the trap and low crosstalk at neighboring trapping zones. Relevant optomechnical devices are included on each beam path to ensure full positional control of the focus at the ion and enough throw to correct for slow thermal drifts. Positional sensors are included in the designs for initial beam pointing calibration routines, both before and after the vacuum chamber.

Once the system has been further designed and built, there are many possible areas of research that could be explored for producing novel work. Most notably these areas include isotope selective loading, ion shuttling, performing parallel gates with qudits, as well as gate optimization. In the longer term, it may be possible to implement error correcting codes for a single qubit with this system, but it would require all of the previously mentioned areas to have already been developed to a certain extent on the machine.

References

[1] NexTorr Z, NexTorr D, NexTorr D StarCell [Pamphlet]. (n.d.). SAES Group.

[2] Feynman, R. 1983. Tiny Computers Obeying Quantum Mechanical Laws. Talk delivered at Los Alamos National Laboratory. New Directions in Physics: The Los Alamos 40th Anniversary Volume. 1987.

[3] Islam, K.R., (2019, Fall). Personal Communication.

[4] Audi, M. An Introduction to An Introduction to Ion Pumps Ion Pump. CERN Accelerator School, May 2006.

[5] Benvenuti, C. (n.d.). Getter pumping. R&B Energy Research, Geneva, Switzerland.

[6] Maccallini, E., Manini, P., Conte, A., Siviero, F., & Bonucci, A. (2012). New Approach to meet vacuum requirements in UHV/XHV systems by Non Evaporable Getter Technology. Journal of Physics: Conference Series, 390, 012006. doi:10.1088/1742-6596/390/1/012006

[7] Benvenuti, C., & Chiggiato, P. (1993). Obtention of pressures in the 1014 torr range by means of a ZrVFe non evaporable getter. Vacuum, 44(5-7), 511-513. doi:10.1016/0042-207x(93)90084-n

[8] Malyshev, O. (2011). Non-Evaporable Getters. STFC Daresbury Laboratory.

[9] Graham, R. D., Chen, S., Sakrejda, T., Wright, J., Zhou, Z., & Blinov, B. B. (2014). A system for trapping barium ions in a microfabricated surface trap. AIP Advances, 4(5), 057124. doi:10.1063/1.4879817

[10] Pagano, G., Hess, P. W., Kaplan, H. B., Tan, W. L., Richerme, P., Becker, P., . . . Monroe, C. (2018). Cryogenic trapped-ion system for large scale quantum simulation. Quantum Science and Technology, 4(1), 014004. doi:10.1088/2058-9565/aae0fe

[11] Monroe, C., Meekhof, D. M., King, B. E., Jefferts, S. R., Itano, W. M., Wineland, D. J., & Gould, P. (1995). Resolved-Sideband Raman Cooling of a Bound Atom to the 3D Zero-Point Energy. Physical Review Letters, 75(22), 4011-4014.

[12] Kurisu, H., Ishizawa, K., Yamamoto, S., Hesaka, M., & Saito, Y. (2008). Application of titanium materials to vacuum chambers and components. Journal of Physics: Conference Series, 100(9), 092002. doi:10.1088/1742-6596/100/9/092002

[13] Watanabe, F. (2004). Extremely low-outgassing material: 0.2 beryllium copper alloy. Journal of Vacuum Science & Technology A: Vacuum, Surfaces, and Films, 22(1), 181-191. doi:10.1116/1.1635390

[14] Sefa, M., Fedchak, J. A., & Scherschligt, J. (2017). Investigations of medium-temperature heat treatments to achieve low outgassing rates in stainless steel ultrahigh vacuum chambers. Journal of Vacuum Science & Technology A: Vacuum, Surfaces, and Films, 35(4), 041601. doi:10.1116/1.4983211

[15] P. Obšil, A. Lešundák, T. Pham, K. Lakhmanskiy, L. Podhora, M. Oral, O. Číp, L. Slodička. (2019). Hydrogen pressure at 1012 mBar level in a room temperature ion trapping apparatus. doi: arXiv:1904.13242

[16] Yoshimura, N., Hirano, H., Sato, T., Ando, I., & Adachi, S. (1991). Outgassing characteristics and microstructure of a "vacuum fired" (1050°C) stainless steel surface. Journal of Vacuum Science & Technology A: Vacuum, Surfaces, and Films, 9(4), 2326-2330. doi:10.1116/1.577317

[17] Chen, J. R., Lee, C. H., & Liu, Y. C. (1988). A comparison of thermal outgassing rates of aluminum alloy and stainless steel vacuum chambers. AIP Conference Proceedings. doi:10.1063/1.37306

[18] Hedlund, E. (n.d.). The need for more outgassing data of materials for accelerators and storage ring experiments. SP-Swedish Testing and Research Institute. Uppsala University, Sweden.

[19] Katharina Battes *et al.* Outgassing Behavior of Different Oxide Ceramic Materials. AVS 64th International Symposium Exhibition. November 2, 2017, 4:00 pm, Room 9.

[20] Ari Riihimaki. Outgassing Studies of Some Accelerator Materials (masters thesis). UNIVERSITY OF HELSINKI.

[21] Brando Okolo. 3D printed PEEK for vacuum technology. Jul 2016. Research Gate, 10.13140/RG.2.1.3330.8406.

[22] Regina Lechner, Christine Maier, Cornelius Hempel, Petar Jurcevic, Ben P. Lanyon, Thomas Monz, Michael Brownnutt, Rainer Blatt, and Christian F. Roos. Electromagnetically-induced-transparency ground-state cooling of long ion strings. Phys. Rev. A 93, 053401.

[23] Rotter, D. (2008). Quantum feedback and quantum correlation measurements with a single Barium ion (doctoral dissertation). University of Innsbruck, Innsbruck, Austria.

[24] Leibrandt, D. (2009). Integrated chips and optical cavities for trapped ion quantum information processing (doctoral dissertation). Massachusetts Institute of Technology, Cambridge, Massachusetts.

[25] Heinrich, J. (2018). THESE DE DOCTORAT DE SORBONNE UNIVERSITE (doctoral dissertation). Université d'Évry-Val-d'Essonne.

[26] Lindenfelser, F. (2017). Broadband cooling on a forbidden transition in a novel high-optical-access ion trap (doctoral dissertation). ETH Zurich.

[27] Zhang, X. (2018). Quantum Computation and Simulation with Trapped Ions (doctoral dissertation). Tsinghua University.

[28] Hucul, D. (2015). A Modular Quantum System of Trapped Atomic Ions (doctoral dissertation). University of Maryland.

[29] Højbjerre, K., 2009. "Experiments with cold trapped molecular ions" (doctoral thesis). Danish National Research Foundation Center for Quantum Optics - Quantop. Department of Physics and Astronomy, Aarhus University.

[30] H.A. Fürst. Trapped ions in a bath of ultracold atoms (doctoral thesis). Van der Waals-Zeeman Institute (WZI). 9 January 2019.

[31] Frank Ziesel, (2013) "Quantum State Manipulation and Dynamics in Micro Ion Traps" (doctoral thesis). Johannes Gutenberg-Universität Mainz.

[32] Norbert Matthias Linke. "Background-free detection and mixed-species crystals in micro- and macroscopic ion-traps for scalable QIP." (doctoral thesis). New College, University of Oxford.

[33] Mcconnell, R., Bruzewicz, C., Chiaverini, J., & Sage, J. (2015). Reduction of trapped-ion anomalous heating byin situsurface plasma cleaning. Physical Review A, 92(2). doi:10.1103/physreva.92.020302

[34] Hite, D. A., Colombe, Y., Wilson, A. C., Brown, K. R., Warring, U., Jördens, R., . . . Wineland, D. J. (2012). 100-Fold Reduction of Electric-Field Noise in an Ion Trap Cleaned withIn SituArgon-Ion-Beam Bombardment. Physical Review Letters, 109(10). doi:10.1103/physrevlett.109.103001

[35] Allcock, D. T., Guidoni, L., Harty, T. P., Ballance, C. J., Blain, M. G., Steane, A. M., & Lucas, D. M. (2011). Reduction of heating rate in a microfabricated ion trap by pulsed-laser cleaning. New Journal of Physics, 13(12), 123023. doi:10.1088/1367-2630/13/12/123023

[36] Rushton, J. A., Aldous, M., & Himsworth, M. D. (2014). Contributed Review: The feasibility of a fully miniaturized magneto-optical trap for portable ultracold quantum technology. Review of Scientific Instruments, 85(12), 121501. doi:10.1063/1.4904066

[37] CF Blank Flange. (n.d.). CF Blank Flange. Retrieved from https://www.pfeiffer-vacuum.com/en/products/chambers-components/components/cf/cf-flanges/6675/cf-blank-flange

[38] K Mukugi, H Tsuchidate, N Oishi. Characteristics of cold cathode gauges for outgassing measurements in uhv range, Vacuum. Volume 44, Issues 5-7, 1993, Pages 591-593.

[39] Pressure Measurement Technical Notes. (n.d.). Retrieved May 14, 2020, from https://www.lesker.com/newweb/gauges/gauges_technicalnotes_1.cfm.

[40] CF Flanges Technical Notes. (n.d.). Retrieved May 18, 2020, from https://www.lesker.com/newweb/flanges/flanges_technicalnotes_conflat_1.cfm

[41] Pump Classifications Technical Notes. (n.d.). Retrieved May 17, 2020, from https://www.lesker.com/newweb/vacuum_pumps/vacuumpumps_technicalnotes_1.cfm

[42] Kurt J. Lesker Company. (n.d.). Retrieved July 08, 2020, from https://www.lesker.com/newweb/vacuum_pumps/ionpump_gamma_ionpump_tisub.cfm.

[43] Wolfgang Paul – Nobel Lecture. NobelPrize.org. Nobel Media AB 2020. Sat. 27 Jun 2020. https://www.nobelprize.org/prizes/physics/1989/paul/lecture/.

[44] K. Jousten. Ultrahigh vacuum gauges. Physikalisch-Technische Bundesanstalt, 10587 Berlin, Germany.

[45] Rademacher, R. (2020). Design of a Real-Time Embedded Control System for Quantum Computing Experiments (masters thesis). University of Waterloo.

[46] Bramman, B. (2019). Measuring Trapped Ion Qudits (masters thesis). University of Waterloo.

[47] Kotibhaskar, N. (2019). Design and construction of an ion trapping apparatus for quantum simulation experiments (masters thesis). University of Waterloo.

[48] Motlakunta, S. (2018). Developing theoretical and experimental tools for a hybrid quantum simulator based on trapped ions (masters thesis). University of Waterloo.

[49] Schäfer, V., Ballance, C., Thirumalai, K. et al. Fast quantum logic gates with trapped-ion qubits. Nature 555, 75–78 (2018).

[50] Maunz, Peter, Mizrahi, Jonathan, and Goldberg, Josh. IonControl v. 1.0. Computer software. https://www.osti.gov//servlets/purl/1326630. Vers. 00. USDOE. 15 Jul. 2016. Web.

[51] Peter Maunz. High optical access trap 2.0. Technical Report SAND2016-0796R, Sandia National Laboratories, January 2016.

[52] Nicholas D. Guise *et al.* Ball-grid Array Architecture for Microfabricated Ion Traps. Journal of Applied Physics 117, 174901 (2015).

[53] Daniel A. Steck, Quantum and Atom Optics, available online at http://steck.us/teaching (revision 0.12.5, 26 January 2019).

[54] Wang, Y., Um, M., Zhang, J. et al. Single-qubit quantum memory exceeding ten-minute coherence time. Nature Photon 11, 646–650 (2017).

[55] Wright, K., Beck, K.M., Debnath, S. et al. Benchmarking an 11-qubit quantum computer. Nat Commun 10, 5464 (2019).

[56] Ballance, C. J. and Harty, T. P. and Linke, N. M. and Sepiol, M. A. and Lucas, D. M. High-Fidelity Quantum Logic Gates Using Trapped-Ion Hyperfine Qubits. Phys. Rev. Lett. 117, 060504 – Published 4 August 2016.

[57] Michael A. Nielsen and Isaac L. Chuang. 2011. Quantum Computation and Quantum Information: 10th Anniversary Edition (10th. ed.). Cambridge University Press, USA.

[58] Preskill, John. Quantum Computing in the NISQ era and beyond. Quantum 2, 79 (2018). https://arxiv.org/abs/1801.00862.

[59] Christensen, J.E., Hucul, D., Campbell, W.C. et al. High-fidelity manipulation of a qubit enabled by a manufactured nucleus. npj Quantum Inf 6, 35 (2020). https://doi.org/10.1038/s41534-020-0265-5.

[60] Elia Perego, Marco Pomponio, Amelia Detti, Lucia Duca, Carlo Sias, and Claudio E. Calosso. A scalable hardware and software control apparatus for experiments with hybrid quantum systems. Review of Scientific Instruments 89, 113116 (2018).

[61] Natalie C. Brown and Kenneth R. Brown. Leakage mitigation for quantum error correction using a mixed qubit scheme. PHYSICAL REVIEW A 100, 032325 (2019).

[62] Hans Karlsson and Ulf Litzén. Revised Ba I and Ba II Wavelengths and Energy Levels Derived by Fourier Transform Spectroscopy.Phys. Scr. 60 321. (1999).

[63] David S. Smith and Michael G. Stabin. Exposure rate constants and lead shielding values for over 1,100 radionuclides .Health Phys. 2012 Mar; 102(3) : 271-91.

[64] Dave Hucel et al. "133Ba+: High fidelity goldilocks qubits" SPIE Quantum Information Science, Sensing, and Computation XII, Session 2: Quantum Computing II, Online.

[65] A. Walther, F. Ziesel, T. Ruster, S. T. Dawkins, K. Ott, M. Hettrich, K. Singer, F. Schmidt-Kaler, and U. Poschinger. Controlling Fast Transport of Cold Trapped Ions. PRL 109, 080501 (2012).

[66] D. L. Moehring , C. Highstrete, D. Stick, K. M. Fortier, R. Haltli, C. Tigges and M. G. Blain. Design, fabrication and experimental demonstration of junction surface ion traps. New Journal of Physics 13 (2011) 075018.

[67] "Zemax." Wikipedia, Wikimedia Foundation, 7 Nov. 2019, en.wikipedia.org/wiki/Zemax.

[68] "Edmund Optics." Comparison of Optical Aberrations - Edmund Optics, web.archive.org/web/20111206062508/www.edmundoptics.com/technical-support/optics/comparison-of-optical-aberrations/.

[69] "Edmund Optics." Chromatic and Monochromatic Optical Aberrations - Edmund Optics, web.archive.org/web/20111206061647/www.edmundoptics.com/technical-support/optics/chromatic-and-monochromatic-optical-aberrations/.

[70] "Zernike Polynomials". Wyant College of Optical Sciences, University of Arizona. Class06-08. https://wp.optics.arizona.edu/visualopticslab/wp-content/uploads/sites/52/2016/08/Class06_08.pdf

[71] Lakshminarayanan, Vasudevan Fleck, Andre. (2011). Zernike polynomials: A guide. Journal of Modern Optics - J MOD OPTIC. 58. 1678-1678. 10.1080/09500340.2011.633763.

[72] G. Ghosh, "Sellmeier coefficients and dispersion of thermo-optic coefficients for some optical glasses," Appl. Opt. 36, 1540-1546 (1997).

[73] Jose Sasian, Weichuan Gao, and Yufeng Yan. "Method to design apochromat and superachromat objectives.". Optical Engineering 56(10), 105106 (October 2017).

[74] Geert Vrijsen, Yuhi Aikyo, Robert F. Spivey, Volkan Inlek, and Jungsang Kim. Efficient isotope-selective pulsed laser ablation loading of 174Yb+ ions in a surface electrode trap. Vol. 27, No. 23 / 11 November 2019 / Optics Express 33907.

[75] Peter D. D. Schwindt, Yuan-Yu Jau, Heather Partner, Adrian Casias, Adrian R. Wagner, Matthew Moorman, Ronald P. Manginell, James R. Kellogg, and John D. Prestage. A highly miniaturized vacuum package for a trapped ion atomic clock. Rev. Sci. Instrum. 87, 053112 (2016).

[76] Spivey, R., and 7 colleagues 2017. Characterization of a Compact Cryogenic Package Approach to Ion Trap Quantum Comuting. APS March Meeting Abstracts 2017, G1.372.

[77] Leschhorn, G., Hasegawa, T. Schaetz, T. Efficient photo-ionization for barium ion trapping using a dipole-allowed resonant two-photon transition. Appl. Phys. B 108, 159–165 (2012).

[78] Smith, Warren J. Modern Optical Engineering. 3rd ed., McGraw-Hill, 2000.

[79] Ahi, K. (2017). Mathematical Modeling of THz Point Spread Function and Simulation of THz Imaging Systems. IEEE Transactions on Terahertz Science and Technology, 7(6), 747–754.

[80] Goodwin, B. (n.d.). What is the difference between the FFT and Huygens PSF? Retrieved May 9, 2020, from https://my.zemax.com/en-US/Knowledge-Base/kb-article/?ka=KA-01494

[81] Thom, J., Yuen, B., Wilpers, G. et al. Intensity stabilisation of optical pulse sequences for coherent control of laser-driven qubits. Appl. Phys. B 124, 90 (2018).

[82] Christian Felix Roos. Controlling the quantum state of trapped ions (doctoral thesis). University of Innsbruck.

[83] J Roßnagel et al. Fast thermometry for trapped ions using dark resonances. 2015 New J. Phys. 17 045004.

[84] S. Knünz, M. Herrmann, V. Batteiger, G. Saathoff, T. W. Hänsch, and Th. Udem. Sub-millikelvin spatial thermometry of a single Doppler-cooled ion in a Paul trap. Phys. Rev. A 85, 023427.

[85] R. J. Epstein et al. Simplified motional heating rate measurements of trapped ions. Phys. Rev. A 76, 033411.

[86] K. A. Landsman, Y. Wu, P. H. Leung, D. Zhu, N. M. Linke, K. R. Brown, L. Duan, and C. Monroe. Two-qubit entangling gates within arbitrarily long chains of trapped ions. arXiv:1905.10421.

[87] "Achromatic Lens." Wikipedia, Wikimedia Foundation, 15 Jan. 2020, en.wikipedia.org/wiki/Achromatic_lens.

[88] Grahame Vittorini. December 2013. STABILITY OF ION CHAINS IN A CRYOGENIC SURFACE-ELECTRODE ION TRAP (doctoral thesis). Georgia Institute of Technology.

[89] Brown, K., Kim, J. Monroe, C. Co-designing a scalable quantum computer with trapped atomic ions. NPJ Quantum Inf 2, 16034 (2016).

[90] David P. DiVincenzo. The Physical Implementation of Quantum Computation. IBM. arXiv:quant-ph/0002077.

[91] Kielpinski, D., Monroe, C. Wineland, D. Architecture for a large-scale ion-trap quantum computer. Nature 417, 709–711 (2002).

[92] Franz Kärtner. 6.974 Fundamentals of Photonics: Quantum Electronics. Spring 2006. Massachusetts Institute of Technology: MIT OpenCourseWare, https://ocw.mit.edu.

[93] Kolasinski, K. W. (2020). Surface science: foundations of catalysis and nanoscience. Hoboken, NJ, USA: John Wiley Sons, Inc.

[94] Laurendeau, N. M. (2011). Statistical thermodynamics: fundamentals and applications. Cambridge: Cambridge University Press.

[95] P. A. Redhead. Recommended practices for measuring and reporting outgassing data. National Research Council, Ottawa ON K1A 0R6, Canada. https://www.avs.org/AVS/files/67/67a0c198-fee7-4f19-9e37-19605e2fd0df.pdf.

[96] D. J. McCarron. A Guide to Acousto-Optic Modulators. December 7, 2007. http://jila1.nickersonm.com/papers/A%20Guide%20to%20Acousto-Optic%20Modulators.pdf

[97] Vibhu Vivek. OPTICAL SWITCHES. October 3, 1999. University of Arizona. https://wp.optics.arizona.edu/milster/wp-content/uploads/sites/48/2016/06/acousto-optics-modulator.pdf.

[98] Technical Note: Electro-Optic Modulator FAQs. (n.d.). Retrieved March 5, 2020, from https://www.newport.com/n/electro-optic-modulator-faqs

[99] Flange Systems. (n.d.). Retrieved May 21, 2020, from https://www.vacom.de/en/service/vacuum-specific-measurement/leak-test-for-vacuum/290-en/products/standard-components/flange-systems

[100] Woodgate, G. K. (1983). Elementary Atomic Structure. Oxford University Press.

[101] E. Kim, A. Safavi-Naini, D. A. Hite, K. S. McKay, D. P. Pappas, P. F. Weck, and H. R. Sadeghpour. Electric-field noise from carbon-adatom diffusion on a Au(110) surface: First-principles calculations and experiments. PHYSICAL REVIEW A 95, 033407 (2017).

[102] Pei Jiang Low, Brendan M. White, Andrew A. Cox, Matthew L. Day, Crystal Senko. Practical trapped-ion protocols for universal qudit-based quantum computing. https://arxiv.org/abs/1907.08569.

[103] O'Leary, D. P., Brennen, G. K., Bullock, S. S. (2006). Parallelism for quantum computation with qudits. Physical Review A - Atomic, Molecular, and Optical Physics, 74(3), 1-11. [032334].

[104] Claude Cohen-Tannoudji, Alfred Kastler, I Optical Pumping, Progress in Optics. Volume 5, 1966, Pages 1-81, ISSN 0079-6638, ISBN 9780444533371.

[105] John Preskill. Fault-tolerant quantum computation. arXiv: quant-ph/9712048.

[106] Gregers Poulsen (2011). Sideband Cooling of Atomic and Molecular Ions (doctoral thesis). University of Aarhus.

[107] J.-S. Chen, K. Wright, N.C. Pisenti, D. Murphy, K.M. Beck, K. Landsman, J.M. Amini, and Y. Nam. Efficient sideband cooling protocol for long trapped-ion chains. arXiv:2002.04133.

[108] Caroline Champenois. Trapping and cooling of ions. DEA. du 6 au 10 octobre a l'ecole de Physique des Houches,ecole predocotorale sur les atomes froids et la condensation de Bose-Einstein, 2008, pp.28. ffcel-00334152f

[109] Fred Atoneche, Anders Kastberg. Simplified approach for quantitative calculations of optical pumping. European Journal of Physics, European Physical Society, 2017, 38, pp.45703 - 45703.

[110] Mehta, K., Bruzewicz, C., McConnell, R. et al. Integrated optical addressing of an ion qubit. Nature Nanotech 11, 1066–1070 (2016).

[111] Microfabricated Optics for Quantum Control of Trapped Ions Day, M. (Author). 6 Nov 2018.

[112] Hadi Askari, Hamidreza Fallah, Mehdi Askari, and Mehdi Charkhchi Mohmmadieyh. Electrical and optical properties of ITO thin films prepared by DC magnetron sputtering for low-emitting coatings. September 2014. arXiv:1409.5293.

[113] Li, C., Chai, X., Wei, B., Yang, J., Daruwalla, A., Ayazi, F., & Raman, C. (2019). Cascaded collimator for atomic beams traveling in planar silicon devices. Nature Communications, 10(1). doi:10.1038/s41467-019-09647-3

[114] Stutzman, M., Adderley, P., Mamun, M., & Poelker, M. (2019). Non-evaporable getter coating chambers for extreme high vacuum. doi:arXiv:1803.07056

[115] Prodromides, A. (2002). Non-Evaporable Getter Thin Film Coatings for Vacuum Applications. These No. 2652.

[116] Mamun, M. A., Elmustafa, A. A., Stutzman, M. L., Adderley, P. A., & Poelker, M. (2014). Effect of heat treatments and coatings on the outgassing rate of stainless steel chambers. Journal of Vacuum Science & Technology A: Vacuum, Surfaces, and Films, 32(2), 021604. doi:10.1116/1.4853795

[117] Benvenuti, C. & Escudeiro Santana, A & Ruzinov, V. (2001). Ultimate pressures achieved in TiZrV sputter-coated vacuum chambers. Vacuum. 60. 279-284. 10.1016/S0042-207X(00)00389-4.

[118] Zheng, S. (1993). Conductance Calculation - Molecular Flow, Long Tube of Circular Cross Section. GEM TN-93-382.

[119] Duniway Stockroom. TECH TIPS- Conductance of a Tube. Duniway MP16.

[120] Leybold Vacuum. Fundamentals of Vacuum Technology. Kat.-Nr. 199 90.

[121] Agilent Technologies. HIGH AND ULTRA-HIGH VACUUM FOR SCIENCE RESEARCH. Kat.-Nr. 199 90.

[122] CapaciTorr D, CapaciTorr Z, UHV 1400 Wafer Module [Pamphlet]. (n.d.). SAES Group.

[123] Day, M., (2020, Spring). Personal Communication.

[124] Nicolosi, D., (2019, Spring). Personal Communication.

[125] Thorlabs. POLARIS-K1S2P Specifications. Retrieved July 11, 2020, from https://www.thorlabs.com/drawings/d4ceeb436816e5ed-7A2794BC-B885-F620-3CAEB7CD3F604C42/POLARIS-K1S2P-SpecSheet.pdf.

[126] Kosky, P. G., Balmer, R. T., Keat, W., amp; Wise, G. (2016). Exploring engineering: An introduction to engineering and design. Amsterdam: Elsevier/AP.

APPENDICES

Appendix A

Ion Trapping Groups

When I started on the QuantumIon project, I began by looking at ion trapping theses. This list is an important resource for any project relating to ion trapping, and it can be found at https://quantumoptics.at/images/miscellaneous/IonTrappers.pdf. This list is more or less comprehensive. Below are reported base pressures taken from theses for context. Note that these numbers do not necessarily reflect the pressure at the ion.

Advisor-Student	Reported Base Pressure (mbar)
Blatt-Rotter	10^{-11} range [23]
Chuang-Leibrandt	10^{-12} range (cryogenic) [24]
Drewsen-Hojbjerre	$4 \cdot 10^{-10}$ [29]
Gerritsma-Furst	$1 \cdot 10^{-10}$ [30]
Hilico-Heinrich	$6 \cdot 10^{-11}$ [25]
Home-Lindenfelser	$< 5 \cdot 10^{-11}$ [26]
Kim-Zhang	10^{-11} range [27]
Schmidt-Kaler-Ziesel	$3 \cdot 10^{-11}$ [31]
Lucas-Linke	$2 \cdot 10^{-11}$ [32]
Monroe-Hucul	$< 1 \cdot 10^{-11}$ [28]

Table A.1: Reported base pressures from other ion trapping groups.

Appendix B

$^{133}Ba^{+}$ Zeeman Splitting

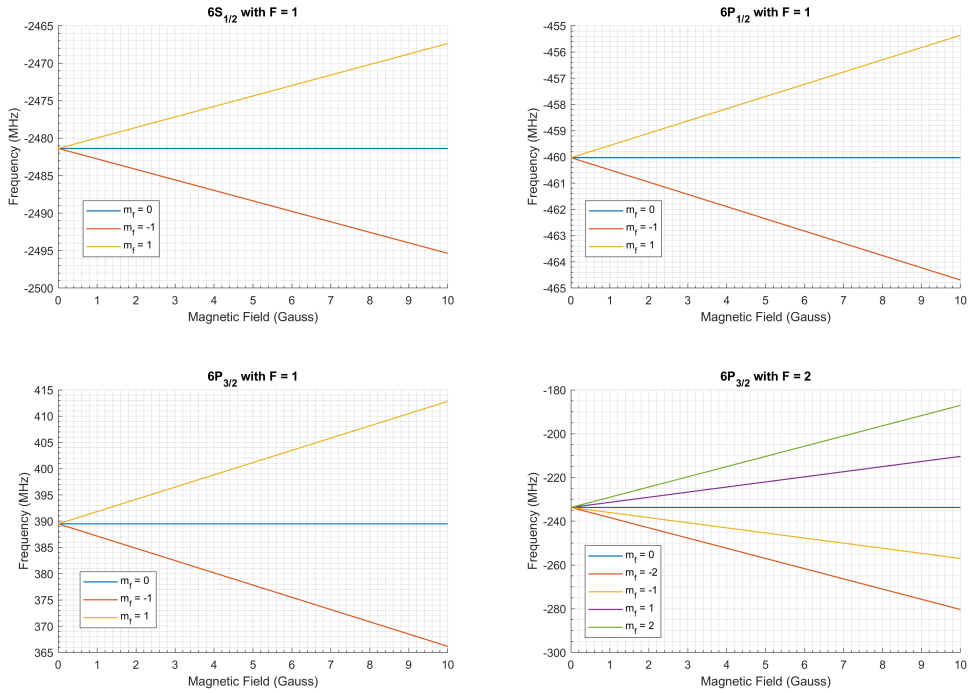

Figure B.1: $6S_{1/2}$, $6P_{1/2}$, and $6P_{3/2}$ levels with 20 MHz uncertainty in the hyperfine splitting used to calculate the Zeeman splitting [59].

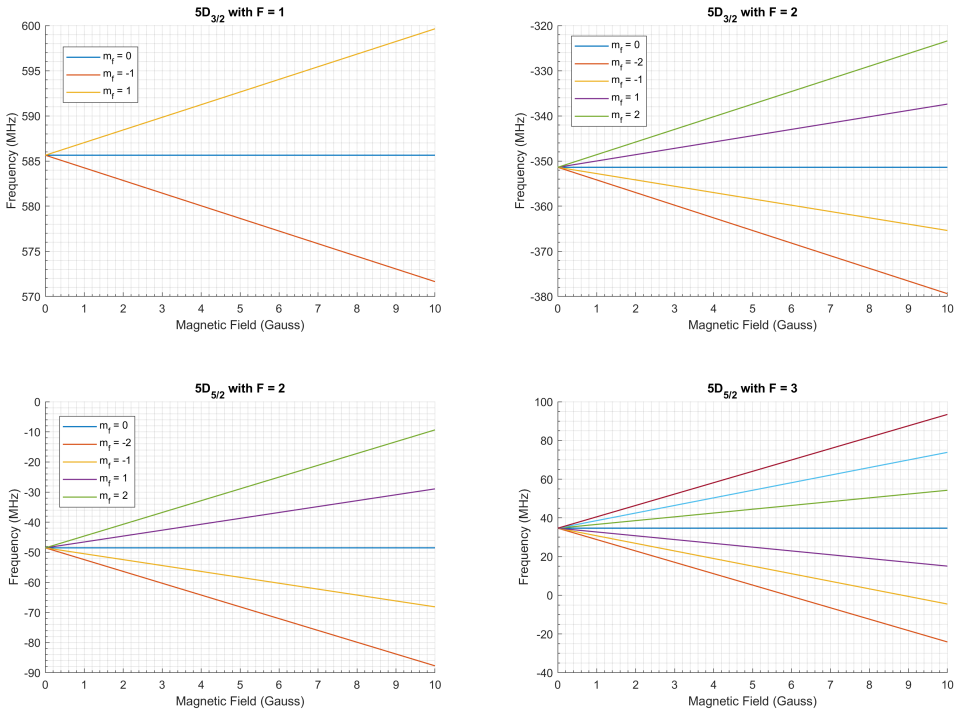

Figure B.2: $5D_{3/2}$ and $5D_{5/2}$ levels with 20 MHz uncertainty in the hyperfine splitting used to calculate the Zeeman splitting [59]. Although this is not explicitly evident, the $5D_{5/2}$ $|F = 2\rangle$ and $|F = 3\rangle$ hyperfine levels start to cross at at fields > 5 Gauss. In order to make these levels distinguishable, the magnitude of the magnetic field should be ≤ 5 Gauss.

This was calculated using the energy shifts due to the nuclear and electron spin coupling [53]. The g-factor constants were taken to be $g_L \approx 1$ and $g_s \approx 2$ and the hyperfine shifts were considered to be dominated by the magnetic-dipole and electric-quadrupole, ignoring the magnetic-octupole term.

$$\Delta E_{hf} = \frac{1}{2}A(J)K + \frac{B}{4}\frac{\frac{3}{2}K(K+1) - 2I(I+1)J(J+1)}{I(2I-1)J(2J-1)} \tag{B.1}$$

In Equation B.1, $K = F(F+1) - I(I+1) - J(J+1)$, the nuclear spin is $I = 1/2$, the total angular momentum is J, and the magnetic field B [53]. The second term in this equation is not relevant for $I = 1/2$.

$$A(J) = \frac{\Delta E(F) - \Delta E(F-1)}{F} \tag{B.2}$$

The strength of the nuclear spin and orbtial angular momentum coupling is set by the magnetic hyperfine constant $A(J)$ in Equation B.2. This is usually experimentally measured and depends on the F number of the hyperfine levels [100]. These hyperfine levels are further split in a magnetic field due to the Zeeman effect.

$$\Delta E_s = \frac{1}{2}A(J)K + \frac{B}{4}\frac{\frac{3}{2}K(K+1) - 2I(I+1)J(J+1)}{I(2I-1)J(2J-1)} + g_F\mu_B B m_F \tag{B.3}$$

Equation B.3 was used to create the plots in Figure B.1 and B.2, which is a useful reference for when working with $^{133}Ba^{+}$.

Appendix C

Additional Optical Schematics

Figure C.1 is a layout of the CW optomechanical beam paths, starting from fiber until the ion on the optics table. The single-mode PM fiber transfers light from the optical rack, where the lasers, AOMs, and EOMs are housed. This schematic is meant as a qualitative example of the steps that need to be taken to ensure that all portions of the experiment can be properly integrated. This picture is a portion of the optics table (which has a total area of about 5x10 sq. ft.).

This high resolution schematic is to relative scale and the projections are of components we intend to implement in the system, however there are many crucial portions not pictured like the Raman optics, imaging system, ablation beam path, and resonator. While some of the beam paths will remain the same, there are are important differences in the final designs not reflected in this schematic.

The orientation of the beam paths with respect to each other are fixed, based on the types of transitions that we want to drive, but the orientation of the beam paths with respect to the table are not. In this orientation, preference has been given to the Raman optics, such that they can span along the longer dimension of the optics table. The smallest portions of the optics table space was reserved for the resonator and ablation beam paths. The width of the table was determined by the size of the CW telescopes and accompanying optics. The minimum effective focal length of the telescopes were also determined by this schematic, ultimately dictated by the amount of room needed to fit control components. The chamber was chosen to be mounted in the center of the table because it provides as much of a "blank canvas" for the optical engineering and it is also consistent with the current optical designs.

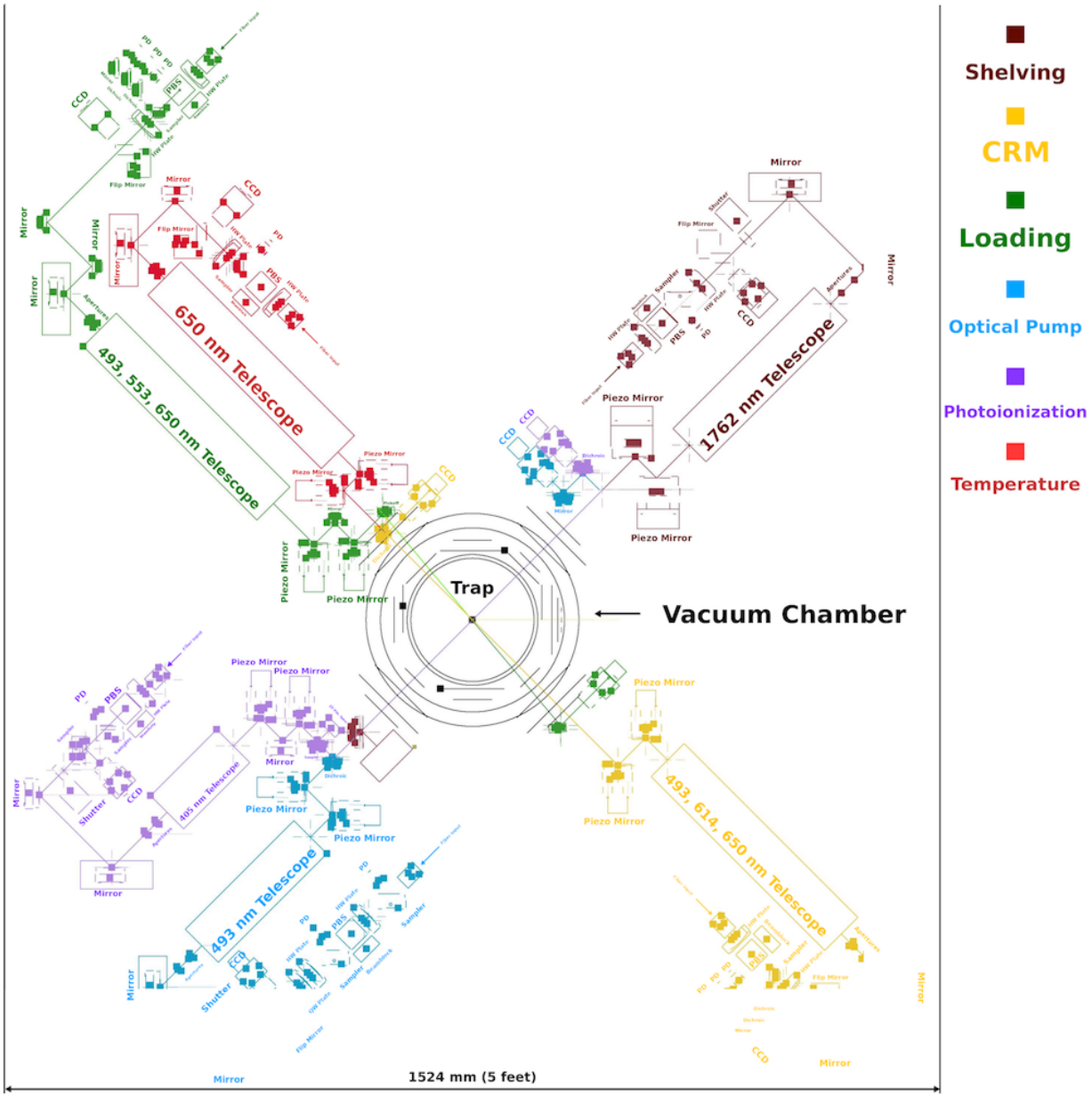

Figure C.1: Close up on projections of the CW optics on the optics table.

Below is useful information relating to the previously mentioned telescopes. The lens ID refers to lenses on the optical schematics in Chapter 4. The length refers to the total footprint on the optics table, including mounts. The beam waists are also listed, but they vary depending on the wavelengths. The transmission loss refers to the amount of loss due to reflection and it is taken from the respective AR coating curves provided by the vendors. The power level at the storage zone is just taken to be the power level at the loading zone, limited by the beam waists. The power levels are based on ideal Gaussian beams.

ID	Part	Focal Length	Description
Second Photoion. Lens 1	Thorlabs LC4252-A	-30 mm	Plano-Concave
Second Photoion. Lens 2	Thorlabs LA1145-A	80 mm	Plano-Convex
Second Photoion. Lens 3	Edmund Optics 69364	500 mm	Plano-Convex

Table C.1: Lens information for the 405 nm telescope.

Collimator	Schäfter + Kirchhoff 60FC-4-M15-01
Length	125 mm
Rayleigh Range	2.64 mm
Beam Waist	18.45 mm
Estimated Power Clipping on Trap	$\approx 7.6 \cdot 10^{-10}$

Table C.2: Useful properties of the 405 nm telescope.

ID	Part	Focal Length	Description
Loading Lens 1	Thorlabs ACY254-250-A	250 mm (X-Axis)	Achr. Cyl. Doublet
Loading Lens 2	Thorlabs ACY254-075-A	75 mm (Y-Axis)	Achr. Cyl. Doublet
Loading Lens 3	Thorlabs ACY254-050-A	50 mm (X-Axis)	Achr. Cyl. Doublet
Loading Lens 4	Thorlabs ACY254-200-A	200 mm (Y-Axis)	Achr. Cyl. Doublet
Loading Lens 5	Newport PAC091	500 mm	Achr. Doublet

Table C.3: Lens information for the 493, 553, and 650 nm loading telescope.

Collimator	Schäfter + Kirchhoff 60FC-4-RGBV11-47
Length	500 mm
Rayleigh Range	2 mm, 250 mm (Y,X)
Beam Waists	17.1-22.6 microns, 198-240 microns (Y,X)
Estimated Transmission Loss	7% (493 nm)
Estimated Power Clipping on Trap	$\approx 5.0 \cdot 10^{-10}$ (493 nm)
Estimated Power at Quantum & Storage Zone	$\approx 6.1 \cdot 10^{-8}$ (493 nm)

Table C.4: Useful properties of the 493, 553, and 650 nm loading telescope.

ID	Part	Focal Length	Description
CRM Lens 1	Thorlabs ACY254-200-A	200 mm (X-Axis)	Achr. Cyl. Doublet
CRM Lens 2	Thorlabs ACY254-050-A	50 mm (Y-Axis)	Achr. Cyl. Doublet
CRM Lens 3	Thorlabs ACY254-050-A	50 mm (X-Axis)	Achr. Cyl. Doublet
CRM Lens 4	Thorlabs ACY254-150-A	150 mm (Y-Axis)	Achr. Cyl. Doublet
CRM Lens 5	Newport PAC090	500 mm	Achr. Doublet

Table C.5: Lens information for the 493, 614, 650 nm CRM telescope.

Collimator	Schäfter + Kirchhoff 60FC-4-RGBV11-47
Length	425 mm
Rayleigh Range	2 mm, 250 mm (Y,X)
Beam Waist	15-20 microns, 174-217 microns (Y,X)
Estimated Transmission Loss	7% (493 nm)
Estimated Power Clipping on Trap	$\approx 4.0 \cdot 10^{-10}$ (493 nm)
Estimated Power at Loading & Storage Zone	$\approx 4.7 \cdot 10^{-8}$ (493 nm)

Table C.6: Useful properties of the 493, 614, and 650 nm CRM telescope.

ID	Part	Focal Length	Description
Opt. Pump. Lens 1	Thorlabs LK4349RM-A	-50 mm (Y-Axis)	Cyl. Plano-Concave
Opt. Pump. Lens 2	Thorlabs LJ4667RM-A	200 mm (X-Axis)	Cyl. Plano-Convex
Opt. Pump. Lens 3	Thorlabs LJ4643RM-A	150 mm (Y-Axis)	Cyl. Plano-Convex
Opt. Pump. Lens 4	Thorlabs LK4349RM-A	-50 mm (X-Axis)	Cyl. Plano-Concave
Opt. Pump. Lens 5	Thorlabs LA1380-A	500 mm	Plano-Convex

Table C.7: Lens information for the 493 optical pumping telescope.

Collimator	Schäfter + Kirchhoff 60FC-4-M12-33
Length	300 mm
Rayleigh Range	2.04 mm, 244 mm (Y,X)
Beam Waist	17.92 microns, 196 microns (Y,X)
Estimated Transmission Loss	5%
Estimated Power Clipping on Trap	$\approx 5.0 \cdot 10^{-10}$
Estimated Power at Loading & Storage Zone	$\approx 6.0 \cdot 10^{-8}$

Table C.8: Useful properties of the 493 nm optical pumping telescope.

ID	Part	Focal Length	Description
Shelving Lens 1	Thorlabs LK1085L1-C	-20 mm (Y-Axis)	Cyl. Plano-Concave
Shelving Lens 2	Thorlabs LK1431RM-C	-75 mm (X-Axis)	Cyl. Plano-Convex
Shelving Lens 3	Thorlabs LJ1567RM-C	100 mm (X-Axis)	Cyl. Plano-Concave
Shelving Lens 4	Thorlabs LJ1267L1-C	250 mm (Y-Axis)	Cyl. Plano-Convex
Shelving Lens 5	Thorlabs LA1380-C	500 mm	Plano-Convex

Table C.9: Lens information for the 1762 shelving telescope.

Collimator	Schäfter + Kirchhoff 60FC-4-A8S-09
Length	325 mm
Rayleigh Range	1.03 mm, 91 mm (Y,X)
Beam Waist	24.3 microns, 226 microns (Y,X)
Estimated Transmission Loss	12.6%
Estimated Power Clipping on Trap	$\approx 1.2 \cdot 10^{-9}$
Estimated Power at Loading & Storage Zone	$\approx 7.9 \cdot 10^{-8}$

Table C.10: Useful properties of the 1762 nm shelving telescope.

Appendix D

Selected Mechanical Drawings

The drawings in this appendix give the reader a reference for the more important mechanical designs in the project. All drawings are reprinted with permission.

The custom 5-way cross was manufactured by VISTA Corp. with welded "tabs" to attach the frame that is pictured on the following page. There are drawings for flanges, a custom nipple, and the frame subsections, but these were omitted to save space. The Kimball physics chambers were also omitted because they can be found on the company website.

The titanium re-entrant viewports will be manufactured by MPF Products. Thanks to Nikolay Videnov for working with MPF Products and Special Optics to tolerance the glass as well as coordinate with FiveNine Optics for coating specifications. The standard viewports were omitted.

The custom stainless steel feedthrough from MDC Vacuum Products with 100 micro sub-D connections to carry DC voltages and 16 copper pins to carry the RF voltage and provide other, separate, grounds. Stainless steel was chosen because it is easier to weld when compared to titanium.

The ZIF socket connects the trap to the flexible printed circuit. This piece was developed for Sandia National Laboratories and is compatible with multiple chip trap designs. This is a highly specialized piece, but it is possible to make the socket out of a more UHV-friendly material like MACOR.

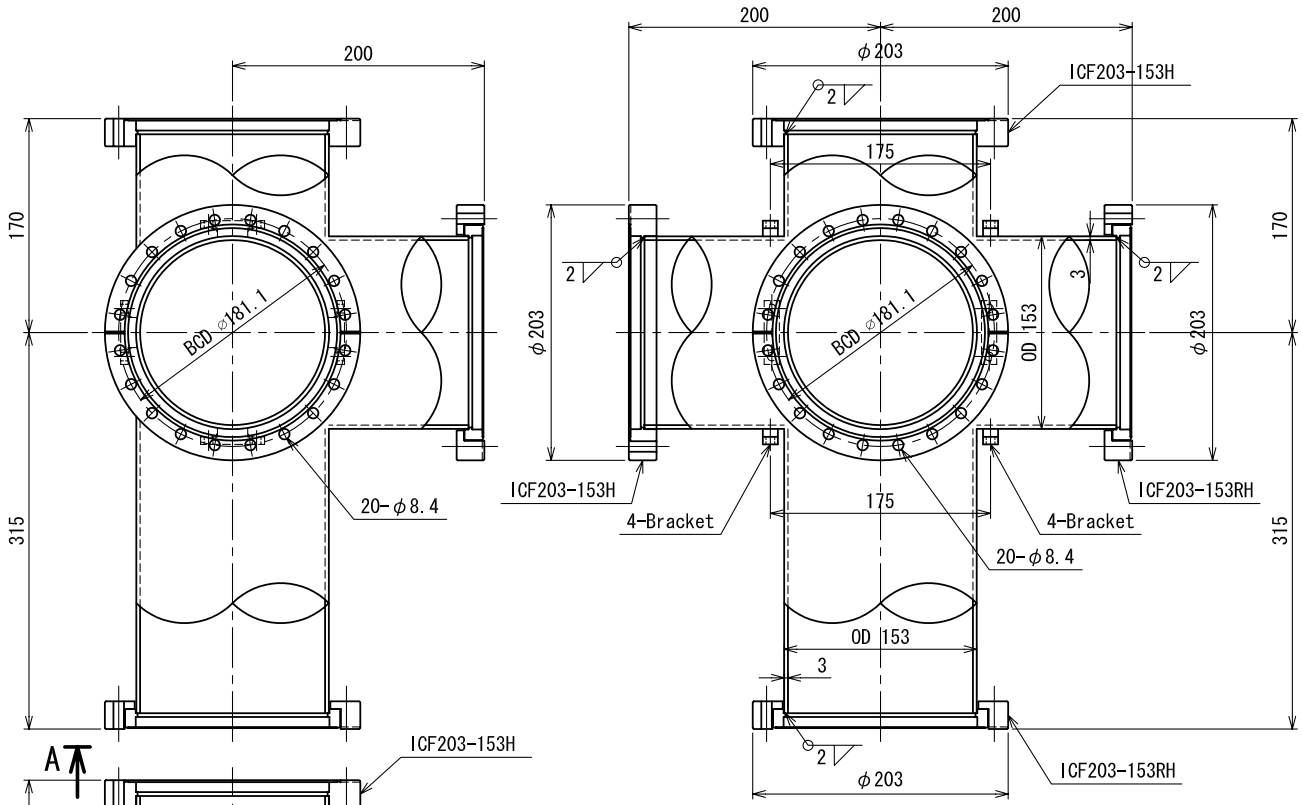

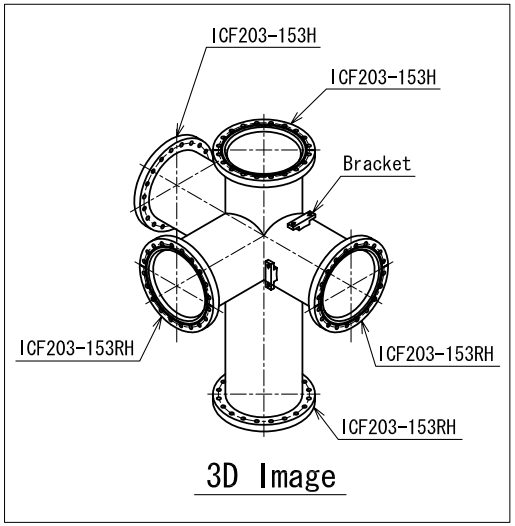

122

NOTE 1

1. Inside/outside buff #400 polished & chemical treatment.

MILL	NO.	DESCRIPTION	MATERIAL	REQ'D	SPARE	REQ'D TOTAL	REMARKS

CUSTOMER	University of Waterloo		JOB.NO.	5703P01
TITLE	Custom 5 way cross ASSEMBLY		QUANTITY	1 SET
			SCALE	1/4
			DRAWN	m.nawata
			DRAWN DATE	2020/03/24
	VISTA Corporation			
		DWG.NO.	P-020004-01	REV 0

REV	REVISION NOTE	DATE	DESIGNED	CHK'D	APP'D
0		2020/03/24	m.hesaka	t.osako	m.hesaka

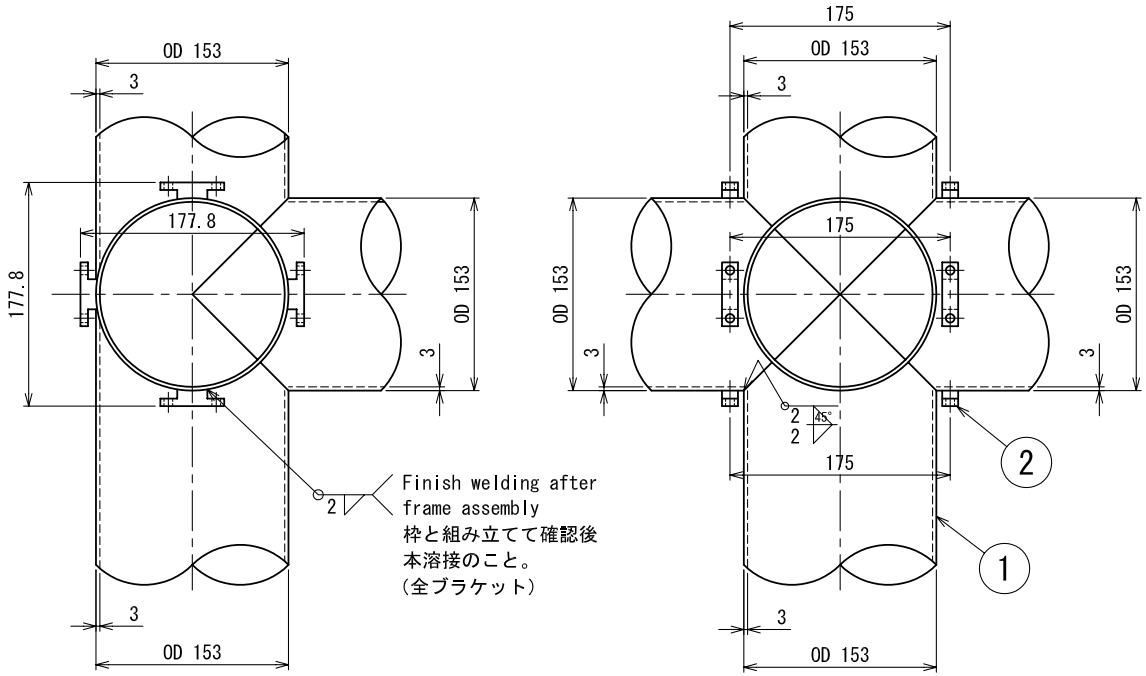

123

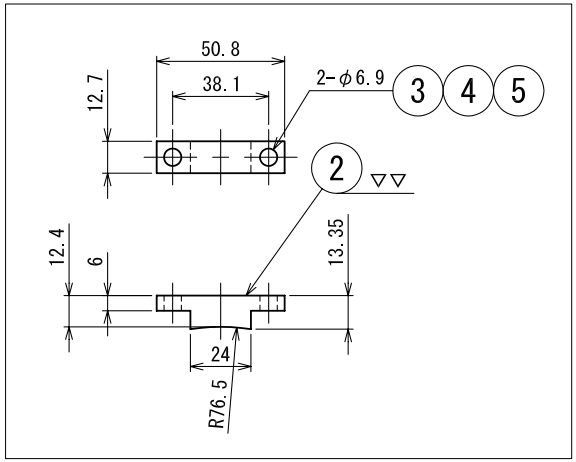

	NO.	DESCRIPTION	MATERIAL	REQ'D	SPARE	REQ'D TOTAL	REMARKS
	5	Round Washer	TB340	32		32	1/4-20UNC
	4	HEX Nut	TB340	16		16	1/4-20UNC
	3	HEX. socket cap screw	TB340	16		16	1/4-20UNC×20L
	2	Bracket	TP340	8		8	
	1	Pipe	TTP340W	1		1	OD 153×t3

REV	REVISION NOTE	DATE	DESIGNED	CHK'D	APP'D
0		2020/03/24	m.hesaka	t.osako	m.hesaka

CUSTOMER: University of Waterloo

JOB.NO.: 5703P01

TITLE: Custom 5 way cross
Body & Bracket

QUANTITY: 1 SET
SCALE: 1/4, 1/2
DRAWN: m.nawata
DRAWN DATE: 2020/03/24

VISTA Corporation

DWG.NO. P-020004-02 REV 0

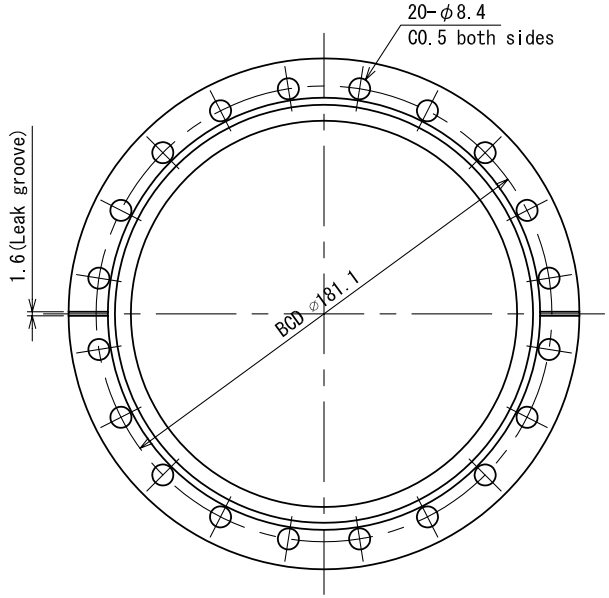

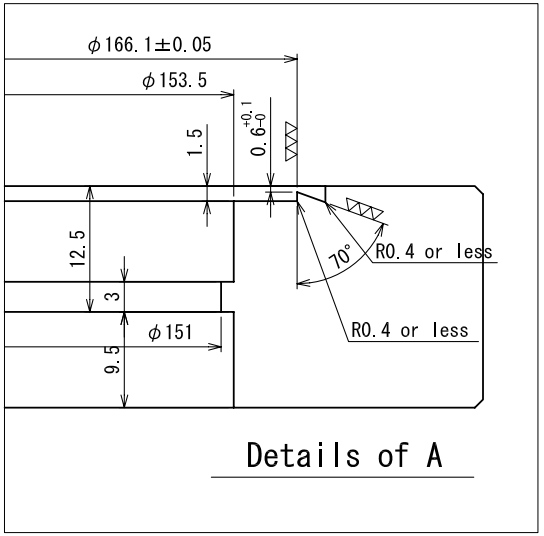

Details of A

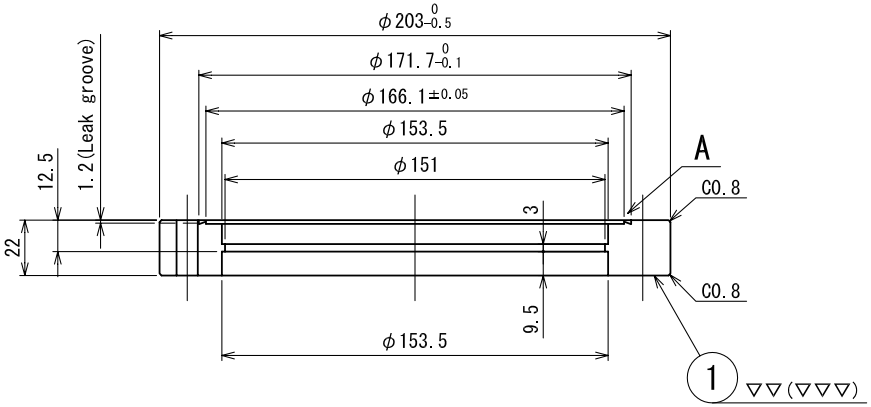

ICF203-153H

124

	1	ICF FLANGE	KS100	2		2	ICF203-153H
MILL	NO.	DESCRIPTION	MATERIAL	REQ'D	SPARE	REQ'D TOTAL	REMARKS

CUSTOMER	University of Waterloo	JOB.NO.	5703P01	
TITLE	Custom 5 way cross Detailed view of flange(1)	QUANTITY	1	SET
		SCALE	1/2, ×2	
		DRAWN	m.nawata	
		DRAWN DATE	2020/03/24	
	VISTA Corporation			
	DWG.NO. P-020004-03	REV	0	

REV	REVISION NOTE	DATE	DESIGNED	CHK'D	APP'D
0		2020/03/24	m.hesaka	t.osako	m.hesaka

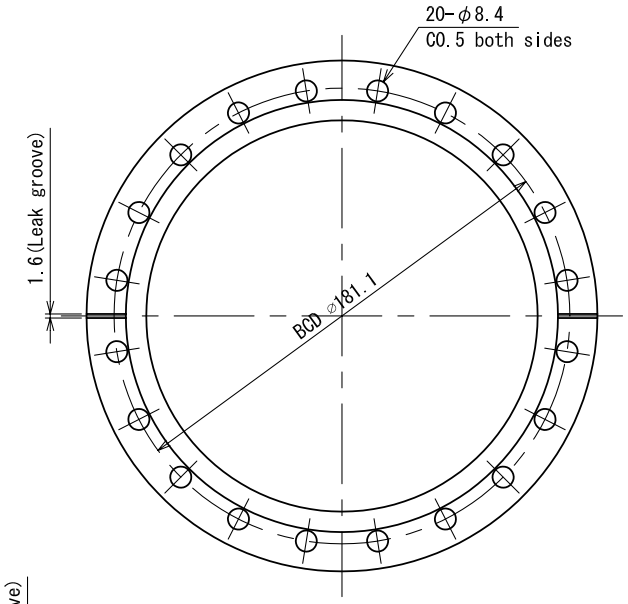

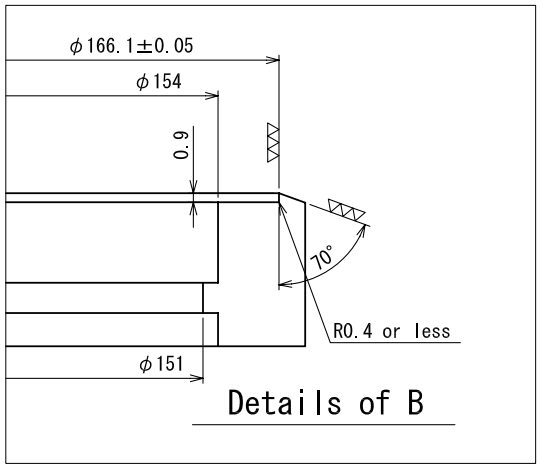

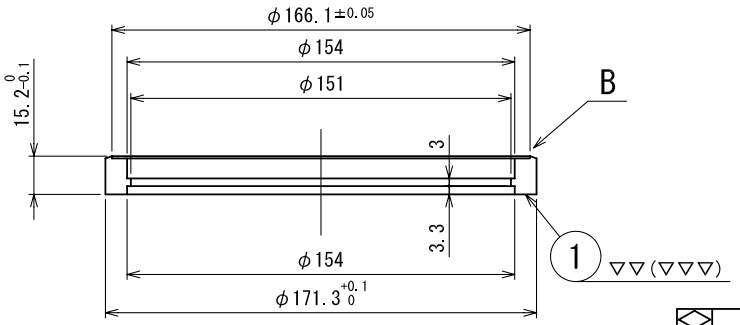

ICF203-153RH

125

MILL	NO.	DESCRIPTION	MATERIAL	REQ'D	SPARE	REQ'D TOTAL	REMARKS
	2	ICF RECEIVE FLANGE	KS100	3		3	ICF203-153RH
	1	ICF INSERT FLANGE	KS100	3		3	ICF203-153RH

REV	REVISION NOTE	DATE	DESIGNED	CHK'D	APP'D
0		2020/03/24	m.hesaka	t.osako	m.hesaka

CUSTOMER: University of Waterloo

JOB.NO.: 5703P01

TITLE: Custom 5 way cross
Detailed view of flange(2)

QUANTITY: 1 SET
SCALE: 1/2, ×2
DRAWN: m.nawata
DRAWN DATE: 2020/03/24

VISTA Corporation

DWG.NO. P-020004-04 REV 0

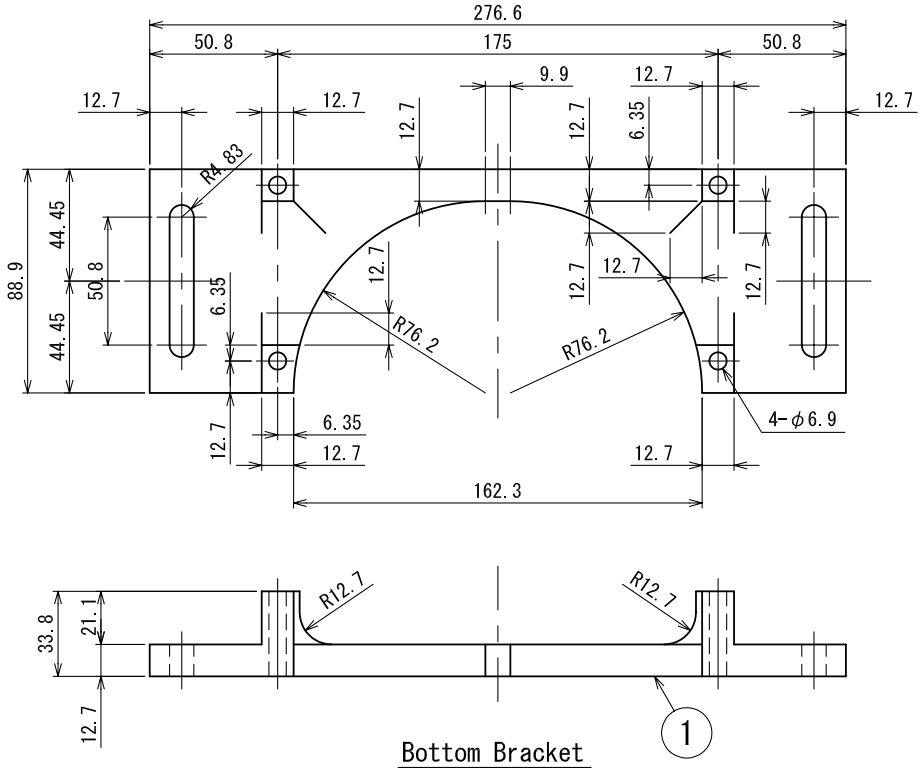

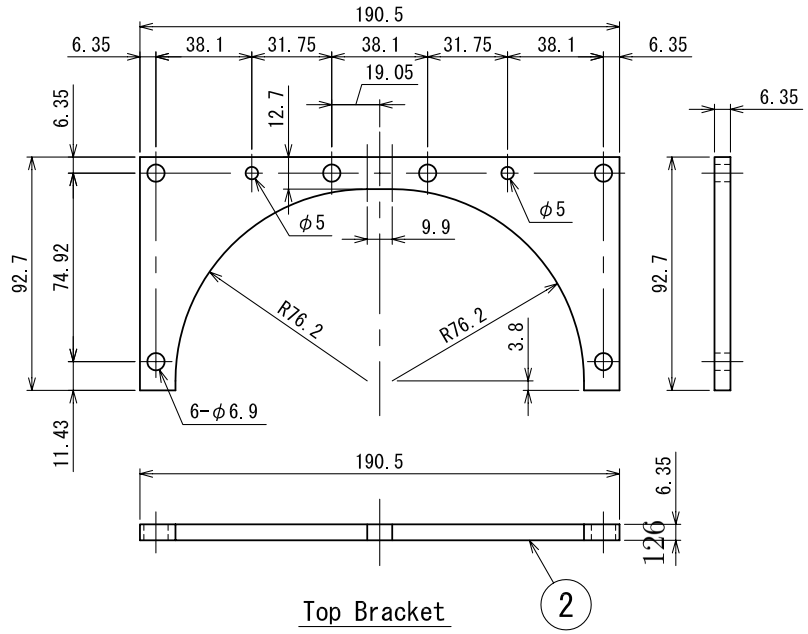

NOTE 1
1.No buffing

	NO.	DESCRIPTION	MATERIAL	REQ'D	SPARE	REQ'D TOTAL	REMARKS
	2	Top Bracket	TP340	2		2	
	1	Bottom Bracket	TP340	2		2	

0		2020/03/24	m.hesaka	t.osako	m.hesaka
REV	REVISION NOTE	DATE	DESIGNED	CHK'D	APP'D

CUSTOMER: University of Waterloo
JOB.NO.: 5703P01
TITLE: Bracket Frame Top & Bottom Bracket
QUANTITY: 1 SET
SCALE: 1/2
DRAWN: m.nawata
DRAWN DATE: 2020/03/24
VISTA Corporation
DWG.NO. P-020004-11
REV 0

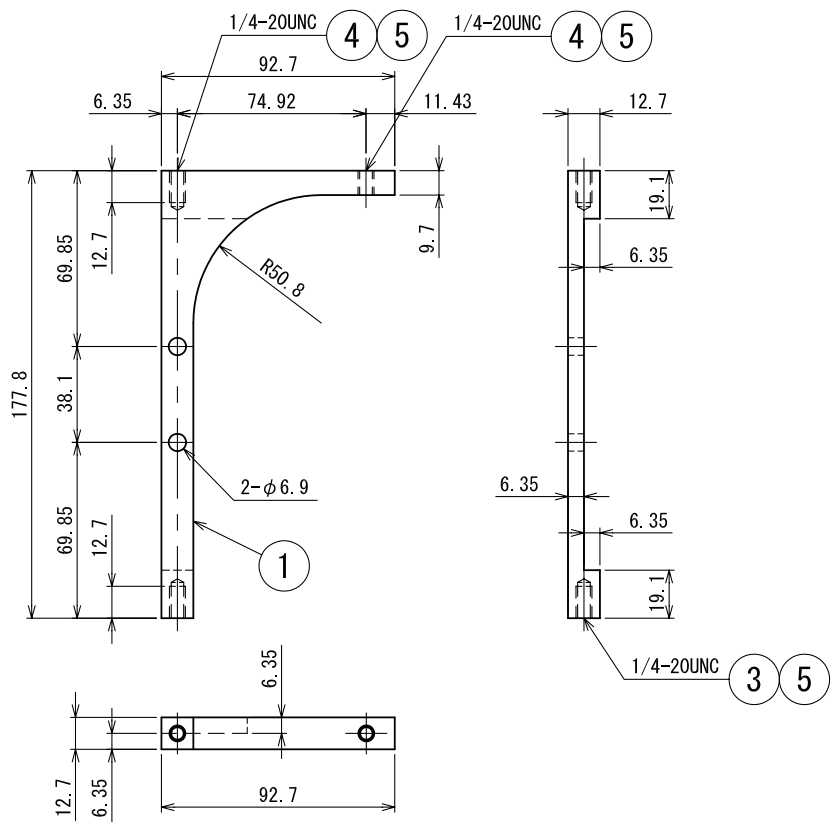

Square Frame right

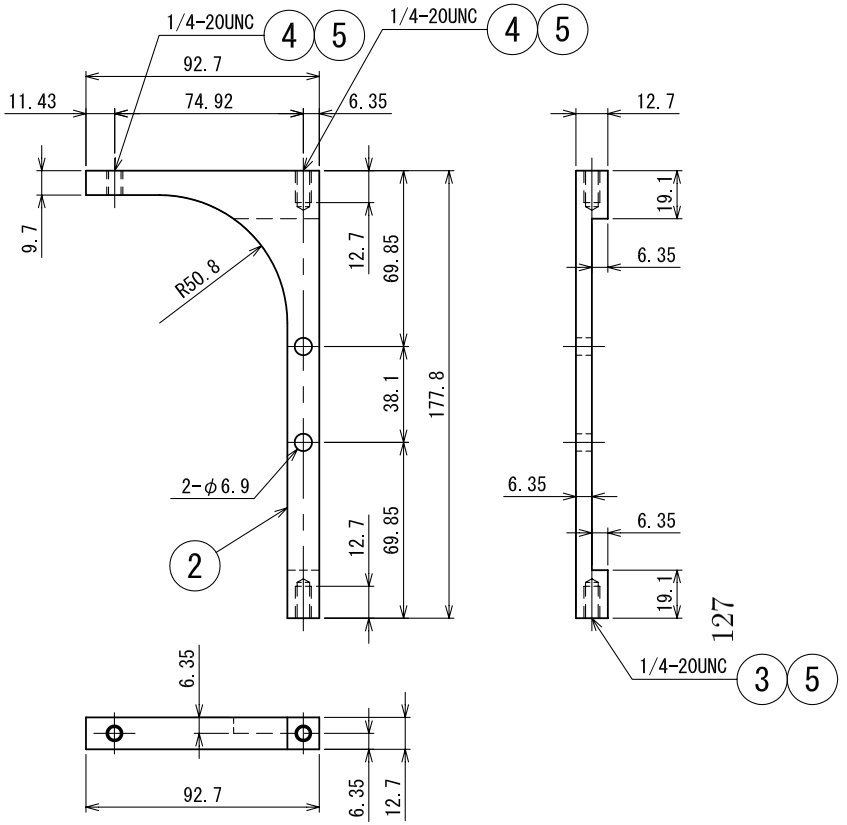

Square Frame left

NOTE 1
1.No buffing

	NO.	DESCRIPTION	MATERIAL	REQ'D	SPARE	REQ'D TOTAL	REMARKS
	5	Round Washer	TB340	12		12	1/4-20UNC
	4	HEX. socket cap screw	TB340	8		8	1/4-20UNC×45L
	3	HEX. socket cap screw	TB340	4		4	1/4-20UNC×50L
	2	Square Frame left	TP340	2		2	
	1	Square Frame right	TP340	2		2	

REV	REVISION NOTE	DATE	DESIGNED	CHK'D	APP'D
0		2020/03/24	m.hesaka	t.osako	m.hesaka

CUSTOMER: University of Waterloo
JOB.NO.: 5703P01
TITLE: Bracket Frame / Square Frame
QUANTITY: 1 SET
SCALE: 1/2
DRAWN: m.nawata
DRAWN DATE: 2020/03/24
VISTA Corporation
DWG.NO. P-020004-12 REV 0

NOTE 1
1.No buffing

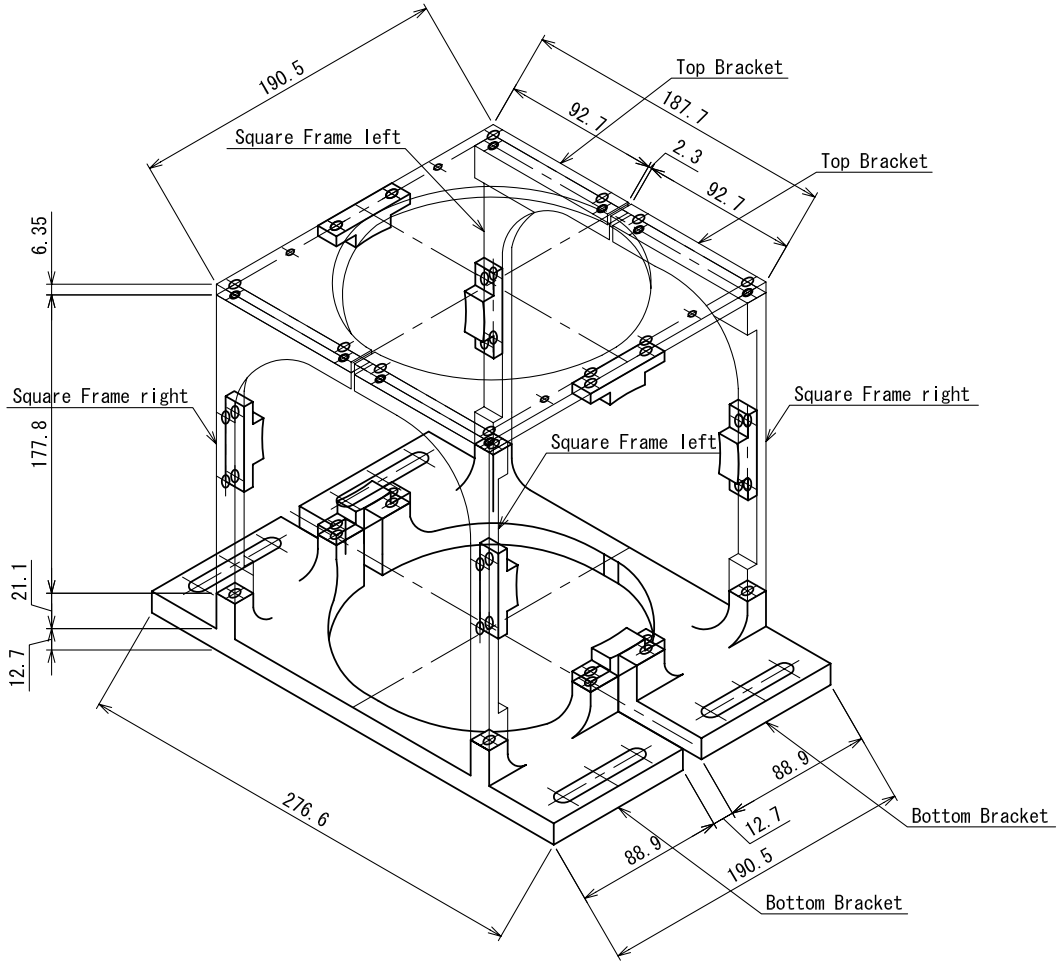

Bracket Frame 3D Image

128

MILL	NO.	DESCRIPTION	MATERIAL	REQ'D	SPARE	REQ'D TOTAL	REMARKS

0		2020/03/24	m.hesaka	t.osako	m.hesaka
REV	REVISION NOTE	DATE	DESIGNED	CHK'D	APP'D

CUSTOMER	University of Waterloo
JOB.NO.	5703P01
TITLE	Bracket Frame Assembly
QUANTITY	1 SET
SCALE	1/3
DRAWN	m.nawata
DRAWN DATE	2020/03/24
	VISTA Corporation
DWG.NO.	P-020004-13
REV	0

THIS DRAWING IS FOR QUOTATION PURPOSES ONLY

PART #: Q22695-2	REV: E	SHEET 1 OF 1

REVISION BOX			
REV.	DESCRIPTION	DATE	APPROVED
E	UPDATED WINDOW THICKNESS TOLERANCE AND CUSTOMER SUPPLIED COATING	2/28/2020	AP

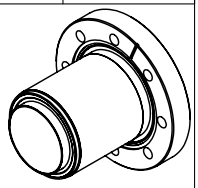

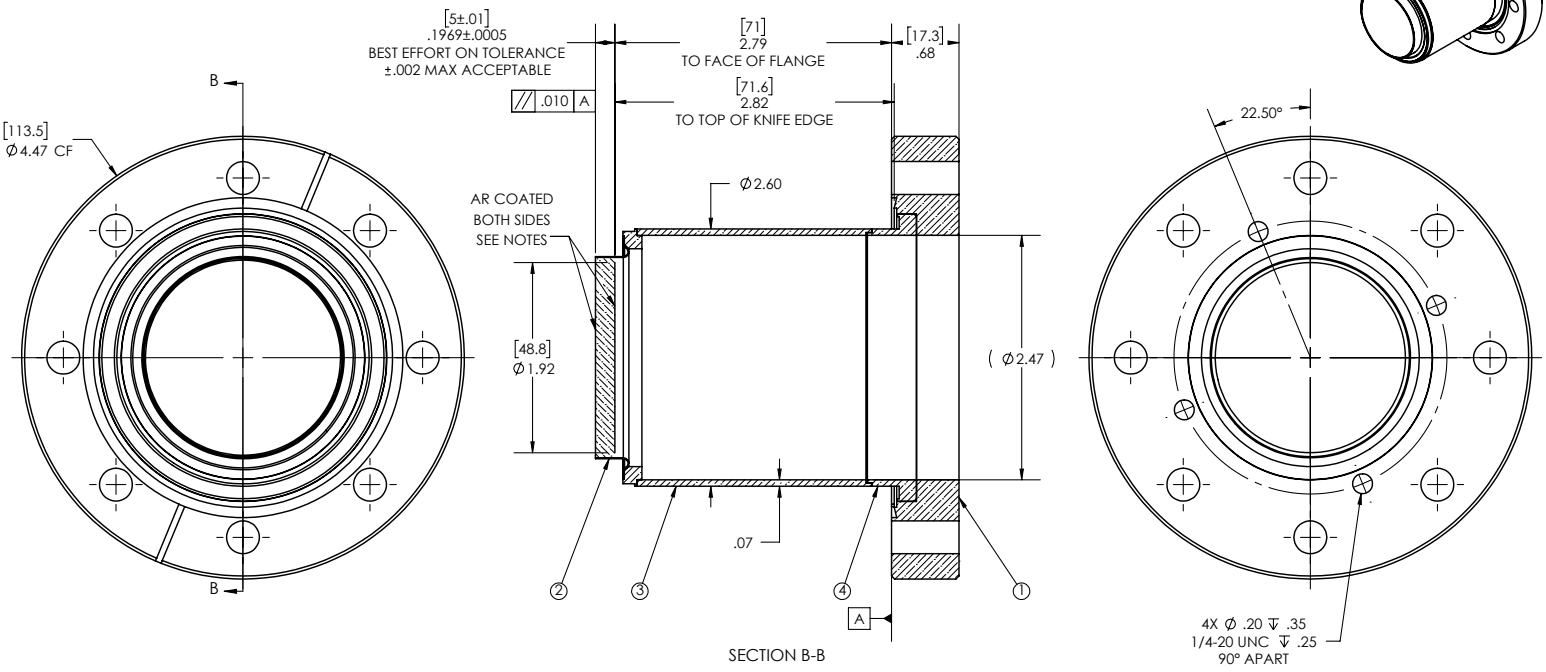

NOTES:
1. MATERIAL: HERAEUS SPECTROSIL 2000
2. HOMOGENEITY GRADE: A
3. INCLUSION CLASS: 0
4. TWD < λ/10 @ 632nm (PEAK TO VALLEY)
5. SURFACE FINISH: 20-10 SCRATCH-DIG
6. PARALLELISM: <10 ARC-SECONDS
7. CUSTOMER SUPPLIED COATING
8. LEAK RATE < $1X10^{-9}$ ATM CC/SEC HE

ITEM NO.	DESCRIPTION	QTY
1	FLANGE, TI-5 TITANIUM	1
2	COATED SUB ASSEMBLY	1
3	TUBE, TI-5 TITANIUM	1
4	ADAPTER, TI-5 TITANIUM	1

THIS DRAWING IS FOR QUOTATION PURPOSES ONLY

UNLESS OTHERWISE SPECIFIED:	QUOTATION #: Q22695-2			QUOTATION
DIMENSIONS ARE IN INCHES [ ] DIMENSIONS ARE IN MILLIMETERS FOR REFERENCE		NAME	DATE	MPF PRODUCTS INC.
TOLERANCES: ANGULAR: MACH ± 1/2° TWO PLACE DECIMAL ± .030 [.76] THREE PLACE DECIMAL ± .015 [.381]	DRAWN:	JB	8/27/2019	TITLE: LASER GRADE (DUV) FUSED SILICA MBAR COATED, 48.8mm VIEW ALL TITANIUM 4.5" CONFLAT FLANGE MOUNT
	CHECKED:		8/27/2019	
	APPROVED:	JB	8/27/2019	
REMOVE ALL BURRS AND SHARP EDGES	APPLICATION			
MIN SURFACE FINISH: Ra 63 µin | Ra 1.6 µm | N7	USED ON:		BASED ON:	
THIRD ANGLE PROJECTION:	MOUNT: Ø4.50" CF (CF 63)		WEIGHT: 1.392	DWG NO: Q22695-2 REV: E
				Friday, February 28, 2020 2:54:48 PM - BY: ENG2

THIS DRAWING IS FOR QUOTATION PURPOSES ONLY

PART #: Q22695-1	REV: C	SHEET 1 OF 1

REVISION BOX

REV.	DESCRIPTION	DATE	APPROVED
C	UPDATED WINDOW THICKNESS TOLERANCE AND CUSTOMER SUPPLIED COATING	2/28/2020	AP

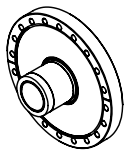

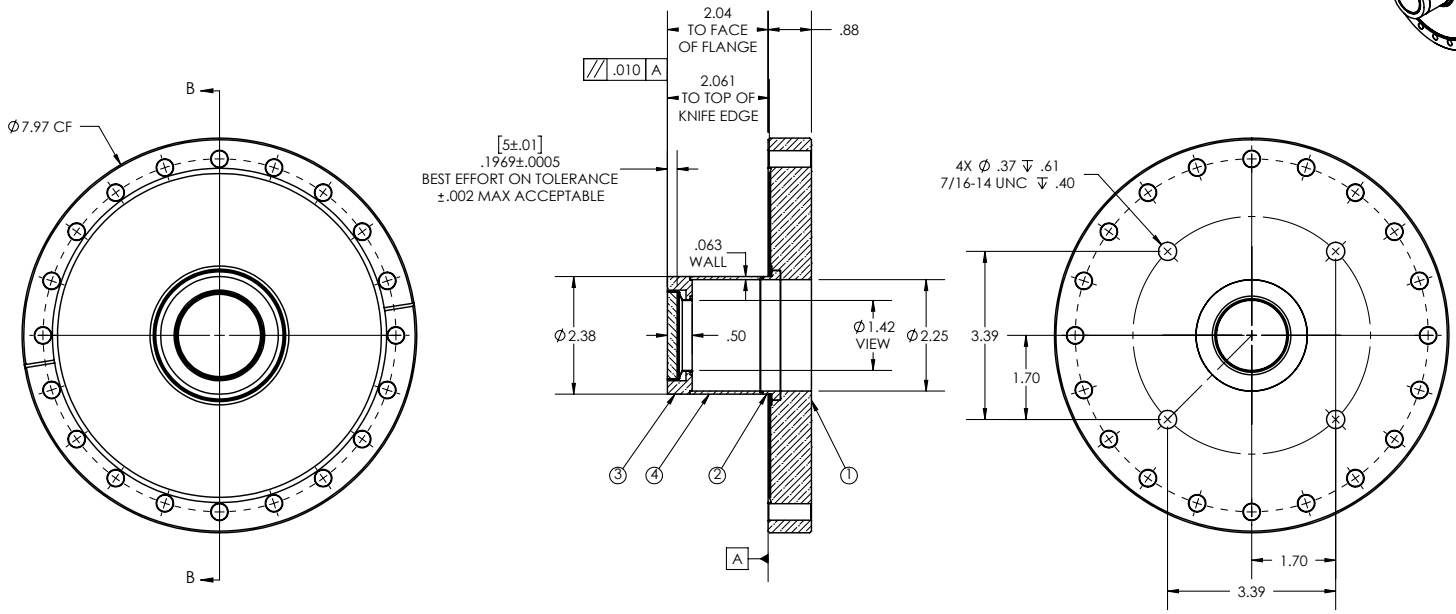

SECTION B-B

NOTES:

1. MATERIAL: HERAEUS SPECTROSIL 2000
2. HOMOGENEITY GRADE: A
3. INCLUSION CLASS: 0
4. TWD < λ/10 @ 632nm (PEAK TO VALLEY)
5. SURFACE FINISH: 20-10 SCRATCH-DIG
6. PARALLELISM: <10 ARC-SECONDS
7. CUSTOMER SUPPLIED COATING
8. LEAK RATE < 1X10⁻⁹ ATM CC/SEC HE

ITEM NO.	DESCRIPTION	QTY
1	FLANGE, TI-5 TITANIUM	1
2	ADAPTER, TI-5 TITANIUM	1
3	SUB-ASSEMBLY	1
4	TUBE, TI-5 TITANIUM	1

THIS DRAWING IS FOR QUOTATION PURPOSES ONLY

UNLESS OTHERWISE SPECIFIED:

DIMENSIONS ARE IN INCHES
[ ] DIMENSIONS ARE IN MILLIMETERS FOR REFERENCE

TOLERANCES:
ANGULAR: MACH ± 1/2°
TWO PLACE DECIMAL ± .030 [.76]
THREE PLACE DECIMAL ± .015 [.381]

REMOVE ALL BURRS AND SHARP EDGES

MIN SURFACE FINISH: Ra 63 µin | Ra 1.6 µm | N7

THIRD ANGLE PROJECTION:

QUOTATION #: Q22695-1

	NAME	DATE
DRAWN:	AC	7/10/2019
CHECKED:		7/10/2019
APPROVED:	AC	7/10/2019

APPLICATION

USED ON:	BASED ON:

MOUNT:	WEIGHT:
Ø8.00" CF (CF 150)	6.274

QUOTATION

MPF PRODUCTS INC.

TITLE:
LASER GRADE (DUV) FUSED SILICA
MBAR COATED, 1.44" VIEW
8" CONFLAT FLANGE MOUNT

DWG NO: Q22695-1 REV: C

Friday, February 28, 2020 3:22:30 PM - BY: ENG2

REVISIONS			
REV	ECN NO	DESCRIPTION	DATE
A	13771	RELEASE FOR CUSTOMER REVIEW - SQ65410	11/27/2019

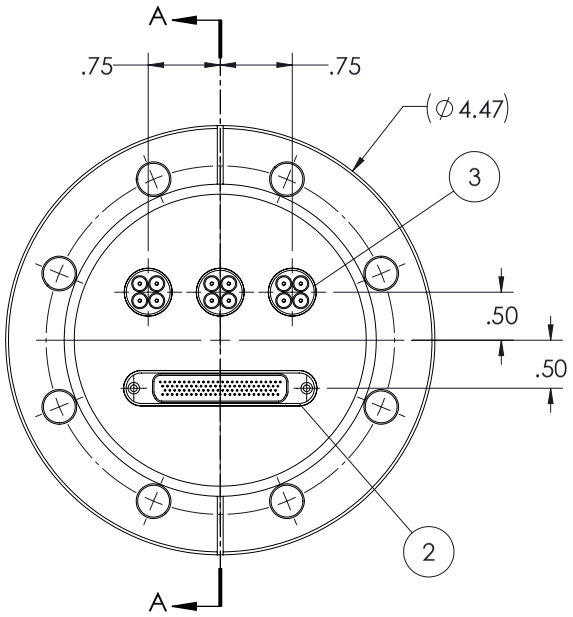

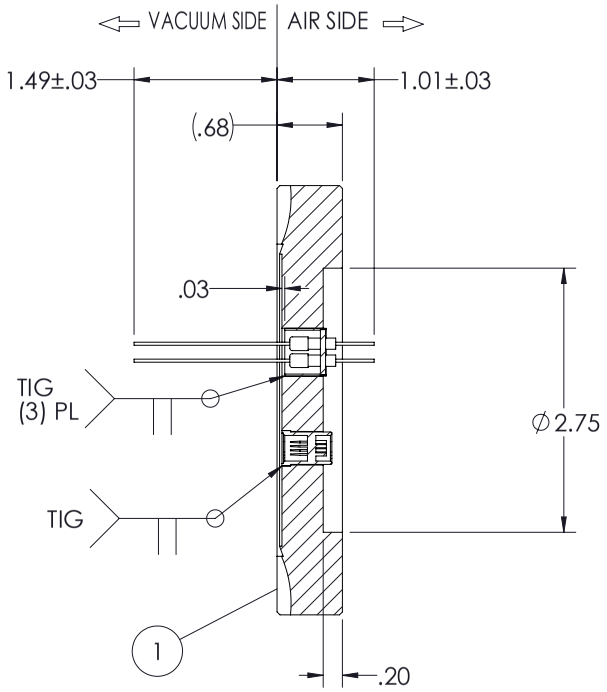

SECTION A-A

131

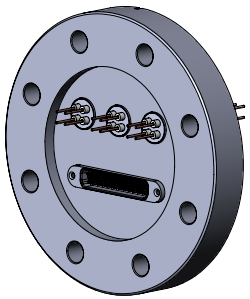

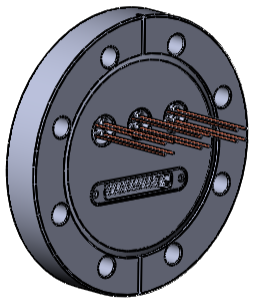

ITEM NO.	NAME	DESCRIPTION	QTY.	DWG NO
1	FLANGE	316SS	1	1418702
2	100 PIN MICRO D	STANDARD (WELDABLE)	1	1164701
3	4 PIN PWR F/T	STANDARD (9411012)	3	0028203

NOTES:

1. LEAK TEST @ 2.0×10^{-10} STD AT. cc/sec HELIUM
2. ELECTRICAL RATINGS:
   ITEM 2: 300 VDC, 5 AMPS
   ITEM 3: 500 VDC, 16 AMPS

DRAWN	DATE	CHECKED	DATE	MATERIAL	FINISH	PLATING
D.MEDIN	11-27-19	D.TAYLOR		SEE BOM	SUITABLE FOR UHV	

.XX TOL.	.XXX TOL.	ANGLES	SPECIFICATIONS
±.030	±.015	±2°	

BLOCK TOLERANCES APPLY UNLESS OTHERWISE SPECIFIED
DIMENSIONS ARE IN INCHES **DO NOT SCALE DRAWING**

INSULATOR SEAL

TITLE:
SPCL (3) PWR 0.5KV
16AMP 4PIN (1) 100PIN
MICRO-D 4.50"CF 316SS

SIZE	DWG. NO.	REV
C	1418701	A

SCALE: 2:1 SHEET 1 OF 1

4680 Series 100-4680-003A

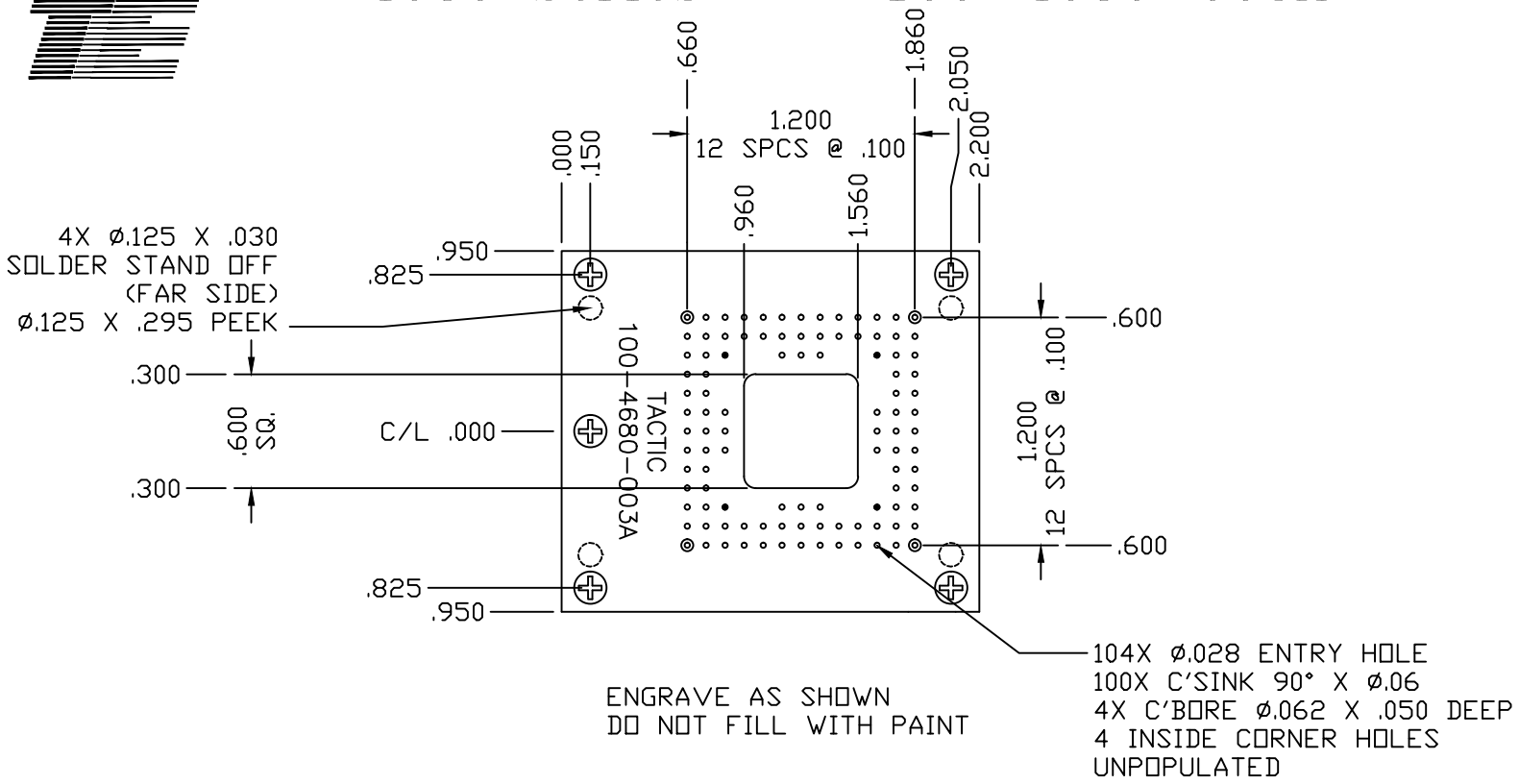

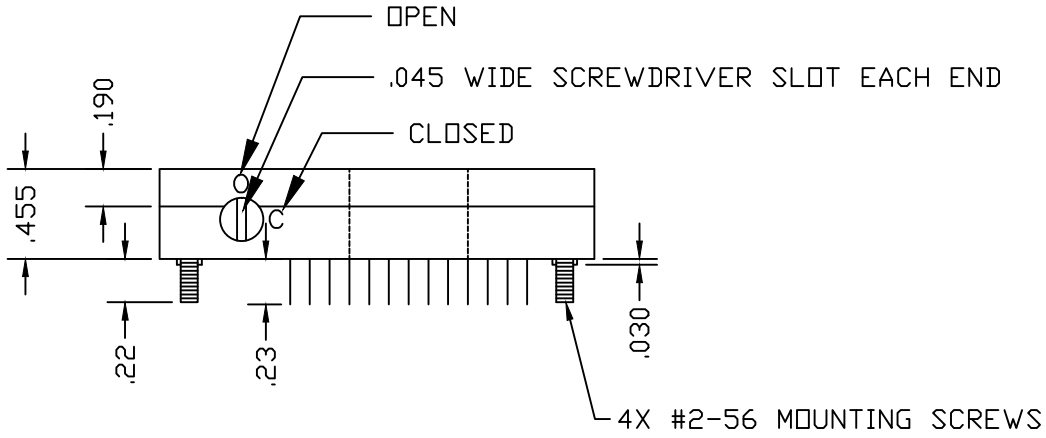

REMOVE ALL PLATING FROM THE CAM AND WEAR PLATE

Physical Insulation material: Peek (all plastic components)
Flammability: UL 94V-0
Color: Tan

Contact Tail: (010" x .018" x .23 lg)
Material: Beryllium Copper
Plating: 30μ"(.76μm)Gold-MIL-G-45204
Type II,Grade C over 50μ"(1.3μm)
Sulfamate Nickel per QQ-N-290A

Electrical Current Rating: 1 Amp
Insulation Resistance: $>1x10^9\Omega$ at 500Vdc
Withstanding Voltage: 1000 Vrms at Sea Level

Environmental Temperature Rating Operational: Be.Cu. temperature rating 302°F (150°C)
Plastics temperature rating 480°F (249°C)

Consult factory or your local TACTIC Distributor for design and pricing.
Phone: 1-800-955-4707 email: tactic1@airmail.net

Date: 4-3-2015